



**HAL**  
open science

## Collection and In Situ Analyses of Regolith Samples by the Mars 2020 Rover: Implications for Their Formation and Alteration History

E M Hausrath, R. Sullivan, Y. Goreva, M P Zorzano, A. Vaughan, A. Cousin, S. Siljeström, S K Sharma, A O Shumway, T. Kizovski, et al.

### ► To cite this version:

E M Hausrath, R. Sullivan, Y. Goreva, M P Zorzano, A. Vaughan, et al.. Collection and In Situ Analyses of Regolith Samples by the Mars 2020 Rover: Implications for Their Formation and Alteration History. *Journal of Geophysical Research. Planets*, 2025, 130 (2), 10.1029/2023JE008046 . hal-04933674

**HAL Id: hal-04933674**

<https://hal.sorbonne-universite.fr/hal-04933674v1>

Submitted on 6 Feb 2025

**HAL** is a multi-disciplinary open access archive for the deposit and dissemination of scientific research documents, whether they are published or not. The documents may come from teaching and research institutions in France or abroad, or from public or private research centers.

L'archive ouverte pluridisciplinaire **HAL**, est destinée au dépôt et à la diffusion de documents scientifiques de niveau recherche, publiés ou non, émanant des établissements d'enseignement et de recherche français ou étrangers, des laboratoires publics ou privés.



Distributed under a Creative Commons Attribution - NonCommercial - NoDerivatives 4.0 International License

## Collection and In Situ Analyses of Regolith Samples by the Mars 2020 Rover: Implications for Their Formation and Alteration History



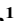








### Special Collection:

The Perseverance Rover's  
Exploration of the Western Fan  
Front, Jezero Crater, Mars

### Key Points:

- Regolith samples contain aqueous alteration potentially resulting from past habitable environments that could contain biosignatures
- Fluorescence detections are consistent with variable concentration of inorganic emitters, though small aromatic organics are also possible
- Both samples include grain sizes from microns (dust) to a few mm, and soil crust due to atmospheric interactions likely involving water

E. M. Hausrath<sup>1</sup> , R. Sullivan<sup>2</sup> , Y. Goreva<sup>3</sup> , M. P. Zorzano<sup>4</sup> , A. Vaughan<sup>5</sup> , A. Cousin<sup>6</sup> , S. Siljeström<sup>7</sup>, S. Sharma<sup>3</sup>, A. O. Shumway<sup>8</sup> , T. Kizovski<sup>9</sup>, S. J. VanBommel<sup>10</sup>, M. Tice<sup>11</sup>, A. Knight<sup>10</sup> , G. Martinez<sup>4,12</sup> , A. Vicente-Retortillo<sup>4</sup> , L. Mandon<sup>13</sup>, C. T. Adcock<sup>1</sup> , J. M. Madariaga<sup>14</sup> , I. Población<sup>14</sup>, J. R. Johnson<sup>15</sup> , J. Lasue<sup>6</sup> , O. Gasnault<sup>6</sup> , N. Randazzo<sup>16</sup>, E. L. Cardarelli<sup>3,17</sup> , R. Kronyak<sup>3</sup>, A. Bechtold<sup>18</sup> , G. Paar<sup>19</sup> , A. Udry<sup>1</sup> , O. Forni<sup>6</sup>, C. C. Bedford<sup>20</sup> , N. A. Carman<sup>1</sup> , J. F. Bell III<sup>21</sup>, K. Benison<sup>22</sup> , T. Bosak<sup>23</sup> , A. Brown<sup>24</sup> , A. Broz<sup>19</sup> , F. Calef<sup>3</sup> , B. C. Clark<sup>25</sup> , E. Cloutis<sup>26</sup> , A. D. Czaja<sup>27</sup> , T. Fornaro<sup>28</sup> , T. Fouchet<sup>29</sup> , M. Golombek<sup>3</sup>, F. Gómez<sup>4</sup> , C. D. K. Herd<sup>16</sup> , K. Herkenhoff<sup>30</sup> , R. S. Jakubek<sup>31</sup>, L. Jandura<sup>3</sup>, J. Martinez-Frias<sup>32</sup> , L. E. Mayhew<sup>33</sup> , P.-Y. Meslin<sup>6</sup>, C. E. Newman<sup>34</sup> , J. I. Núñez<sup>15</sup> , F. Poulet<sup>35</sup>, C. Royer<sup>20</sup>, P. Russell<sup>17</sup> , M. A. Sephton<sup>36</sup> , S. K. Sharma<sup>37</sup> , D. Shuster<sup>38</sup>, J. I. Simon<sup>39</sup> , I. Tirona<sup>3</sup> , R. C. Wiens<sup>20</sup> , B. P. Weiss<sup>23</sup> , A. J. Williams<sup>40</sup> , K. Williford<sup>41</sup>, Z. U. Wolf<sup>42,43</sup>, and the Regolith Working Group<sup>43</sup>

<sup>1</sup>Department of Geoscience, University of Nevada, Las Vegas, NV, USA, <sup>2</sup>CCAPS, Cornell University, Ithaca, NY, USA, <sup>3</sup>Jet Propulsion Laboratory, California Institute of Technology, Pasadena, CA, USA, <sup>4</sup>Centro de Astrobiología (CAB), CSIC-INTA, Torrejón de Ardoz, Spain, <sup>5</sup>Apogee Engineering, LLC, Flagstaff, AZ, USA, <sup>6</sup>Institut de Recherche en Astrophysique et Planétologie, Université de Toulouse 3 Paul Sabatier, CNRS, CNES, Toulouse, France, <sup>7</sup>RISE Research Institutes of Sweden, Stockholm, Sweden, <sup>8</sup>Department of Earth and Space Sciences, University of Washington, Seattle, WA, USA, <sup>9</sup>Department of Earth Science, Brock University, St. Catharines, ON, Canada, <sup>10</sup>Department of Earth and Planetary Sciences, Washington University in St. Louis, St. Louis, MO, USA, <sup>11</sup>Texas A&M University, College Station, TX, USA, <sup>12</sup>Lunar and Planetary Institute, Houston, TX, USA, <sup>13</sup>Division of Geological and Planetary Sciences, California Institute of Technology, Pasadena, CA, USA, <sup>14</sup>Department of Analytical Chemistry, University of the Basque Country UPV/EHU, Leioa, Spain, <sup>15</sup>Johns Hopkins University Applied Physics Laboratory, Laurel, MD, USA, <sup>16</sup>Department of Earth and Atmospheric Sciences, University of Alberta, Edmonton, AB, Canada, <sup>17</sup>University of California, Los Angeles, Los Angeles, CA, USA, <sup>18</sup>Department of Lithospheric Research, University of Vienna, Wien, Austria, <sup>19</sup>Joanneum Research, Graz, Austria, <sup>20</sup>Earth, Atmospheric, and Planetary Sciences, Purdue University, West Lafayette, IN, USA, <sup>21</sup>Arizona State University, Tempe, AZ, USA, <sup>22</sup>Department of Geology and Geography, West Virginia University, Morgantown, WV, USA, <sup>23</sup>Department of Earth, Atmospheric, and Planetary Science, Massachusetts Institute of Technology, Cambridge, MA, USA, <sup>24</sup>Plancius Research, Severna Park, MD, USA, <sup>25</sup>Space Science Institute, Boulder, CO, USA, <sup>26</sup>University of Winnipeg, Winnipeg, MB, Canada, <sup>27</sup>Department of Geosciences, University of Cincinnati, Cincinnati, OH, USA, <sup>28</sup>INAF—Astrophysical Observatory of Arcetri, Firenze, Italy, <sup>29</sup>LESIA, Observatoire de Paris, Université PSL, Sorbonne Université, Université Paris Cité, CNRS, Meudon, France, <sup>30</sup>US Geological Survey Astrogeology Science Center, Flagstaff, AZ, USA, <sup>31</sup>Jacobs, NASA Johnson Space Center, Houston, TX, USA, <sup>32</sup>Institute of Geosciences, IGEO (CSIC-UCM), Madrid, Spain, <sup>33</sup>Department of Geological Sciences, University of Colorado Boulder, Boulder, CO, USA, <sup>34</sup>Aeolis Research, Chandler, AZ, USA, <sup>35</sup>IAS, CNRS/Université Paris Saclay, Orsay Cedex, France, <sup>36</sup>Department of Earth Science & Engineering, Imperial College, London, UK, <sup>37</sup>University of Hawaii, Honolulu, HI, USA, <sup>38</sup>University of California, Berkeley, Berkeley, CA, USA, <sup>39</sup>NASA Johnson Space Center, Houston, TX, USA, <sup>40</sup>Department of Geological Sciences, University of Florida, Gainesville, FL, USA, <sup>41</sup>Blue Marble Space Institute of Science, Seattle, WA, USA, <sup>42</sup>Los Alamos National Laboratory, Los Alamos, NM, USA, <sup>43</sup>For Members See Appendix A

### Supporting Information:

Supporting Information may be found in the online version of this article.

### Correspondence to:

E. M. Hausrath,  
Elisabeth.Hausrath@unlv.edu

### Citation:

Hausrath, E. M., Sullivan, R., Goreva, Y., Zorzano, M. P., Vaughan, A., Cousin, A., et al. (2025). Collection and in situ analyses of regolith samples by the Mars 2020 rover: Implications for their formation and alteration history. *Journal of Geophysical Research: Planets*, 130, e2023JE008046. <https://doi.org/10.1029/2023JE008046>

Received 3 NOV 2023

Accepted 11 JUL 2024

© 2025 The Author(s). This article has been contributed to by U.S. Government employees and their work is in the public domain in the USA.

This is an open access article under the terms of the [Creative Commons Attribution-NonCommercial-NoDerivs License](https://creativecommons.org/licenses/by/4.0/), which permits use and distribution in any medium, provided the original work is properly cited, the use is non-commercial and no modifications or adaptations are made.

**Abstract** The *Perseverance* rover has sampled mm-size lithic fragments containing olivine likely from at least two source regions from the surface of an inactive megaripple surface, and fine-grained material from the surface and to a depth of ~4–6 cm. Some of the mm-size grains lack a coherent diffraction pattern measured by PIXL, consistent with the presence of poorly ordered secondary phases that have been altered. Analysis of these materials on Earth will allow examination of materials that have experienced aqueous, potentially habitable environments that could contain biosignatures. Fluorescence of three different patterns was detected, consistent with inorganic emissions from silica defects or rare earth elements in certain mineral phases, although organic origin cannot be excluded. Analysis of Autofocus Context Imager and Wide Angle Topographic Sensor for Operations and eNginering images of the subsurface material and MEDA thermal inertia measurements indicate average grain sizes of ~125 and ~150 μm, respectively, for the bulk material within the megaripple.

The fine-grained material in the sampling location indicates chemical compositions similar to previously proposed global components as well as airfall dust. In situ and associated atmospheric measurements provide evidence of recent processes likely including water vapor in soil crust formation. The sampled material will therefore help elucidate the formation of Martian soils; current surface-atmosphere interactions; the composition, shape, and size distribution of dust grains valuable for studies of past and present Martian climate and for assessing potential health and other risks to human missions; and ancient, aqueously altered environments that could have been habitable, and, if Mars contained life, possibly contain biosignatures.

**Plain Language Summary** The first samples of soil/regolith/loose sediment have recently been collected from Jezero crater Mars. The *Perseverance* rover is able to sample loose material less than 8 mm in size from the surface to a depth of ~4–6 cm, which is then sealed in a sample tube and either deposited on the surface of Mars or stored in the rover similarly to the rock samples for potential return to Earth by the planned Mars Sample Return campaign. Soil samples include mm-size grains that are aqueously altered, are likely from at least two different source regions, and indicate potentially habitable environments that, if Mars contained life, could potentially contain biosignatures. Fluorescence of three different patterns was detected, which could be due to inorganic emissions from silica defects or rare earth elements in certain mineral phases, though organic origin cannot be excluded. The 125–150  $\mu\text{m}$  fine grains appear similar to a previously proposed global soil component, and the collection of airfall dust and soil crust components includes material that has been affected by interactions with the atmosphere, and sheds light on topics ranging from climate to the safety of future human missions.

## 1. Introduction

Much of the surface of Mars observed from orbiters, landers, and rovers is covered by a discontinuous surface layer of mostly unconsolidated material up to several meters thick (e.g., Christensen & Moore, 1992; Golombek et al., 2008). The material of this surface layer integrates products of physical and chemical weathering over the course of Martian history, and reflects aeolian, fluvial, and impact processes that have emplaced these products. The porous, uppermost part of this material is also affected by ongoing chemical exchanges and interactions with the atmosphere.

Throughout this manuscript, the term “regolith” is used similarly to the E2E-iSAG report Planning for Mars Returned Sample Science: Final report of the Mars Sample Return (MSR) End-to-End International Science Analysis Group (McLennan et al., 2012): “the entire layer of fragmental and loose, incoherent, or unconsolidated rock material of any origin, that mantles more coherent bedrock (Gary et al., 1972). It includes: soil, defined as any loose, unconsolidated material that can be distinguished from rocks, bedrock, or strongly cohesive sediments but has no singular origin; airfall dust, which is fine-grained material that has settled from the atmosphere; and aeolian deposits, which represent any accumulation of windblown sediment that occurs in recognizable bedforms or as sand sheets” (McLennan et al., 2012).

Regolith is also sometimes interpreted as implying that the material has not been transported (i.e., G. Taylor & Eggleton, 2001). Consistent with the E2E-iSAG report (McLennan et al., 2012), this interpretation is not used in this work. However, larger grains present in the sampled material that are likely to have been locally derived are discussed throughout this work. In addition, since the sample goals for a regolith sample previously documented within the E2E-iSAG and iMOST reports have discussed the sample goals for the constituent components, including locally derived material, aeolian sediment, and airfall dust, these components are separately described throughout the manuscript (Beatty et al., 2019; McLennan et al., 2012).

The Mars 2020 regolith samples, together with collected rock samples (Bosak et al., 2024; Farley and Stack, 2023a, 2023b, 2023c; Simon et al., 2023), will address goals previously established for MSR objectives (Beatty et al., 2019; McLennan et al., 2012; Mustard et al., 2013; NRC, 2011). The recent International MSR Objectives and Samples Team (iMOST) report identifies seven objectives for MSR (Beatty et al., 2019), which include a number of objectives relevant to collection of regolith samples, such as Objective 1: Interpret the primary geologic processes and history that formed the Martian geologic record, with an emphasis on the role of water, Objective 2: Assess and Interpret the Potential Biological History of Mars, Including Assaying Returned

Samples for the Evidence of Life, Objective 6: Understand and quantify the potential Martian environmental hazards to human exploration and the terrestrial biosphere and Objective 7: Evaluate the type and distribution of in situ resources to support future Mars exploration. The collected regolith samples have been compared to the iMOST goals and desired samples in Table S7 in Supporting Information S1 as well as evaluated for their ability to reach these goals (Czaja et al., 2023).

In order to best achieve the goals previously identified for MSR, a megaripple (different from a dune) about 48 m long, 8 m wide, and 1 m high was selected for the regolith sampling site (Figure 1). Unlike dunes, megaripples have poor particle sorting (Lämmel et al., 2018; Sharp, 1963), thus allowing collection of both coarser, likely locally derived material, along with a continuous range of finer particles having increased potential for more distant origins, ideally also including Jezero watershed materials not yet included in the Mars 2020 rock core sample collection. Besides several morphological indicators of inactivity, the megaripple also displayed evidence of a soil crust, suggesting that stability (or non-activity) of the megaripple should have allowed airfall dust to accumulate within near-subsurface pore space, and also indicating that the soil crust itself would be able to be collected.

Previous work from several landing sites has indicated that much of the finer component of Martian regolith potentially represents a ubiquitous compositional average (e.g., Clark et al., 1982; S. R. Taylor & McLennan, 2009; Yen et al., 2005). Previous summaries (e.g., S. R. Taylor & McLennan, 2009) have described Martian regolith as including potentially global components with differing contributions from volatiles and locally derived materials (e.g., Figure 2). Details of the variations among landing sites in Figure 2 are given in Supporting Information S1. Explanations for apparent global silt- and sand-sized components are uncertain (Clark et al., 1982; S. R. Taylor & McLennan, 2009; Yen et al., 2005); one possibility is that Martian crust fundamentally varies relatively little in its (mafic) composition so that weathering products of these materials result in regolith having relatively minor compositional variations from place to place around the planet. Another possibility is that whatever compositional variation that might exist in source rocks, active aeolian mixing of dust, silt- and very fine sand-sized grains over the long arid history of the planet has resulted in widespread, near-global particle mixing, even if individual regolith particles might express compositional variation from each other. Analyses of a returned regolith sample will help better understand the formation of the potentially global, local, and volatile components.

## 2. Methods

### 2.1. Selection of Sampling Location

Only a single Martian regolith sample is currently intended to be returned to Earth. Ideally, this small sample volume would represent the diverse regolith unit that covers much of the Martian surface. Regolith includes a wide range of particle sizes (dust, silt, sand, and larger components) of different compositions, and has been affected by surface-atmosphere interactions such as wind transport, crust formation, and volatile exchange within near-subsurface porosity (e.g., Arvidson et al., 2010; Blake et al., 2013; Hausrath et al., 2023; Johnson et al., 2007; Mellon et al., 2008; Ming et al., 2006; Minitti et al., 2013; O'Connell-Cooper et al., 2017; Sullivan & Kok, 2017; Vaughan et al., 2023; Wang et al., 2006, 2008). It was also hoped that the regolith sample might include Jezero watershed materials not yet included in the Mars 2020 rock core sample collection. Careful selection of the regolith sampling location was conducted to achieve as many of these science goals as possible.

Technical and operational factors applied constraints on where regolith sampling could occur. Regolith sampling capability was certified for use late in the Prime Mission (one Martian year duration), just before the Prime Mission cache was to be deposited at the Three Forks depot location (Czaja et al., 2023), which restricted available sample locations. Regolith collection involved several technical risks that could be reduced by choosing an appropriate collection site. The regolith collection system (Section 2.2) uses a hollow drill bit designed to penetrate ~6.5 cm beneath the regolith surface and sweep back and forth through the regolith to collect material through two 8 mm × 8 mm openings (Moeller et al., 2021; Section 2.2). Accordingly, terrain-related fault risks included: (a) the bit striking unseen buried rock or rubble during initial downward penetration into the regolith, or while the spinning bit swept back-and-forth through the regolith sampling volume; and (b) partial or complete blockage of the regolith bit access windows by stones too large to pass through them. For these reasons, regolith collection sites were preferred that had a reduced probability of rocks or rubble hidden just beneath the surface, and a greater probability that all regolith components would fit through the 8 mm × 8 mm windows of the hollow regolith bit.

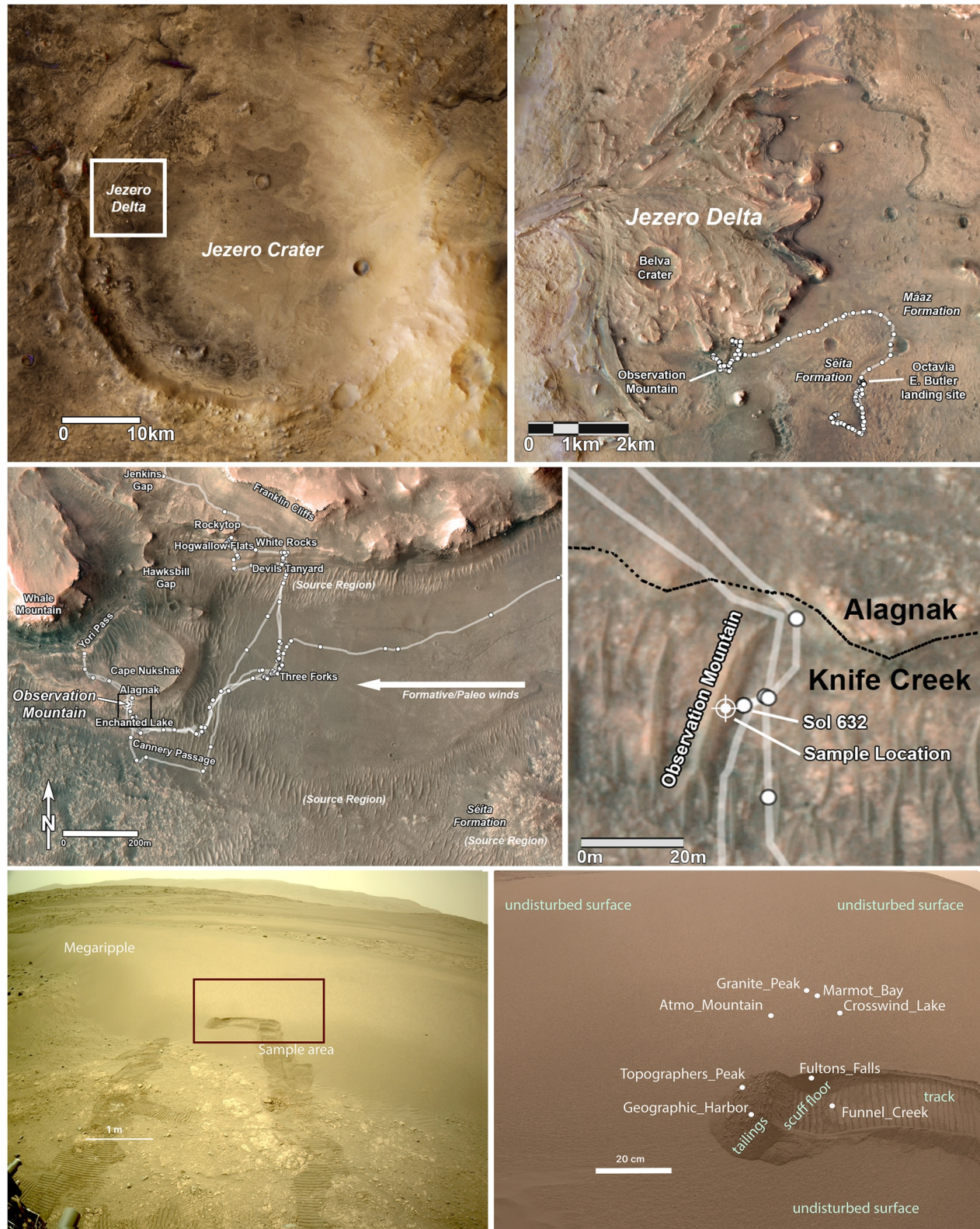


Figure 1.

The surface of a large, inactive aeolian megaripple was recognized as a setting that could reduce technical risks as well as optimize the science objectives of regolith sampling. Megaripples are aeolian bedforms comprised of poorly sorted materials (different from dunes) (e.g., Bagnold, 1941, pp. 153–157; Fryberger et al., 1992; Jerolmack et al., 2006; Lämmel et al., 2018). Volumetrically, megaripples are dominated by sand-sized grains capable of saltating along the ground during strong wind events, but they also include coarser grains that move only in short, creep-like motions, driven by high-speed impacts of the finer, saltating sand. Grain mass grows rapidly as the cube of grain radius, so the largest, creep-only grains of a megaripple have a fairly sharp cut-off maximum grain size. Bedform migration dynamics concentrate these coarsest grains at the bedform surface, especially near the megaripple's crest. This feature allows maximum grain size throughout the megaripple volume to be observed and compared with the size of the regolith bit access windows before regolith sampling might be attempted. Megaripples, like other aeolian bedforms, are perched on the ground that they migrate across; this minimizes the risk of the regolith bit colliding with subsurface rocky material. The possibility of the regolith bit colliding with a large rock buried within a megaripple was evaluated prior to sampling by assessing the size and abundance of any perched surface rocks in the area surrounding the candidate megaripple; locations where such rocks were scarce suggested lower risk and were preferred. This risk could be reduced further by choosing to sample a larger megaripple and by sampling as close to its crest as possible, thereby maximizing the megaripple thickness above the projected underlying ground plane.

The surface of a large, inactive, aeolian megaripple also offered excellent opportunities to pursue the science goals of regolith sampling. On Mars, surface water has been scarce over the last half of Martian history (e.g., Carr & Head, 2010), leaving wind transport as the dominant mode of grain transport. Figure 3 summarizes Martian aeolian transport modes as a function of grain size, and how grains could gradually evolve to smaller sizes through high-speed collisional attrition (cf. Bristow & Moller, 2018; Kuenen, 1960). Wind tunnel tests, at Mars-equivalent atmospheric pressure with low-density grains simulating Martian gravity, indicate that 80–200  $\mu\text{m}$  grains should be easiest for the wind to mobilize on Mars (Greeley et al., 1980; Iversen & White, 1982; Swann et al., 2020). Thus, grains of 80–200  $\mu\text{m}$  are most frequently mobilized into high-speed saltation trajectories where impacts with hard ground are assumed to gradually cause grain attrition by spalling off much smaller dust-sized particles. This is why the notional grain attrition history shown in Figure 3 has the most rapid reduction in grain size for these sand-sized grains. However, as grain size continues to be reduced through collisional attrition, numerical experiments show that collisional kinetic energy declines over two orders of magnitude as grain size decreases from 150 to 50  $\mu\text{m}$ , thereby greatly reducing the potential for continued attrition and slowing further evolution to smaller grain sizes (Figure 4) (see Bristow & Moller, 2018 for terrestrial comparison). This effect is primarily due to grain mass decreasing more rapidly than grain radius. Partly for the same reason, grains <150  $\mu\text{m}$  are increasingly susceptible to short-term suspension during strong wind events, thus reducing collisions during transport and further slowing grain attrition. Wheel excavations along previous rover traverses (*Opportunity* at Meridiani Planum, *Spirit* at Gusev crater, and MSL at Gale crater) have revealed that, volumetrically, grains <150  $\mu\text{m}$  are most common in near-surface regolith (Arvidson, Anderson, Bartlett, Bell, Blaney, et al., 2004; Arvidson, Anderson, Bartlett, Bell, Christensen, et al., 2004; Arvidson, Poulet, et al., 2006; Arvidson, Squyres, et al., 2006; Sullivan et al., 2005, 2008, 2011, 2020; Miniti et al., 2013; Weitz et al., 2018, 2022). Overall, these lines of reasoning are consistent with grains <100  $\mu\text{m}$  representing an evolutionary end-state in Martian regolith development. After aeolian transport reduces grain sizes to <100  $\mu\text{m}$ , further reduction in size is much more difficult, implying that many of these grains might have a long transport history.

The 50–150  $\mu\text{m}$  size range was a prime goal for regolith sampling also for compositional reasons. A review of regolith compositions at other Mars mission sites, provided in Supporting Information S1, reveals intriguing

**Figure 1.** Context of regolith sampling. Jezero crater region on Mars (top left panel) showing Jezero Fan location (inset). Top right panel depicts inset of Jezero Fan including the Octavia E. Butler landing site and the Máaz and Séítah formations relative to the *Observation Mountain* regolith sampling location. Center left panel depicts the Fan Front area with *Observation Mountain* in the west and formative/paleo wind directions and sediment source regions, including the western Séítah formation, in/from the east. Close up of *Observation Mountain* megaripple and the potential localized source region, *Knife Creek* is shown in the center right panel. Lower panels depict regolith sampling locations in Navcam (lower left, sequence ncam00301 from Sol 632), and Front Hazcam (lower right, sequence fhaz02008 from Sol 593) images. (Sol = number of Martian days since landing.) Image credits: Top left panel basemap from European Space Agency Mars Express High Resolution Stereo Camera (ESA MEX HRSC) images mosaic (Freie Universität Berlin/DLR/ESA). Image data available at <https://maps.planet.fu-berlin.de>, Lon. 77.70, Lat. 18.40. Navcam and Hazcam images were acquired from the *Perseverance* rover (<https://pds-imaging.jpl.nasa.gov/volumes/mars2020.html>). All other panel basemaps are Mars Reconnaissance Orbiter HiRISE color mosaics (Credit: NASA/JPL/University of Arizona). Base image data available in the Planetary Data System <https://pds-imaging.jpl.nasa.gov/>.

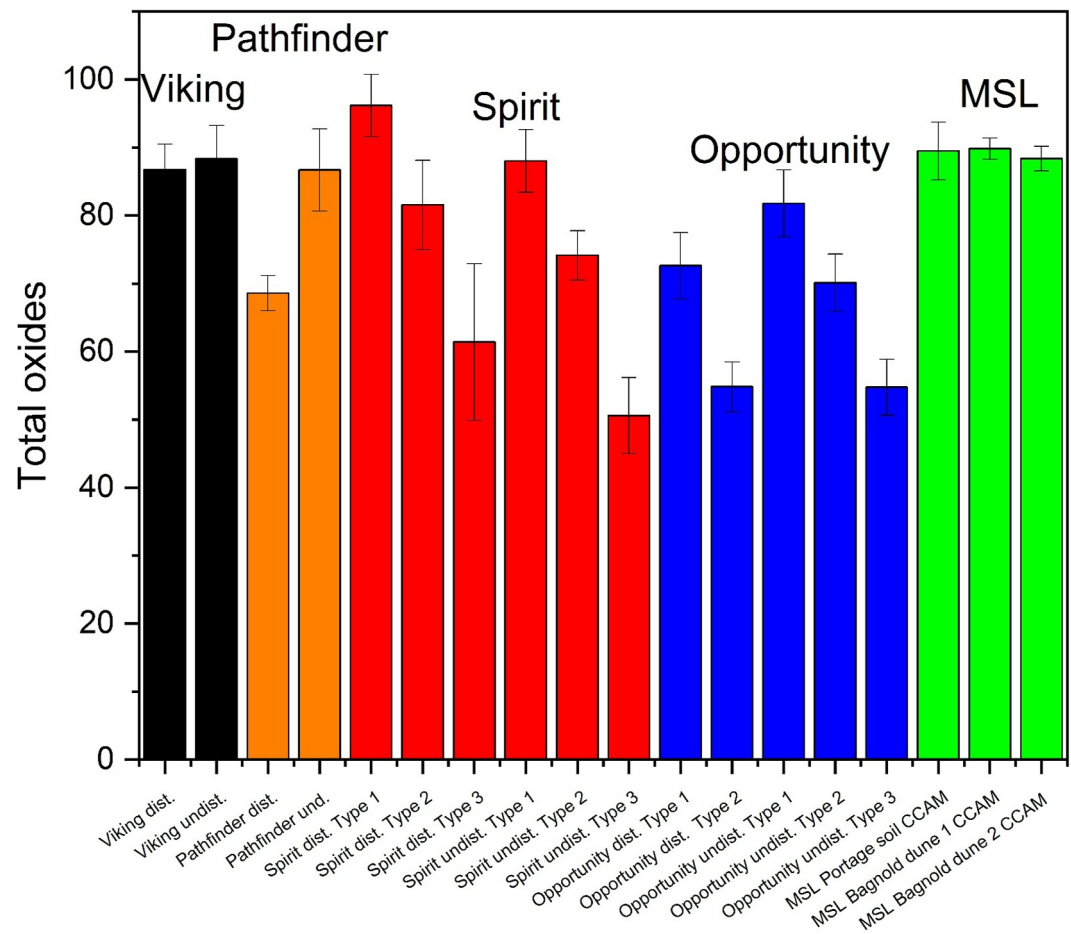


**Figure 2.** Summary of the total amount of rock-forming oxides measured for the different soils analyzed in past missions on Mars. Comparison between different soils shows the difference in the total amount of volatiles, revealing substantial differences between some of the soils. The data are contained in Tables S1 and S2 in Supporting Information S1, Table S9 and S10, and in the Planetary Data System: [https://pds-geosciences.wustl.edu/missions/mer/mer\\_apxs\\_oxide.htm](https://pds-geosciences.wustl.edu/missions/mer/mer_apxs_oxide.htm).

compositional variations, but it is important that many of these bulk compositions (e.g., at the 17–38 mm footprint resolution of a rover APXS sensor, Gellert et al., 2006, 2009) are more similar to each other, across and between mission sites, than to local rock compositions at each site (e.g., Clark et al., 1982; Yen et al., 2005; O’Connell-Cooper et al., 2017). This argues that mobility of Martian aeolian regolith particles commonly overwhelms the erosional release rate of similarly sized grains from local bedrock outcrops, so that regolith compositions duplicating the compositions of those adjacent outcrops have been rare. In addition to a possibly narrower range of source bedrock compositions on Mars compared with Earth, a long history of aeolian mobility for the dominant 50–150  $\mu\text{m}$  regolith grain size-fraction might have resulted in widespread mixing of these grains leading to similar bulk regolith compositions at many locations around the planet, yet within these mixtures individual grains have varied compositions (Clark et al., 1982; O’Connell-Cooper et al., 2017; Yen et al., 2005). For these reasons, a prime scientific goal for the Mars 2020 regolith sample was obtaining an abundance of 50–150  $\mu\text{m}$  grains as an important representative of a possible global Martian regolith unit. Previous experience has shown that the interiors of Martian megaripples are dominated by this size-fraction (e.g., Arvidson, Anderson, Bartlett, Bell, Blaney, et al., 2004; Arvidson, Anderson, Bartlett, Bell, Christensen, et al., 2004; Arvidson, Poulet, et al., 2006; Arvidson, Squyres, et al., 2006; Cabrol et al., 2014; Herkenhoff et al., 2008; Jerolmack et al., 2006; Soderblom et al., 2004; Sullivan et al., 2005, 2008, 2011, 2022; Weitz et al., 2018, 2022).

Dust-sized grains could represent physically irreducible regolith particles, and are a fundamental regolith component for sampling. Dust particles are lofted into suspension during strong wind events, including by strong winds around the core of low-pressure vortices (or “dust devils”) in which “suction” and other effects may also

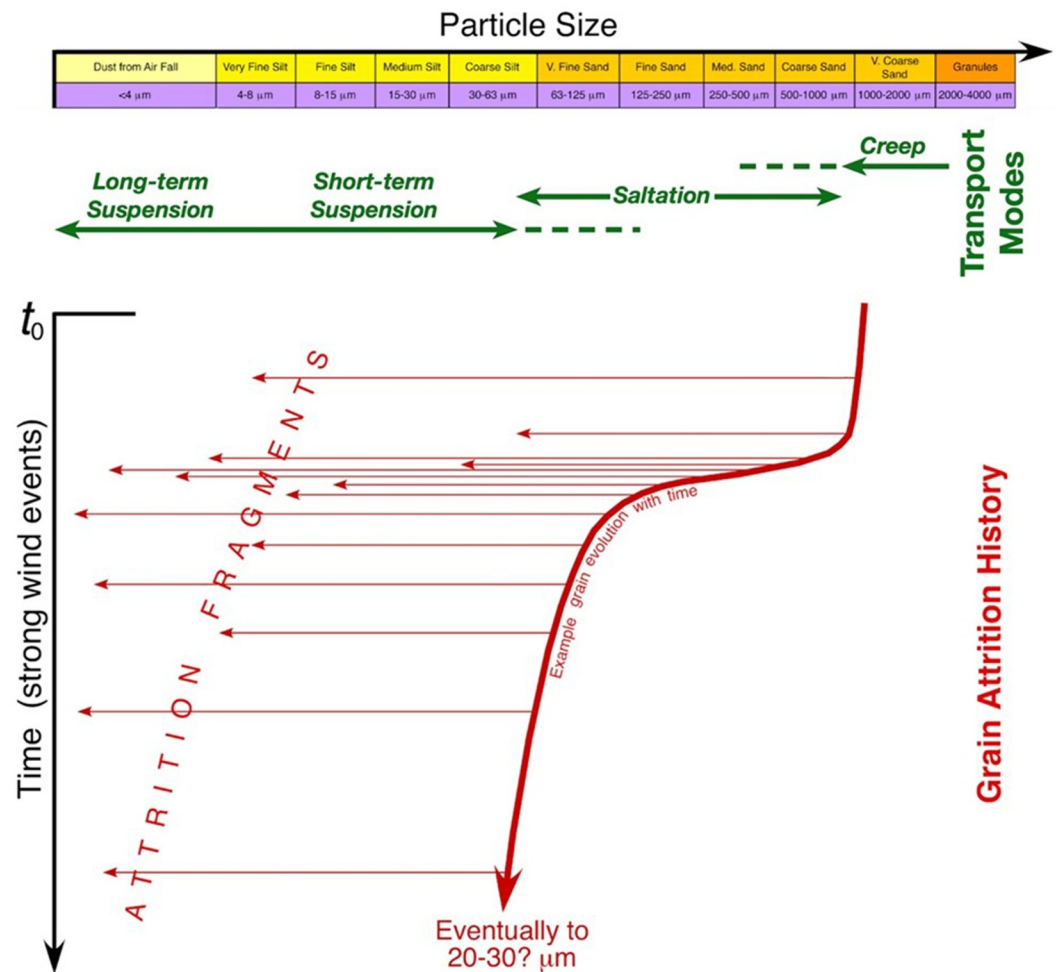


**Figure 3.** Regolith particles smaller than a few mm have been susceptible to aeolian transport during long arid periods of Martian history. Aeolian abrasion very likely plays a dominant role in the evolution of regolith particles toward smaller sizes. This process accelerates as grain size reduces to 80–200  $\mu\text{m}$ , the size range that wind tunnel experiments indicate should be the easiest to mobilize (Greeley et al., 1980; Iversen & White, 1982; Swann et al., 2020). The rate of grain size reduction then probably slows as decreasing grain size reduces collisional kinetic energy (Figure 4), and short-term suspension becomes the more likely transport mode. Attrition products contribute to the population of dust and finer silt within the regolith (notional horizontal arrows).

help to raise dust (e.g., Neakrase et al., 2016). During major storms, dust particles can circulate for weeks before settling back to the ground (e.g., Cantor, 2007; Guzewich et al., 2019). Numerous global dust storm events over the last half of Martian history imply that dust-sized components within a regolith sample could have been sourced from rock units anywhere around the planet, and represent an essential component of the global regolith unit. However, targeting a dust mantle at Jezero for sampling by the regolith bit was not practical. Visible dust mantles on regolith are uncommon at Jezero, found only in small, wind-protected areas, such as within complex crest topography of the largest megaripples. Such locations generally were not reachable by the rover. As an alternative, dust grains infiltrating the near-subsurface pore space were relied upon for sampling. As an example of subsurface dust present in a relatively non-dusty surface environment, Figure 6 shows a wheel trench into aeolian sands on the floor of Eagle crater at Meridiani Planum. Like Jezero, Meridiani Planum is a relatively low dust site, with rare continuous dust mantle deposits found only in protected areas (not shown). Wheel track fidelity on the surface in Figure 6 shows no evidence of surface dust. However, wheel tracks on disturbed subsurface material (e.g., trench floor and tailings) have higher fidelity and higher albedo, indicating the presence of abundant very fine particles that had previously infiltrated the near-subsurface regolith.



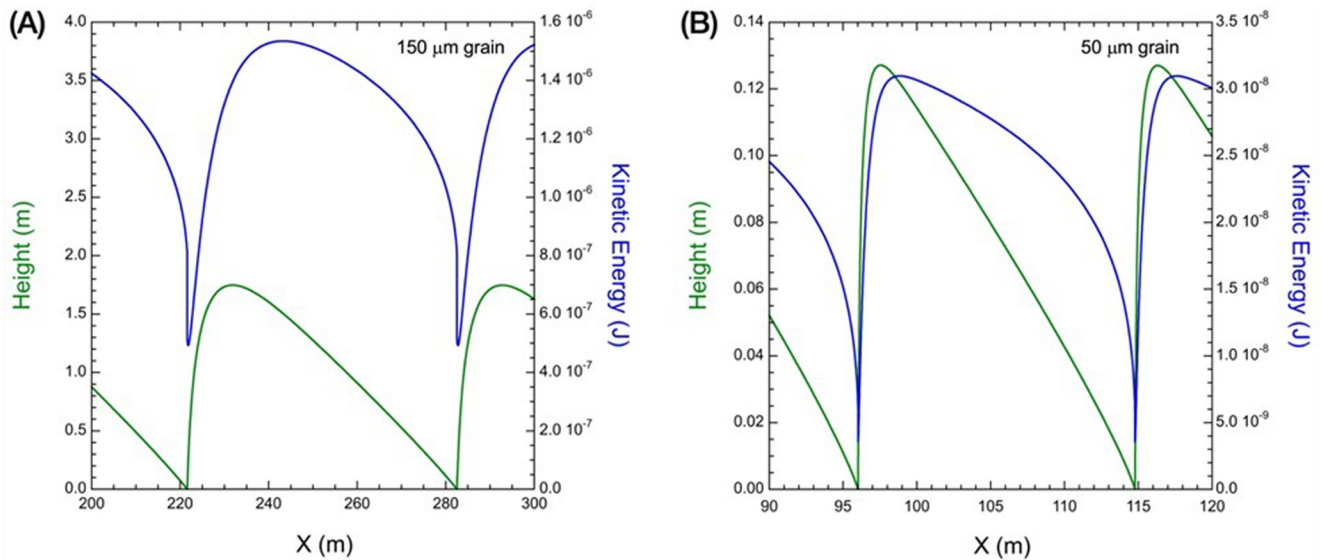


**Figure 4.** Numerical experiments of equilibrium saltation trajectories (Grainwind.c; Sullivan & Kok, 2017) over hard ground (bounce coefficient 0.8) show how grain kinetic energy at rebound decreases by two orders of magnitude as grain size decreases from 150 to 50  $\mu\text{m}$ . So as grain size decreases, the rates of grain attrition and grain size reduction should slow. Green curves are grain trajectories. Test conditions: atmospheric pressure  $P = 6.7$  mb, temperature  $T = 250^\circ\text{K}$ , aerodynamic roughness  $z_0 = 0.0001$  m, wind friction speed  $u_* = 1.0$  m/s (equivalent to wind speed  $u \sim 24$  m/s at height  $z = 1.5$  m), and constant bounce rebound angle of  $50^\circ$ . Note different vertical exaggeration between 150  $\mu\text{m}$  case (a) and 50  $\mu\text{m}$  case (b). Purple curves are KE. KE of 150  $\mu\text{m}$  grain at rebound  $\sim 5 \times 10^{-7}$  J. KE of 50  $\mu\text{m}$  grain at rebound  $\sim 4 \times 10^{-9}$  J.

For megaripples at Jezero, the abundance of dust particles within near-subsurface pore space was expected to correlate inversely with bedform activity. This prompted a search to identify the least active, most indurated megaripple surfaces that might be available for sampling. This search was motivated also by the desire to sample compositional components of fully developed cohesive surface crusts (even though such crusts would be broken up by the action of the regolith bit). Previous lander and rover missions have observed that light cohesion is a pervasive characteristic of Martian regolith (e.g., Arvidson, Anderson, Bartlett, Bell, Blaney, et al., 2004; Arvidson, Anderson, Bartlett, Bell, Christensen, et al., 2004; Arvidson, Poulet, et al., 2006; Arvidson et al., 2009; Clark et al., 1982; Moore et al., 1987; Sullivan et al., 2011; Weitz et al., 2020), including at Jezero where cohesive surface crusts are very common (Hausrath et al., 2023). Development of surface cohesion probably involves exchanges of volatiles between the atmosphere and near-surface regolith (e.g., Hausrath et al., 2023; Ming et al., 2006; Wang et al., 2006, 2008). Understanding these processes better was an important science goal for regolith sampling.

Guidance for identifying inactive megaripple surfaces at Jezero was obtained from: (a) observations that megaripples with distinct surface characteristics did not migrate during one or more strong, sand-driving wind event(s) associated with a regional dust storm that began around Sol 313 of the mission (Lemmon et al., 2022), while other megaripples in the same area did migrate; (b) evaluation of the uniquely complex crests of large Jezero megaripples; and (c) previous terrestrial work comparing lee versus stoss (windward) megaripple flanks.

A regional dust storm passed over Jezero beginning around Sol 313, and was associated with strong winds and active dust lifting (initially by both linear wind gusts and vortices) (Lemmon et al., 2022). This aeolian activity was strong enough to saltate large quantities of sand on to the rover deck, to damage the MEDA (Rodríguez-Manfredi et al., 2021) wind sensors, and to cause some megaripples close to the rover to migrate (Lemmon et al., 2022). This is the first known instance of Martian megaripple migration observed in situ, although megaripple migration elsewhere on Mars has been previously observed from orbit (Silvestro et al., 2020). However, other megaripples in the same area with more rounded crests and somewhat coarser surface grains did not migrate during the same period, and their surface grains remained stable (Movie S1). Grain size measurements (Figure 7) reveal that megaripple surfaces covered with  $< 2$  mm grains were active, while surfaces that included abundant coarser grains, commonly up to 3 mm, were not. Thus, a stable, inactive megaripple desirable for future regolith sampling could be identified by having an abundance of grains  $> 2$  mm on its surface.

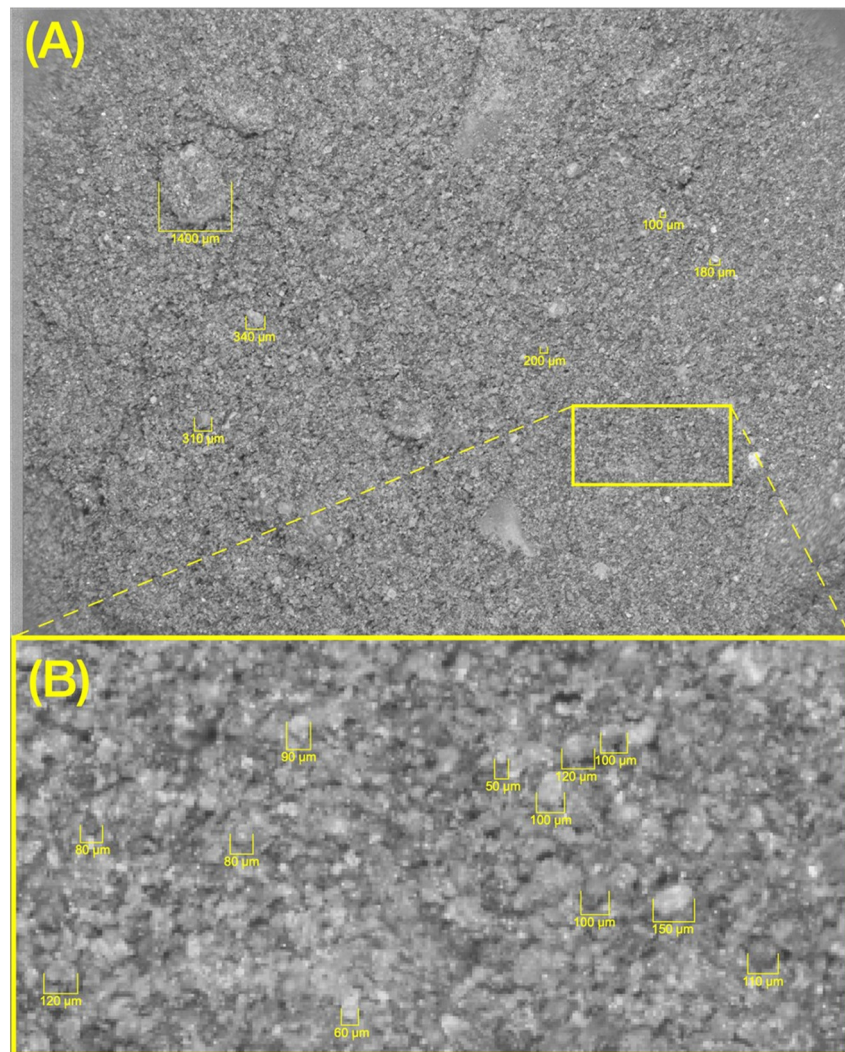


**Figure 5.** (a) This Sol 598 Autofocus Context Imager image is a  $10.1\ \mu\text{m}/\text{pixel}$ , flat-fielded, focus-merge view of the tailings pile (Topographers Peak) created by a wheel scuff into the *Observation Mountain* megariipple regolith collection site (sequence srlc10402). The bulk of the two regolith samples (*Atmo Mountain* and *Crosswind Lake*) are composed of similar material that is mostly  $<150\ \mu\text{m}$  (see also Section 3.2 and Figure 15). (b) Close inspection reveals bright  $10.1\ \mu\text{m}$  pixels scattered throughout; these likely represent bright dust grains or aggregates of dust, many of which might not fully span the dimensions of each pixel.

Megariipple crest morphology provided a second indicator of relative inactivity. Many of the largest megariipples along the Mars 2020 traverse have complex crest morphologies not seen previously on Mars or, to our knowledge, on Earth (Figure 8). These morphologies typically involve smaller secondary megariipples with sharper, more sinuous crests perched near but commonly not centered along the main megariipple crest. The secondary megariipple crests seem to represent reactivation of only part of the surface population of coarse grains (likely  $<2\ \text{mm}$ ) “harvested” from the original megariipple surface. In this interpretation, most of the population of Jezero megariipples near the rover’s Prime Mission traverse grew to enormous sizes visible from orbit. However, at some later stage, perhaps after a period of inactivity, strong wind events became characterized by somewhat weaker sand flux (involving reduced atmospheric density, reduced peak wind strengths, and/or smaller available sand grains saltating from upwind). This reduced sand flux has been capable of moving mostly  $<2\ \text{mm}$  grains, harvesting these grains from the original coarse grain population of megariipple surfaces to form the secondary megariipples. On this basis, crest complexity on large megariipples indicates greater age and inactivity, where effects of atmosphere-regolith interactions (e.g., crust development) are likely to be well-developed.

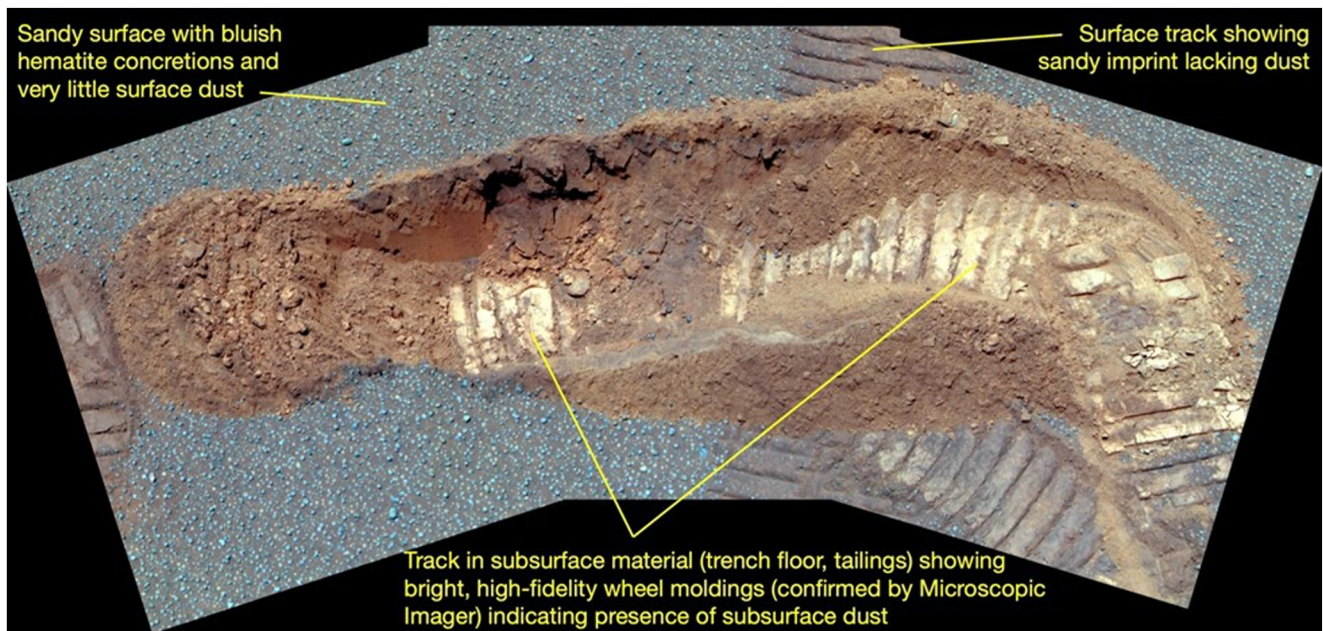


**Figure 6.** MER *Opportunity* rover color-stretched Pancam mosaic of a wheel trench on the floor of Eagle crater at Meridiani Planum, from the 26th Sol of that mission. Like Jezero crater, the Meridiani Planum landing site has relatively little surface dust, with dust mantles present only in areas well-shielded from wind. However, trench wheel track morphology and albedo indicate the presence of dust in the near-subsurface. Wheel track is 16 cm across for scale. This enhanced-color mosaic was acquired on Sol 26, Pancam sequence ID 2385, using Pancam 753, 535, and 432 nm filters. Data for the *Opportunity* mission are available on the Planetary Data System: <https://pds-geosciences.wustl.edu/missions/mer/index.htm>.

Finally, megarripple migration involves accumulation of grains on the lee side, simultaneously with erosion of grains from the stoss (windward) side. For this reason, surface material exposed on the stoss side will have been in place longer than material exposed on the lee side surface. While not the most important factor when a given megarripple has become indurated and stable, nevertheless stoss sides were preferred for regolith sampling.

To summarize, regolith sampling site criteria that would minimize technical risks and address science goals included: the stoss slope of a large megarripple displaying complex crest morphology and abundant >2 mm surface grains, with the surrounding area having few surface boulders. Figure 1 shows the location of the megarripple selected for sampling, designated “*Observation Mountain*.” The *Observation Mountain* megarripple is located at the *Enchanted Lake* section of the *Shenandoah* formation (Stack et al., 2024). The section was targeted between investigations of the *Amalik* member (fine-grained sandstone) and *Alagnak* member (coarse-grained sandstone) next to the *Knife Creek* member (mudstone) (Stack et al., 2024).

Data from the Mars 2020 science payload were acquired at *Observation Mountain* to provide scientific context for the regolith samples (two samples were acquired, intended as compositional and textural twins), analogous to contextual data sets acquired for all rock samples. Previous observations on other missions showed that Martian regolith right at the surface generally is different, either in composition, grain size-frequency, or both, from regolith in the near-subsurface (e.g., Arvidson, Anderson, Bartlett, Bell, Blaney, et al., 2004; Arvidson, Anderson, Bartlett, Bell, Christensen, et al., 2004; Arvidson, Poulet, et al., 2006; Arvidson, Squyres, et al., 2006; Arvidson et al., 2010; Minitti et al., 2013; Stein et al., 2018; Sullivan et al., 2011; Wang et al., 2006, 2008; Yen et al., 2008). Near-subsurface materials would compose most of the collected regolith sample volume (Section 2.3). On this basis it was desirable to make subsurface regolith accessible to the science payload, to provide relevant scientific context for the regolith samples. This was facilitated by digging a small wheel-scuff trench (e.g., Sullivan et al., 2011). Trenching created a “roadcut” exposure that displayed an in situ soil depth profile (Figure 10, target “*Fultons Falls*”). The arm turret is too bulky to fit down into a wheel-scuff trench (although 34–98  $\mu\text{m}/\text{pixel}$  Wide Angle Topographic Sensor for Operations and eNginEering [WATSON] images were obtained), so remote-sensing instruments Mastcam-Z (Bell et al., 2021; Hayes et al., 2021) and Supercam (Maurice et al., 2021; Wiens, Maurice, Robinson, et al., 2021) recorded compositional and physical properties of the trench wall and interior (Sections 3.1 and 3.3–3.5). For proximity science instruments mounted on the arm, the tailings pile of the

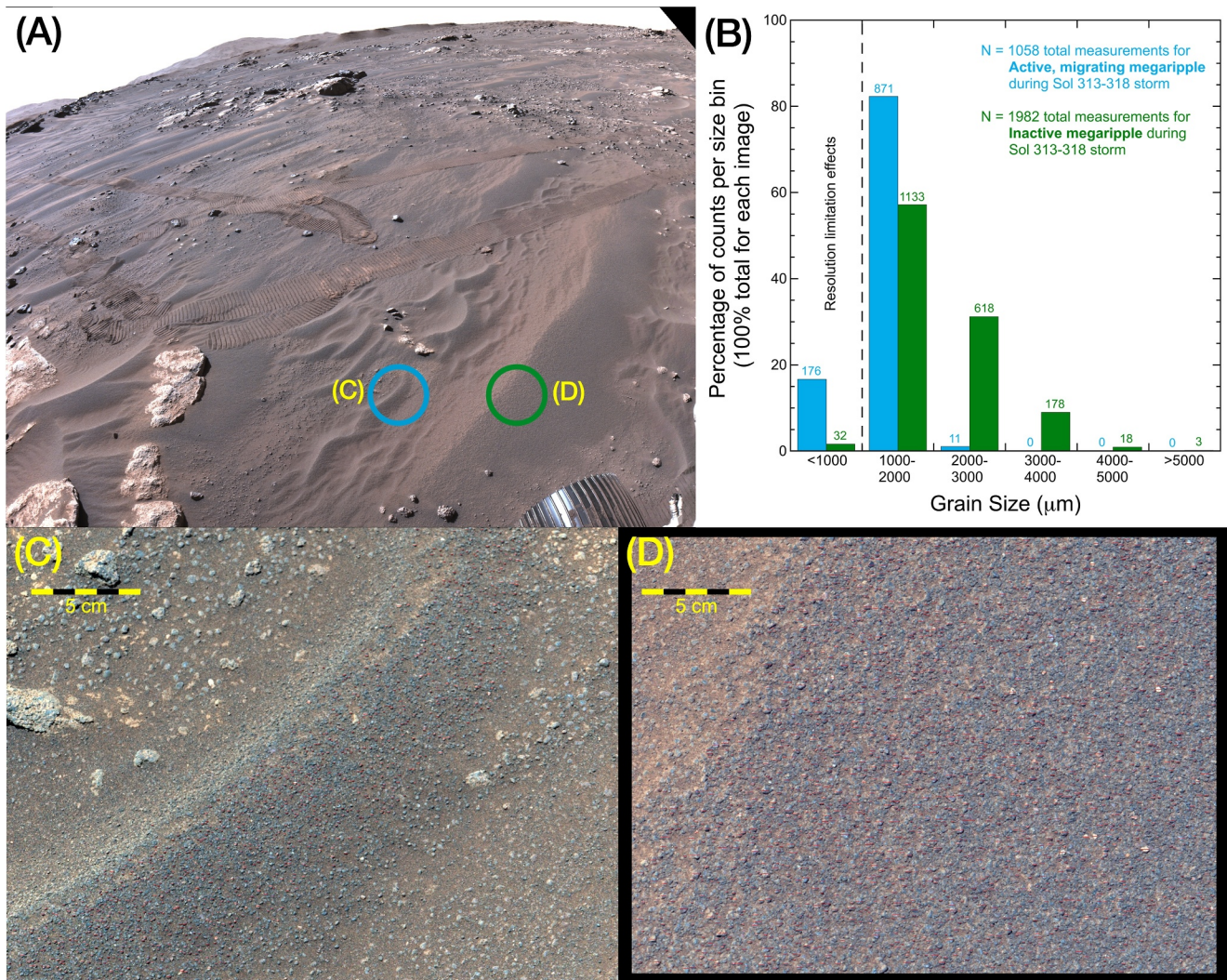


**Figure 7.** Comparison of grain sizes between active and inactive megaripples during the Sol 313–318 regional storm. See Movie S1, which compares Navcam views from sol 286 sequence ncam03286, and sol 321 sequence ncam03321, and shows surface effects of the Sol 313–318 regional storm. (a) Sol 286 Navcam (ncam03286; Maki, Deen, et al., 2020) view of megaripples showing locations of panels (c) and (d). Movie S1 shows megaripple migration at (c), and a stable megaripple surface at (d) (including individually stable surface grains). (b) Grain size-frequency measurements presented as percentage of grain counts per size bin, for the active (blue) and inactive (green) megaripples. Panels (c) and (d) are the Mastcam-Z images utilized in the measurements (individual grain spans are shown in red on each pane, so are seen more easily by magnifying the figure) (Sol 312, sequence zcam08336). The images were obtained at slightly different ranges from the camera, so the image in pane D has been reduced in size proportionally to present both images at the same scale.

wheel scuff (Figure 9, target “*Topographers Peak*”) provided an accessible target of subsurface material, having sufficient positive relief to allow close approach by WATSON and SHERLOC (Bhartia et al., 2021), and PIXL (Allwood et al., 2020). The tailings pile also served as an additional remote-sensing target (Sections 3.1, 3.4, and 3.5). The MEDA suite of meteorological instruments (Rodríguez-Manfredi et al., 2021) monitored environmental conditions during regolith sample collection and evaluated thermal inertia (TI) of the *Observation Mountain* stoss flank (Section 3.6).

The two regolith samples from *Observation Mountain* were the last to be collected before the rover proceeded to the Prime Mission “Three Forks Depot” caching site. However, the penultimate “*Mageik*” rock sample, acquired before traversing to *Observation Mountain*, failed to seal properly on-board. This caused an extended delay between when most of the scientific context data for *Observation Mountain* were acquired (Sols 593–606) and when actual collection of the regolith samples (*Atmo Mountain* and *Crosswind Lake*) and final scientific context observations were conducted (Sols 632–641). The *Atmo Mountain* regolith sample was collected on Sol 634, and

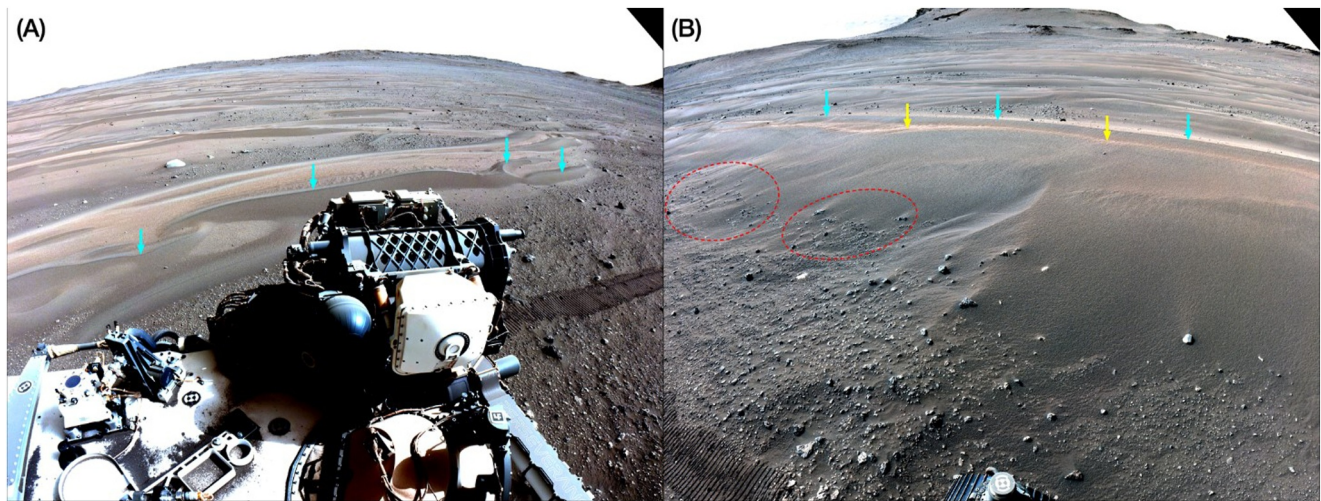


**Figure 8.** Two Navcam views from Sol 538 (ncam03538) show examples of complex megaripple crest morphology, an indicator of megaripple induration and stability. (a) Looking into the formative sand-driving wind direction, several smaller, somewhat darker, sharp-crested, sinuous secondary megaripples have migrated from the crest area of the largest megaripple closest to the rover down the lee side (toward the viewer), partly into the wind shadow of the main crest, so perhaps partly stalling there (blue arrows). (b) Looking in the downwind direction of formative sand-driving winds (note well-developed wind tails streaming from rocks, encircled in red), a small fraction of the original large megaripple surface is interpreted to have been “harvested” to form a smaller secondary megaripple (blue arrows) that has moved away from the viewer, partly into the wind shadow beyond the main crest. The protected area between the main, older megaripple crest and the smaller secondary megaripple beyond hosts a narrow mantle of bright dust (yellow arrows). Unfortunately, dust mantles in positions like these were not directly reachable by the rover.

*Crosswind Lake* on Sol 639. On Sol 641, the rover drove toward the Three Forks sample cache location, where *Crosswind Lake* was deposited as part of a 10-sample tube depot. *Atmo Mountain* remains aboard the rover for deposition as part of a more extensive cache later in the mission. Table 1 lists observations collected by each of the instruments, and analyses are reported in Results Section 3.

The *Observation Mountain* megaripple satisfied the regolith sampling site criteria and associated scientific goals. (a) *Observation Mountain* displays complex crest morphology (Figure 9), consistent with long-term stability and induration of the stoss side, where sampling occurred. (b) The standing exposure of the wheel-scutt “roadcut” indicates cohesion in the near-subsurface (Figure 10). (c) An Autofocus Context Imager (ACI) image of disturbed subsurface material (the wheel scuff tailings pile, target “*Topographers Peak*”) is comprised mostly of the crucial 50–150  $\mu\text{m}$  grain size range (Figures 5 and 15, Section 3.2) that also likely comprises most of the volume of the *Atmo Mountain* and *Crosswind Lake* regolith samples. (d) Numerous bright 10.1  $\mu\text{m}$  pixels in the same view very likely represent bright dust grains or aggregates of these, many of which probably do not fully fill the dimensions of each pixel. (e) Coarse, creep-only grains  $>2$  mm were distributed across the megaripple surface (Figure 11), and on-board Cachecam images (Maki, Gruel, et al., 2020) show some of these very coarse grains at the top of the *Atmo Mountain* sample, and hints of similar coarse material near the top of the *Crosswind Lake* sample (Figure 12).

## 2.2. Regolith Sample Acquisition Process

Regolith sampling is performed by the rover's Sampling and Caching Subsystem (SCS). This system consists of a robotic arm with a rotary percussive drill on the end, and a suite of assemblies inside the body of the rover to store and manipulate drill bits and sample tubes (Moeller et al., 2021). The system was primarily designed to collect core samples from consolidated rock, and the intent of the regolith collection process was to function as similarly as possible to that operation. To that end, any of the sample tubes can be used to collect either a rock core or regolith sample.

The regolith bit is the only unique hardware involved in the regolith sampling process (compared with rock sampling). The bit is made of titanium alloy, and the interior and exterior surfaces are nitrided (Moeller et al., 2021). The internal features that interact with the sample tube and the rear features that interact with the drill are identical to those on the coring bit. The internal features hold the sample tube, while the rear features interact

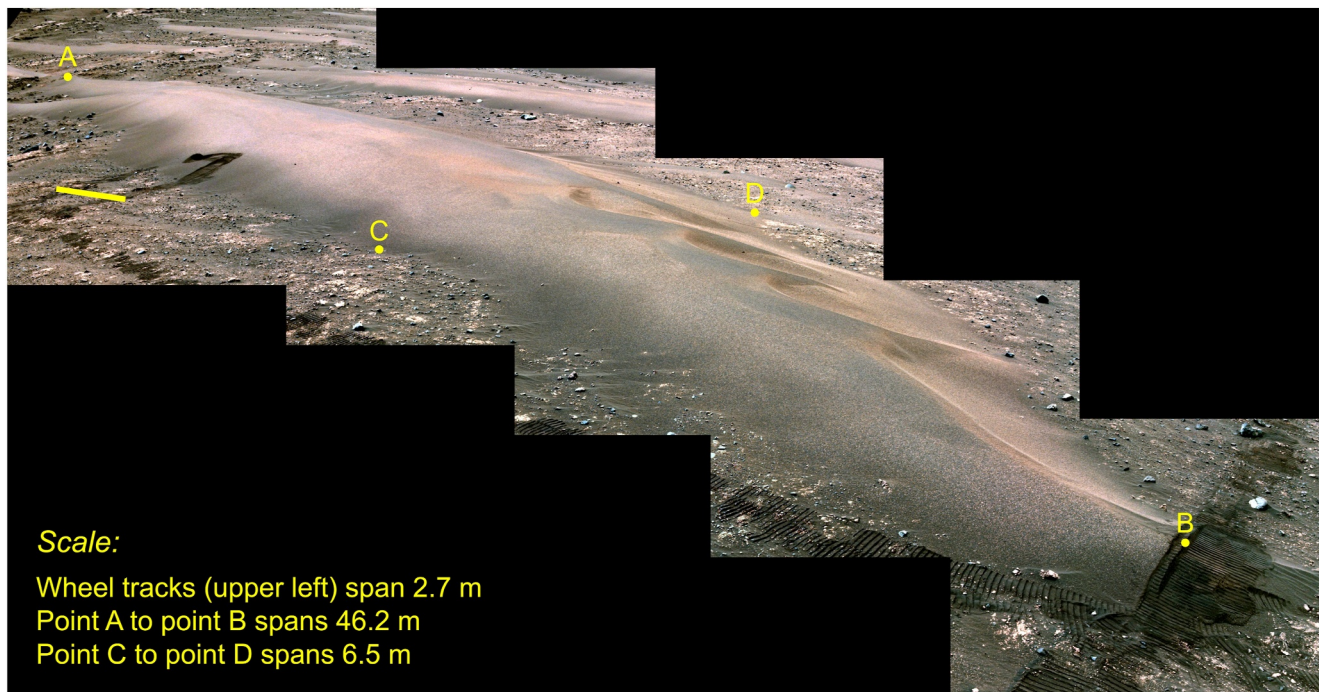


**Figure 9.** Sol 632 color-stretched Navcam (Maki, Gruel, et al., 2020) image tiles (ncam00430), obtained after the *Mageik* rock core sealing anomaly was resolved and the rover was returning to *Observation Mountain* to finish regolith collection. The stoss (dominantly upwind) side of the megaripple is facing the rover. Smaller secondary megaripples have developed from the original large bedform, resulting in crest complexity. The rover carried out the first part of regolith sampling (Sols 593–606), accomplishing most of the science context observations, at the wheel trench site at upper left (where the rover returned, Sols 632–641, to complete sampling). At upper left, near the trench site, the megaripple crest is distorted by a long secondary megaripple that has migrated to the right and partly down into the wind shadow of the original megaripple crest, suggesting stability of the original megaripple stoss surface where the two regolith samples were acquired.

with the drill chuck, spindle, and percussion mechanisms. The unique features are on the front of the bit: (a) the front is hollow but enclosed, except for two small openings on the side; and (b) there is a tooth at the tip (Figure 13). The openings are sized so that any grain entering the bit will fit in the sample tube. The internal volume under the openings is  $8 \text{ cm}^3$ , the desired volume of sample to collect.

Regolith sampling operations begin by using the SCS to load a sample tube into the regolith collection bit, and present the bit to the exterior of the rover. The regolith bit (with sample tube) is then picked up using the robotic arm and drill. The drill is then positioned above the target location. Although rock core collection involves contacting the drill stabilizers to the surface of a rock, regolith collection hovers the drill above the surface and only contacts the surface with the bit.

When the drill is positioned above the target, the drill feed extends the bit until it contacts the surface. Due to the shape of the bit tip, this is not done using sensing; instead, previous images and positioning accuracy are relied upon. The bit is then inserted down into the regolith using the feed, rotation, and percussion motions, to a target depth of 65 mm for the tip of the bit (leaving the windows at less than 65 mm depth). At the target depth, rotation and percussion continue while the turret rotates on the wrist of the robotic arm,  $5^\circ$  in each direction. This causes the bit to sweep through the regolith. The rotation, percussion, and sweep all act to liquify the surrounding regolith and encourage material to flow into the hollow bit through the two access windows. Without all of these activities, it is possible in some types of regolith for the material to be compacted away from the bit and form consolidated walls, resulting in insufficient collected sample. Throughout these sampling activities, the robotic arm and drill sensors are monitored. Any spike in force or current that could be caused by a submerged rock or higher than expected regolith consolidation will cause the rover to stop motion until assessment by rover engineers verifies it is safe to resume.

After the sweep motions are completed, percussion stops and the drill retracts the bit from the regolith. The robotic arm moves the drill away from the surface and points it down relative to gravity. A short burst of percussion is then used to level the sample, so that any material stuck to the outside of the bit or that was above the

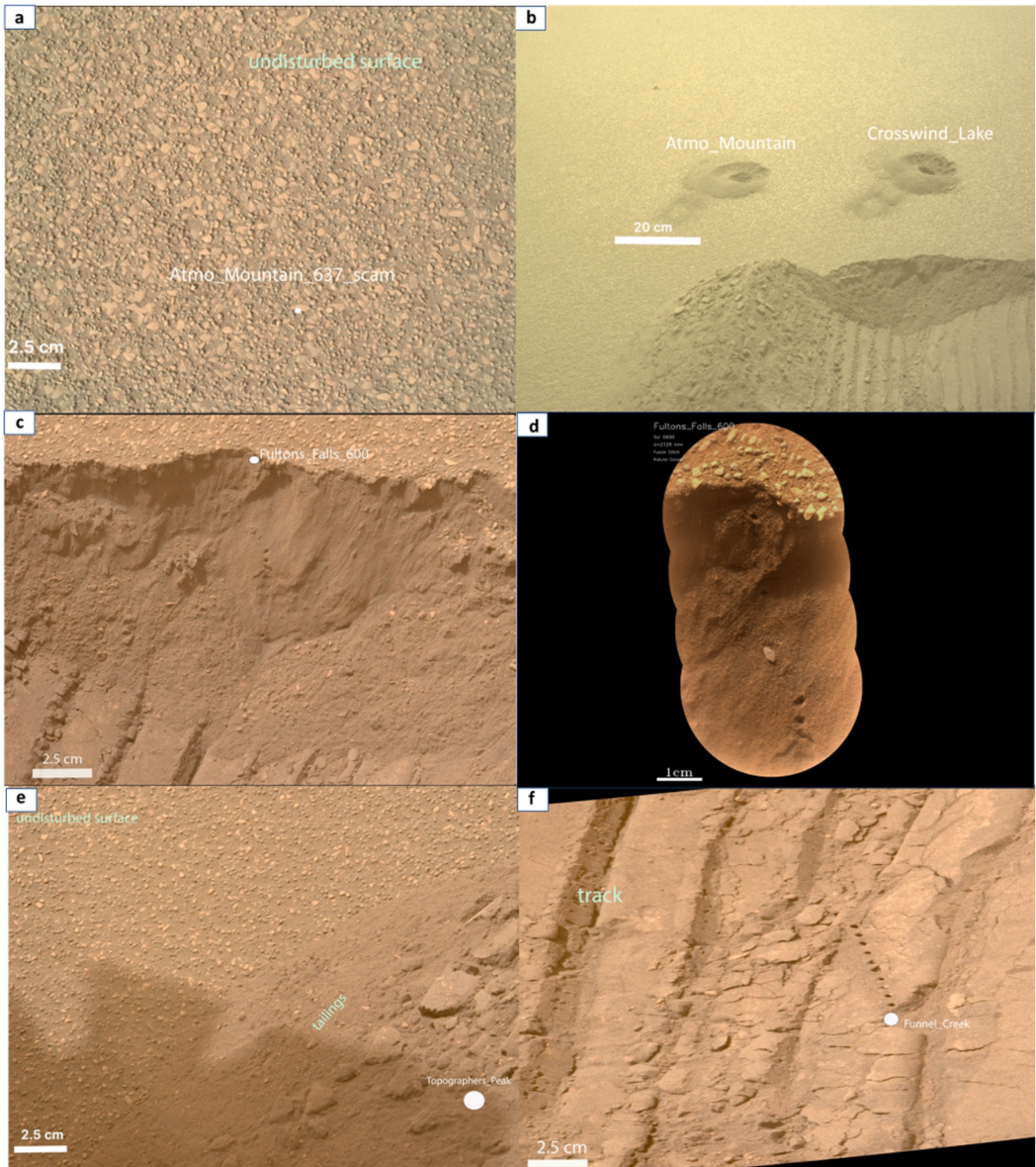


Figure 10.

windows in the bit is expelled. This prevents overfilling the sample tube. The sampling process means that the grains are mixed during sampling, and not retained as an intact depth core.

The turret then begins moving the bit to point up relative to gravity, ensuring the windows point in the direction of motion so no sample is spilled. This inversion combined with intermittent percussion encourages the sample to flow from the tip of the bit into the sample tube.

The bit and tube are then returned to the interior of the rover, where the tube is removed from the bit, imaged by Cachecam (Maki, Gruel, et al., 2020), and sealed. Unlike rock coring, no volume assessment is performed—a volume estimate is obtained solely from the images.

### 2.3. Regolith Sample Acquisition Process Laboratory Experiments

To test the depth beneath the megaripple surface from which the regolith samples were collected, as well as the extent of collection of coarse surface grains and finer, subsurface material, experiments were performed at JPL using the Vehicle System Test Bed (VSTB). These experiments revealed that, during the laboratory sampling, both the fine-grained material beneath the surface, and the coarser material at the surface were sampled, and that maximum depth of sampling was 4–6 cm beneath the surface.

In order to capture different aspects of the natural Martian soil environment, two experiments were performed, referred to as the “jewelry box” and the “chocolate cake” (Figures S2 and S3 in Supporting Information S1). The “jewelry box” experiment was prepared by filling a test bin with a mixture of <2 mm Mojave Mars Simulant sand mixed with MMS dust (Peters et al., 2008). During the filling process, mono-layers of 2 mm glass beads, each mono-layer a different color, were emplaced at 2 cm depth increments within the sand. The “chocolate cake” experiment consisted of two layers of sieved MMS. A 4 cm-thick surface layer of 500–2000  $\mu\text{m}$  sieved sand overlay <500  $\mu\text{m}$  material, so that the collected sample could be re-sieved to determine the amount of material extracted from each layer. Each layer was compacted by light compression before placing the next layer upon it.

The horizontal, layered “jewelry box” and “chocolate cake” were sampled by VSTB using the same sequence of events as the sampling performed on Mars. The laboratory results suggest that on Mars the regolith is sampled to a depth of at least 4 cm, but no deeper than 6 cm, and that substantial amounts of both the grains at the surface and material from all depths to 4–6 cm is sampled (Table S9).

### 2.4. Measurements Associated With Sampling

The Standardized Observation Protocol (STOP) list details the measurements to be made for each sample (Simon et al., 2023). The STOP list varies slightly for each sample, and the detailed STOP list for each sample is listed as part of the Sample Dossier on the Planetary Data System (PDS) (Farley & Stack, 2023c) and a detailed list of the regolith sampling activities are given in Table S12. The measurements associated with regolith sampling are given in Table 2.

**Figure 10.** Regolith sampling location. (a) WATSON image acquired at 40.7 cm standoff of *Atmo\_Mountain\_637\_SCAM* showing the undisturbed surface on Sol 633, sequence id srlc04004. (b) Front Hazcam of *Atmo Mountain* and *Crosswind Lake* sampling holes, sequence id fhaz05001. (c) Mastcam-Z image showing soil crust similar to those that have been observed on the Jezero crater floor and elsewhere on Mars on Sol 596, sequence id zcam03464. (d) Natural color SuperCam Remote Micro-Imager (RMI) of *Fultons\_Falls\_600* on Sol 600 (sequence id scam01600) showing the crust and fine to coarse-grained material. (e) Mastcam-Z image of *Topographers Peak* showing a portion of the tailings on Sol 606, sequence id zcam08609. (f) Mastcam-Z image of *Funnel Creek* showing disturbed/compressed soils from rover wheels, sequence id zcam03466. Also shown is the *Funnel Creek* SuperCam 10-position raster (holes in regolith from Laser Induced Breakdown Spectroscopy (LIBS) measurements) on Sol 602. Hazcam (<https://pds-imaging.jpl.nasa.gov/volumes/mars2020.html>), WATSON (Beegle et al., 2021), Mastcam-Z (Bell et al., 2021) and RMI (Wiens, Maurice, Deen, et al., 2021) data are available on the Planetary Data System. (a) SHERLOC Imaging (WATSON) of *Atmo Mountain*; Activity ID: 1e680a3a-1491-4430-b23b-1161bbb728b6, sequence ID: srlc04004 (b) ECAM Front Hazcam Left (RCE-A); Activity ID: 356f02f1-83b1-42a1-a0e6-450a3625f596, sequence ID: fhaz05001 (c) Mastcam Z Left of *Fulton\_Falls\_600*; Activity ID: f274f245-39ad-48fc-b8bf-75c7d6d3979c, sequence ID: zcam03464 (d) SuperCam 1  $\times$  10 D VISIR LIBS MIC RMIS *Fulton\_Falls\_600*; [https://pds-geosciences.wustl.edu/m2020/urn-nasa-pds-mars2020\\_supercam/data\\_special\\_rmi/sol\\_00600/ascam\\_sol0600\\_scam01600\\_mos\\_fr08\\_aft\\_rgb\\_lri\\_fultons\\_falls\\_600\\_p01.png](https://pds-geosciences.wustl.edu/m2020/urn-nasa-pds-mars2020_supercam/data_special_rmi/sol_00600/ascam_sol0600_scam01600_mos_fr08_aft_rgb_lri_fultons_falls_600_p01.png) (e) Mastcam Z Left of *Topographers\_Peak*; Activity ID: bf368239-f18c-48e5-853c-3b88042b5efb, sequence ID: zcam08609 (f) Mastcam-Z Mosaic *Funnel Creek*; s3://m20-sops-ods/ods/surface/sol/00602/ids/rdr/mosaic/LZLRGB\_0602\_RAS\_0300000\_CYL\_S\_BLFUNLCJ01.IMG.



**Table 1**  
*Summary of Measurements Collected of Observation Mountain Associated With the Regolith Sample From Sols 593–641*

Instrument	Data collection	Targets <sup>a</sup> assessed
Mastcam-Z	Stereoscopic color, zoom, and multispectral imaging to assess texture, color variability, and VNIR spectral characteristics	Granite Peak (undisturbed surface), Topographers Peak, Fulions Falls, Crosswind Lake sample tailings (disturbed surfaces)
SuperCam	LIBS, VIS/IRS, Microphone, RMI	Granite Peak, Fulions Falls, Geographers Harbor, Funnell Creek, Atmo Mountain, Crosswind Lake
WATSON	High-resolution imaging	Fulions Falls, Marmot Bay, Atmo Mountain, Crosswind Lake, Topographers Peak, Goodness Bay
PIXL	X-ray spectra, diffraction data, micro-context camera spectra	Marmot Bay (undisturbed surface), Topographers Peak (disturbed surface)
SHERLOC	Raman and fluorescence spectra, Autofocus Context Imager (ACI) high resolution imaging	Marmot Bay (undisturbed surface), Topographers Peak (disturbed surface)
MEDA	Periodic observations of ambient P, T, and RH of the air; measurement of incoming and outgoing thermal radiation and outgoing solar radiation (yielding the T surface) using the Thermal Infrared Sensory (TIRS)	Surface temperature of the ground temperature sensor Field of View (see image 25). Near-surface P, T and RH; dust accumulation on the windows of the photodiode

*Note.* For more detailed measurements please see the table of Observation Mountain Sampling activities (Table S10) as well as the Sample Dossier on the PDS (Farley & Stack, 2023c). <sup>a</sup>For locations of targets, please see Figure 1. The microphone provides information about soil targets including grain size and surface properties (Martin et al., 2023).

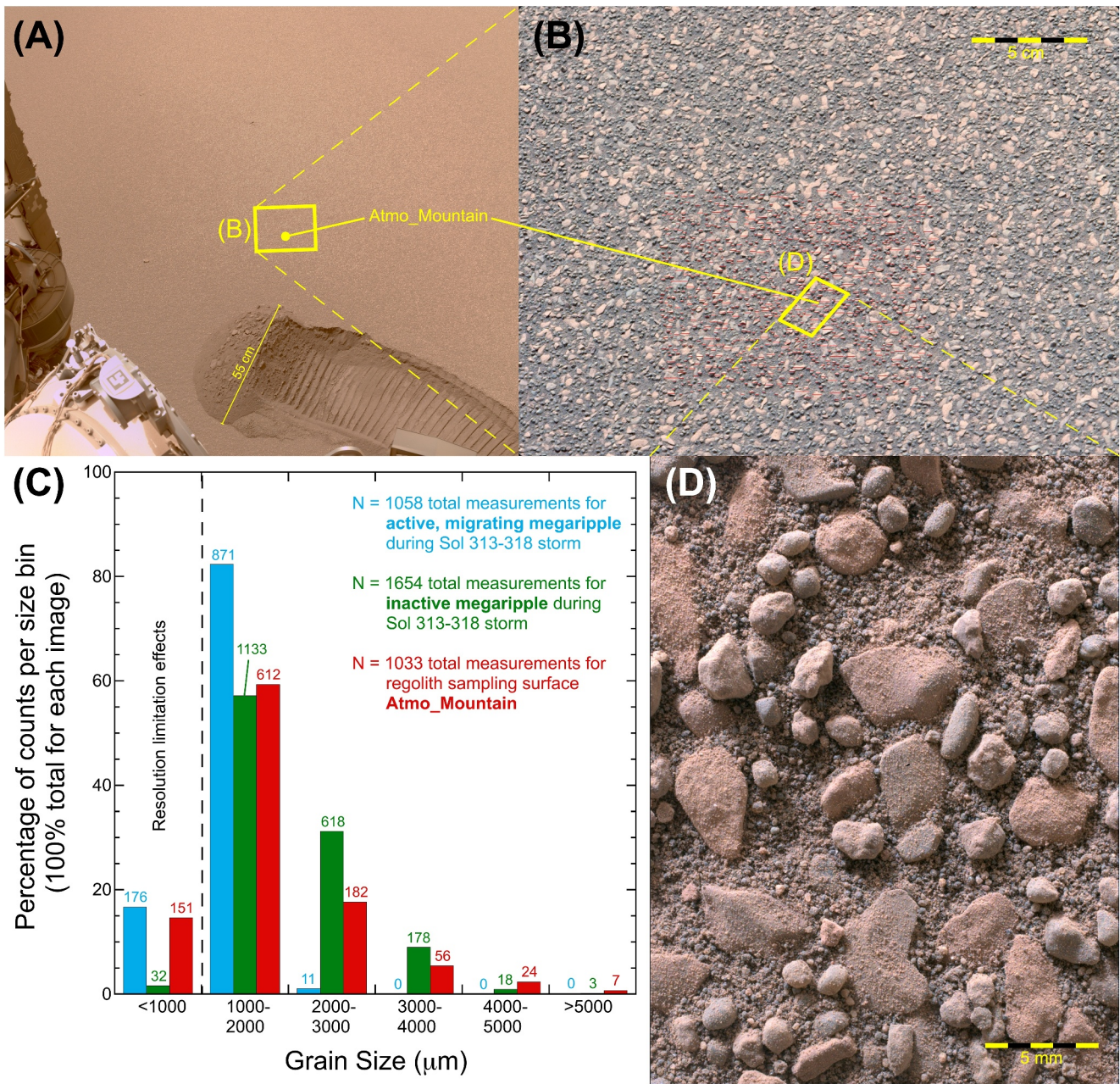


**Figure 11.** Grain size characteristics on the undisturbed stoss flank of the *Observation Mountain* megaripple, using the *Atmo Mountain* sampling target as representative. (a) Navcam view showing location of *Atmo Mountain* relative to the wheel trench and tailings pile (Sol 596, sequence ncam00709). (b) Color-stretched Mastcam-Z view of the *Atmo Mountain* area, with individual grain size measurement locations marked in red; grain size measurements are very fine scale and best observed by zooming into the image (Sol 594, sequence zcam03463). (c) Grain size-frequency measurements presented as percentage of grain counts per size bin, comparing *Atmo Mountain* (red) to active (blue) and inactive (green) megaripples observed with the same instrument at similar resolution earlier in the mission (Figure 7 for details). The regolith sampling surface is endowed with abundant grains  $>2$  mm, so resembles the inactive megaripple with surface grains observed to be stable during the Sol 313–318 regional storm. (d) Color-stretched WATSON view of *Atmo Mountain* before sampling,  $17.5 \mu\text{m}/\text{pixel}$ , showing diversity of grain sizes, shapes, and colors (Sol 598, sequence srlc00364 and srlc00071). This surface contrasts with dominantly much finer material in the near-subsurface (compare with Figure 5).

#### 2.4.1. SuperCam RMI

The SuperCam Remote Micro-Imager (RMI) uses a 2048-pixel square CMOS sensor outfitted with a Bayer filter for color imaging (Maurice et al., 2021). Its pixel angular resolution is 9 microradians, or  $\sim 20 \mu\text{m}$  at a distance of 2.0–2.3 m from SuperCam in the arm work area. However, the telescope optics are optimized for Laser Induced Breakdown Spectroscopy (LIBS), so are the limiting factor in overall resolution and allow identification of

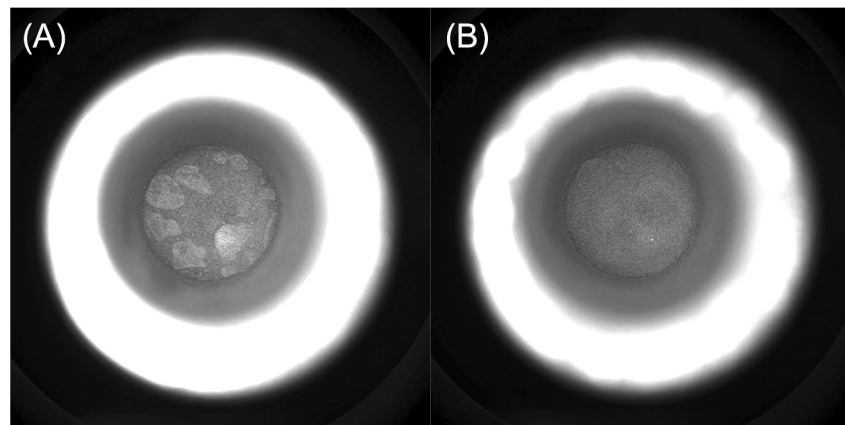


**Figure 12.** Cachecam (Maki, Gruel, et al., 2020) subframes showing the (a) *Atmo Mountain* and (b) *Crosswind Lake* regolith samples on-board the rover, before each was sealed (Sol 634 sequence cach00227, and Sol 639 sequence cach00227, respectively). These images (contrast-enhanced, and represented here in grayscale due to artificial illumination) represent the only images of the regolith that was actually sampled, and show only the top surface of each regolith sample volume. Each sample appears to be dominated by fine grains  $<150\ \mu\text{m}$ , as expected, but much coarser grains similar to those in Figure 11 D are visible at the top of *Atmo Mountain* and might also be visible at the top of *Crosswind Lake*, slightly protruding next to the wall at upper left.

mineral grains in color at sizes down to  $<200\ \mu\text{m}$  in front of the rover. RMI images are corrected for flat field and color balanced using on-board targets.

An image is taken prior to performing LIBS on the first point of the raster, and subsequently at other points along the LIBS raster, concluding with an image after the final LIBS on the last point. The images can be merged to create a mosaic showing the undisturbed surface prior to LIBS, using the earlier images for the immediate region of the spectral observation points. They can also be merged in such a way as to show the surface with all of the LIBS pits, using the later images for the immediate region of the points.

#### 2.4.2. Combined VISIR Measurements by SuperCam and Mastcam-Z

Visible and near-infrared spectral data were collected by both the Mastcam-Z and SuperCam instruments, with Mastcam-Z providing visible to near-infrared (VNIR) multispectral data through 12 narrowband filters covering

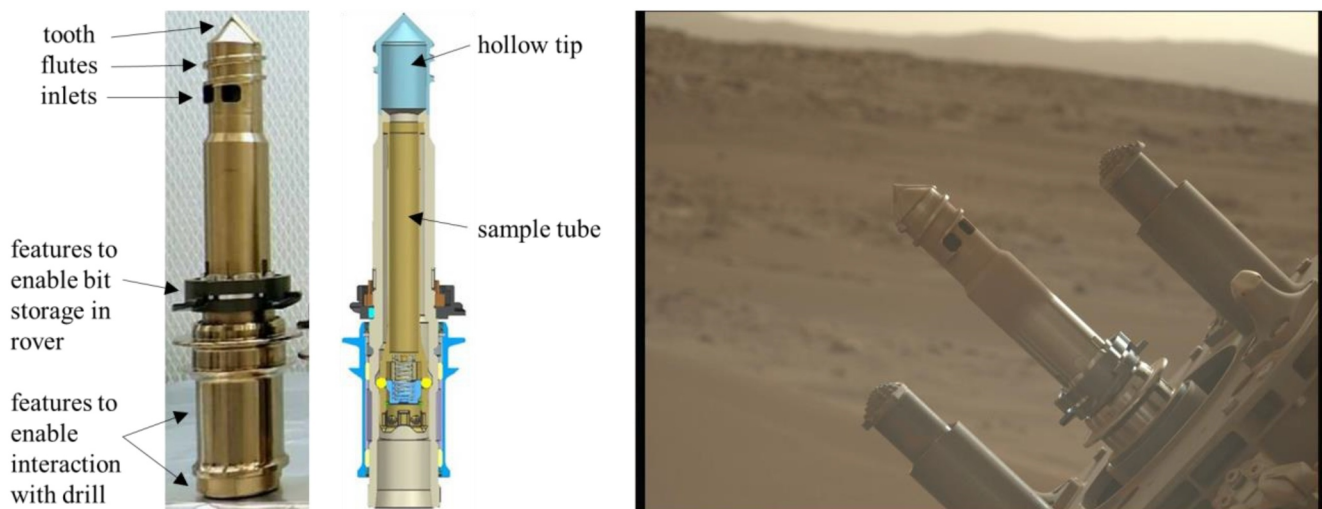


**Figure 13.** Left image is of the regolith bit before installation into the rover, with labels indicating the major sampling features. Middle image is of a cross section of the regolith bit, showing the hollow tip and inner sample tube. Right image is of the regolith sampling bit (in the center between the drill stabilizers) after collecting a sample on Mars (Mastcam-Z Camera image from Sol 634 (zcam05134)).

**Table 2**

*Measurements Associated With Regolith Sampling; Atmospheric and Environmental Measurements Described in Section 3.6*

Sol	STOP list measurement	Target Name/description	Sequence Ids
593	*Pre-bump <b>Mastcam-Z</b> Context Mosaic	<i>Observation Mtn</i> Megaripple	zcam08608
593	*Ripple scuff/trench mobility activity	<i>Observation Mtn</i> Megaripple	NA
593	Post-bump, post-trench creation <b>Mastcam-Z</b> Workspace Mosaic (arm partially occluding)	<i>Observation Mtn</i> Megaripple workspace	zcam07101
594	<b>Mastcam-Z</b> multispectral of undisturbed surface material	<i>Granite Peak</i> /undisturbed surface	zcam03463
594	<b>WATSON</b> target assessment	<i>Atmo Mountain</i> /undisturbed surface, <i>Crosswind Lake</i> /undisturbed surface, <i>Marmot Bay</i> /undisturbed surface, <i>Topographers Peak</i> /disturbed tailings <i>Fulton Falls</i> /disturbed trench wall	srlc00704 srlc01504 srlc02504
594	<b>SuperCam</b> LIBS VISIR RMI	<i>Granite Peak</i> /undisturbed surface	scam01594
596	<b>SuperCam</b> LIBS VISIR RMI	<i>Fulton Falls</i> /disturbed trench wall	scam01596
596	<b>Mastcam-Z</b> multispectral	<i>Fulton Falls</i> /disturbed trench wall	zcam03464
596	<b>Mastcam-Z</b> workspace mosaic reshoots (with arm out of the way)	<i>Observation Mtn</i> Megaripple workspace	zcam08610
598	<b>SHERLOC</b> ACI and 10 × 10 point Scan	<i>Topographers Peak</i> /disturbed tailings	srlc11420.0003a.survey_table_2_max
598	<b>PIXL</b> 5 mm × 5 mm map scan	<i>Topographers Peak</i> /disturbed tailings	pixl05598
599	<b>SuperCam</b> LIBS VISIR RMI	<i>Geographic Harbor</i> /disturbed tailings	scam01599
599	<b>Mastcam-Z</b> Multispectral	<i>Topographers Peak</i> and <i>Geographic Harbor</i> /disturbed tailings	zcam03465
600	<b>SuperCam</b> LIBS, VISIR, RMI	<i>Fulton Falls</i> /disturbed trench wall	scam01600
600	<b>SHERLOC</b> ACI and 10 × 10 point Scan	<i>Marmot Bay</i> /undisturbed surface	srlc11420.0003a.survey_table_2_max
600	<b>PIXL</b> map (3.5 mm × 7 mm) and grid (21 mm × 21 mm) scans	<i>Marmot Bay</i> /undisturbed surface	pixl05601 pixl05600
602	<b>SuperCam</b> LIBS VISIR RMI	<i>Funnel Creek</i> /disturbed trench floor	scam1602
602	<b>Mastcam-Z</b> Multispectral	<i>Funnel Creek</i> /disturbed trench floor	zcam03466
632	<b>Mastcam-Z</b> Workspace Mosaic (upon return to site)	<i>Observation Mtn</i> Megaripple workspace	zcam08632
633	<b>WATSON</b> 40 and 7 cm standoff	<i>Atmo Mountain</i> /undisturbed surface	srlc00746 srlc04004
634	<b>Sample Acquisition</b>	<i>Atmo Mountain</i>	NA
638	<b>WATSON</b> 40 and 7 cm standoff	<i>Crosswind Lake</i>	srlc00701 srlc04001
639	<b>Sample Acquisition</b>	<i>Crosswind Lake</i>	NA
641	<b>Mastcam-Z</b> post-sampling multispectral	<i>Crosswind Lake</i> /disturbed sample tailings	zcam03499
641	<b>SuperCam</b> LIBS VISIR RMI post-sampling	<i>Atmo Mountain</i> /disturbed sample tailings <i>Crosswind Lake</i> /disturbed sample tailings	scam01641 scam02641

Note. NA No sequence IDs for these activities. \* indicates activities that occurred before the final positioning for all subsequent imaging. The bold values indicate the instrument and sample acquisition activities.

442–1,022 nm, and SuperCam spectrometers covering 0.39–0.48 μm (ultra-violet spectrometer, UV), 0.55–0.86 μm (visible spectrometer, VIS) and 1.3–2.6 μm (Infrared Spectrometer, IRS). The SuperCam range enables the identification of different minerals, including mafic igneous minerals (olivine, pyroxene) and secondary phases such as phyllosilicates, sulfates, or carbonates. Mastcam-Z multispectral data enable the identification of absorption bands of minerals of interest not centered in the SuperCam range (e.g., the 0.86 μm hematite band, or

one of the pyroxene bands near 1  $\mu\text{m}$ ). Hence, combining the two data sets allows for a better discrimination of the different minerals present in a target, and this combination is presented below.

Combined Mastcam-Z and SuperCam reflectance spectra were produced following the method in Mandon et al. (2024): for targets measured by the two instruments, data were calibrated to relative reflectance using the processing described in Merusi et al. (2022), Mandon et al. (2023), and Royer et al. (2023). The SuperCam spectra (1–10 point spectra for each measurement) were averaged, then compared with average Mastcam-Z spectra extracted from the corresponding region of interest (ROI). In the combined spectra generated in this work, the Mastcam-Z spectra were offset to fit the reflectance measured by SuperCam at 754 nm (L2 filter). For regolith targets, SuperCam reflectance spectra were acquired before LIBS bursts to avoid shadowing related to the LIBS pits. In some observations, the Mastcam-Z observation was performed after SuperCam (and hence LIBS), so the original surface measured by the SuperCam VISIR spectrometers wasn't observable anymore. In that case, we assumed the regolith targets were homogeneous and used a Mastcam-Z ROI slightly shifted from the LIBS pits locations.

#### 2.4.3. Laser Induced Breakdown Spectroscopy (LIBS) Analyses

Major and trace element quantification was performed by LIBS measurements (Maurice et al., 2021; Wiens, Maurice, Robinson, et al., 2021). Measurements of LIBS usually consist of rasters of 5–10 observation points on a target using a focused laser beam of 100–450  $\mu\text{m}$  in diameter at 1.5–7 m distance (Maurice et al., 2021). In each point, 30 to 50 laser pulses (“shots”) are generally taken. Analysis of either the individual “single shot” spectra can be performed, or averages of all spectra for the point can be analyzed for improved statistics (generally excluding the top five shots to remove the impacts of dust). The SuperCam targets used in this paper are listed in Table 2, and SuperCam data are available on the PDS (Wiens, Maurice, Deen, et al., 2021).

To best document the in situ regolith for future analyses of the returned sample on Earth, the LIBS measurements were analyzed by (a) examining the changes in the hydrogen score (Forni et al., 2013) as a function of shot to identify potential differences with depth (b) Principal Component Analysis (PCA) of the shot-to-shot LIBS major element oxide composition (MOC) data and the hydrogen, chlorine, and sulfur scores were examined for the fine-grained soils from *Observation Mountain* (excluding the top 5 points to remove the effect of dust), and (c) both the averages of the spectra (minus the top 5 shots) and the first shots as indicators of the composition of airfall dust (Lasue et al., 2018, 2023) were compared to other measurements of soil and dust in the discussion.

#### 2.4.4. MEDA Measurements

MEDA nominal measurements consist of 65 min long blocks starting at odd local mean solar time (LMST) hours on odd Sols, and even LMST hours on even Sols (Martínez et al., 2023). However, MEDA measurements on sampling Sols 634 and 639 were restricted to the first 15 min of each hour because of power constraints during sampling Sols, although three additional 15-min-long floating sessions were scheduled during sample sealing and over the sunrise before and after sampling, with the sunrise measurements (a time of minimum temperature hence peak relative humidity, RH) used to calculate the near-surface water vapor abundance most accurately.

#### 2.4.5. SHERLOC Measurements

Scanning Habitable Environments with Raman and Luminescence for Organics and Chemicals (SHERLOC) has three subsystems: WATSON, SHERLOC ACI, and the SHERLOC spectrometer. SHERLOC ACI provides 10.1  $\mu\text{m}/\text{pixel}$  grayscale images that are co-boresighted with the spectrometer, and WATSON full color images with variable standoffs and can go down to  $\sim 13 \mu\text{m}/\text{pixel}$  (Bhartia et al., 2021). SHERLOC scans were performed on *Topographers Peak* (wheel trench tailings pile dominated by subsurface material) and *Marmot Bay* (undisturbed surface near sampling locations *Atmo Mountain* and *Crosswind Lake*). The scans utilized for this study were  $7 \times 7 \text{ mm}$  with  $10 \times 10$  analysis points ( $\sim 110$  micron diameter annuli) and 780 micron spacing between points. For *Topographers Peak*, measured on Sol 598, the Raman spectrum is the trimmed mean (2%) of all 100 points in the scan. The fluorescence spectra are mean averages each representing a selected ROI for the three distinct signals. The cosmic rays were partially removed and data were laser normalized in Loupe (Uckert, 2022), the mean calculated in Excel (Microsoft), and then the spectra were plotted in Igor Pro 9 (Wavemetrics). Similarly, for the *Marmot Bay* spectra taken on Sol 600, the Raman average spectrum included all 100 points in

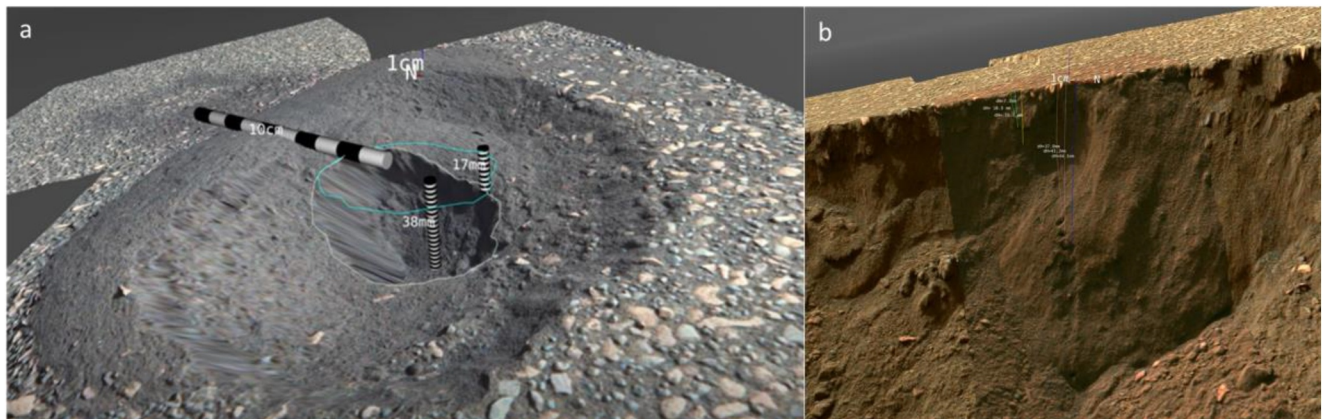


**Figure 14.** Mastcam-Z stereo imaging 3D product of the *Atmo Mountain* sample hole indicates that (a) the measured depth of the sample hole is 3.8 cm, which, since some material may have fallen into the hole during sampling, represents a minimum depth, and is reasonably consistent with the measurements of the depth of sampling obtained in the laboratory experiments at JPL (4–6 cm). The 17 mm scale bar indicates the depth of the second rim compared to the undisturbed surface, the white line is the outline of the sample hole region, and the blue line is the projection of this outline up to the undisturbed surface (Sol 594, not shown here). (b) Depths from the original megaripple surface of Laser Induced Breakdown Spectroscopy (LIBS) measurements are indicated, showing that the LIBS measurements acquired on Sol 600, and the top ~6 LIBS measurements acquired on Sol 596, measure material likely from a similar depth range as that collected in the sample tubes. The Mastcam-Z image and spectral data are available in the Planetary Data System (Bell et al., 2021), and the 3D processing is described in Paar et al. (2023).

the scan, processed and plotted as above. The fluorescence spectra are mean averages each representing a selected ROI for the two distinct signals. The same processing and plotting procedure was used as above.

### 3. Results of Instrument Observations

Results of instrument analyses associated with regolith sample collection include physical measurements with stereo Mastcam-Z images of the depth of one of the sampling holes and the LIBS measurements on the *Fulton Falls* trench wall (Section 3.1), the grain size and sedimentary textures analyzed using WATSON data (Section 3.2), and the evidence for dust analyzed by the SuperCam RMI camera (Section 3.3). Chemical analyses are then presented, including VISIR analyses from both Mastcam-Z and SuperCam (Section 3.4), the SuperCam LIBS analyses (Section 3.5), followed by the MEDA relative humidity and temperature analyses (Section 3.6), the SHERLOC Raman and fluorescence analyses (Section 3.7), and the PIXL geochemical analyses (Section 3.8).

#### 3.1. Mastcam-Z 3-Dimensional Measurements

Mastcam-Z is a pair of zoomable (26–110 mm focal lengths), focusable, stereoscopic cameras located atop the rover mast (Bell et al., 2021; Hayes et al., 2021; Kinch et al., 2020). Three-dimensional analysis of the soil disturbed during sampling was performed using color Mastcam-Z images using the techniques of Paar et al. (2023). Results of the 3D imaging yield a minimum depth of the sample hole of 3.8 cm (which includes effects from the collapse of the surface around the hole, and tailings partially filling it), and the depths from the original megaripple surface of the LIBS measurements on the *Fulton Falls* trench wall “soil profile” (Figure 14). Additional results of the 3D modeling showing the unsampled surface of the bedform, followed by sampling, are included in Supporting Information S1.

#### 3.2. WATSON Grain Size and Sedimentary Textures

##### 3.2.1. Undisturbed Surface Analyses

An initial grain size analysis of the undisturbed surface (Farley & Stack, 2023b; see also Figure 11) reported a size range from ~80  $\mu\text{m}$  (very fine sand) to ~5.5 mm (pebble; Wentworth, 1922), with the sample dominated by coarse sand. In a separate analysis, the roundness and sphericity of the coarse particles was measured. Roundness is an estimate of the smoothness of the grain surface and is described as well-rounded, rounded, subrounded, subangular, angular, or very angular (Powers, 1953). Sphericity, described from high sphericity to low sphericity, is an estimate of how close the grain is to a sphere in shape (Powers, 1953). The roundness and sphericity analysis

**Table 3**  
*Description of Roundness and Sphericity of Grains at Crosswind Lake and Atmo Mountain*

	Crosswind Lake	Atmo Mountain
High sphericity (%)	59	59
Low sphericity (%)	41	41
Very angular (%)	15	1559
Angular (%)	7	17
Sub-angular (%)	19	23
Sub-rounded (%)	22	20
Rounded (%)	25	14
Well rounded (%)	13	13

utilized the highest resolution WATSON images with resolutions of  $\sim 18 \mu\text{m}$ /pixel (see Figures S6 and S7 in Supporting Information S1). Within these images, 106 grains were considered for *Atmo Mountain* and 154 for *Crosswind Lake*. Grain roundness ranged from well-rounded to very angular (Table 3). The percentage of grains with high sphericity is 59% for both *Atmo Mountain* and *Crosswind Lake* (Table 3). Because these grain textures were described with 2D images and the 3D views of the grains were not possible, there is likely a small amount of error in the determinations of sphericity and roundness.

These results may be interpreted as supporting the hypothesis that these grains were deposited by a moderate amount of energy in a relatively short period and from a low to moderate distance from the source region. However, this is based on several assumptions: (a) that all grains were deposited at the same time, (b) that all grains underwent the same previous transport processes; and

(c) that all grains had composition similar enough to give them comparable resistance or vulnerability to physical and chemical weathering. Based on the above, one potential depositional environment is a mid-fan deposit perhaps closer to the mid-fan to distal fan transition given the relatively low amount of gravel-sized grains (Blair & McPherson, 1994). However, additional evidence such as sedimentary structures, 3D geometry of the deposit, and syndepositional diagenetic features are required to evaluate this hypothesis.

The larger grains in both *Atmo Mountain* and *Crosswind Lake* appear to have a pink-reddish color while the smaller grains appear to be white-gray colored. Additionally, the larger pink-reddish grains appear to be more embedded than the other coarse grains, which appear to simply be lying on the surface. This could suggest two separate periods of deposition with the pink-reddish color grains being deposited first followed by the white-gray colored grains at a later time.

### 3.2.2. Disturbed Surface Analyses

Grain size measurements were performed on ACI images of *Topographers Peak*, the tailings pile target composed mostly of subsurface material. Due to the natural topography of the tailings pile surface, ACI images from 31 focal distances were combined into a single merged z-stack image that was also flatfielded. For grain size determinations, a grid of  $20 \times 20$  pixel squares (each pixel is  $10.1 \mu\text{m}$ ) with a random origin was overlaid onto the flatfield image using ImageJ Fiji. Discernible grains at grid crossings were outlined by polygon for measurement. This was done twice (i.e., two random origin grids of  $20 \times 20$  pixel squares were placed). From the resulting data, the major axis of each grain, in both  $\mu\text{m}$  and  $\Phi$ , was designated as the grain size and the combined data were used to determine an overall estimated grain size population of the disturbed surface of *Topographers Peak*.

Determining grain sizes from two-dimensional image analysis presents numerous challenges. Grains are often partially occluded by other finer grains. Much of the natural sample is in shadow or is natural void space. Further, single grains can appear as multiple grains due to dust or contrast effects from rough surfaces. Multiple grains can appear to be single grains because of lack of contrast. Therefore, only grains which could be clearly discerned (i.e., not occluded by other grains, complicated by lighting issues, or otherwise obscured) were measured. To assist with this, the individual ACI slices used to make the flatfield image were referred to, as well as a WTSN color image. The WTSN color image is of lower resolution, however, the color data could sometimes help distinguish between grains of similar grayscale contrast. Final measurements, however, were done on the ACI merged image.

The mean grain size estimate here was  $\sim 125 \mu\text{m}$  ( $+3.0 \Phi$ ) with a median of  $\sim 95 \mu\text{m}$  ( $+3.4 \Phi$ ), a unimodal distribution (Figure 15) and a standard deviation of  $\Phi$  of 0.7. This included measured grains  $>1 \text{ mm}$ . The standard deviation places the sorting on the boundary of moderately to moderately well sorted (Folk & Ward, 1957). The grain size result is slightly finer than measurements from active ripple field targets ( $107\text{--}414 \mu\text{m}$  medians) and linear dunes ( $110\text{--}129 \mu\text{m}$  medians) measured at Gale crater using similar methods (Weitz et al., 2018). The finer results for *Topographer's Peak* suggest relatively longer transport distances for the aeolian materials at this location in Jezero compared to Gale. However, it is worth noting that the ACI resolution ( $\sim 10 \mu\text{m}/\text{pixel}$ ) is finer than the MAHLI image resolution ( $16\text{--}28 \mu\text{m}/\text{pixel}$ ) reported by Weitz et al. (2018) in the Gale crater study, and this could increase the counts of finer grains for the ACI image. In addition, given the

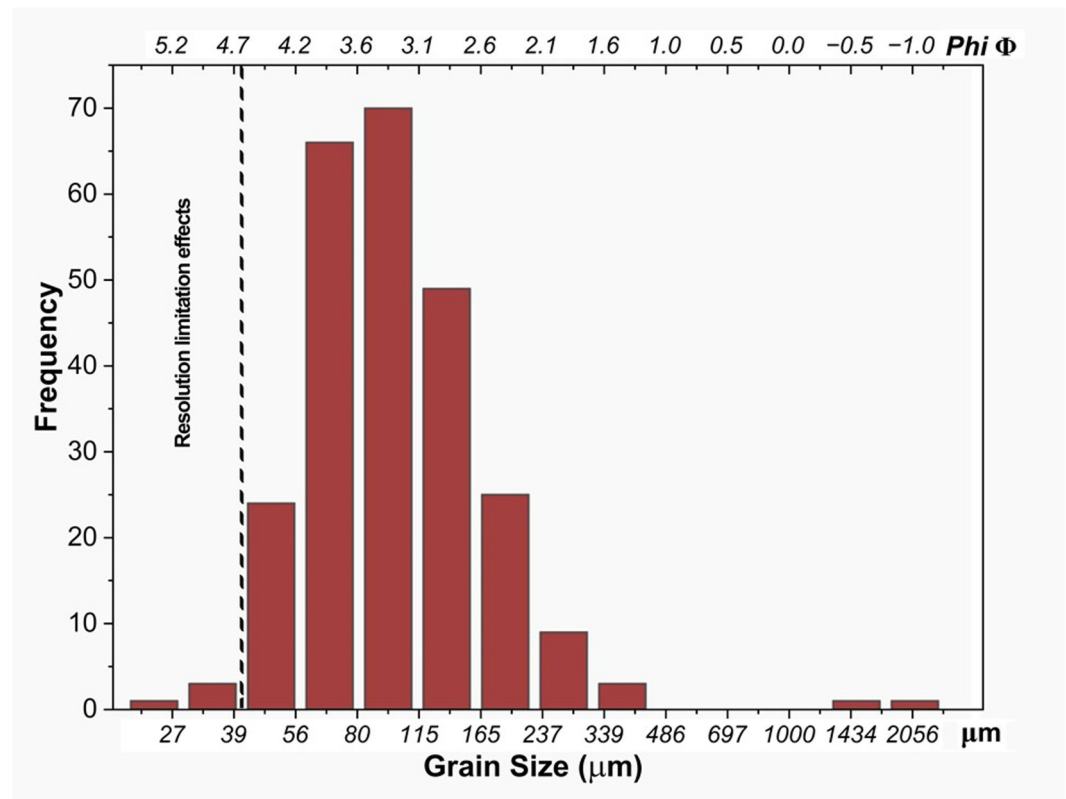


**Figure 15.** Grain size distribution of the disturbed surface of *Topographers Peak*. Mean measured grain size was  $\sim 125 \mu\text{m}$  ( $\Phi = 3.0$ ) inclusive, or  $\sim 110 \mu\text{m}$  ( $\Phi = 3.2$ ) for  $< 1 \text{ mm}$  grains. Dashed line indicates the likely resolution limit where uncertainty in small grain sizes begins to increase substantially. See Table S8 in Supporting Information S1 for the bin values in this figure.

imaging difficulties noted above, a particle size analysis on the returned sample, possibly by a more traditional mass fraction method, will provide a more definitive determination.

### 3.3. SuperCam RMI

SuperCam's RMI provides visual contexts to complement the elemental composition and mineral detail provided by its spectral techniques. An image showing changes between the RMI images taken prior to performing LIBS on *Granite Peak*, and after taking the LIBS measurements on *Granite Peak* in the red channel shows a dark path across the LIBS points, consistent with the removal of likely Fe-rich dust (Figure 16). This Fe-rich dust is therefore likely present in the regolith sample that was collected (*Granite Peak* was located between the regolith sampling sites of *Atmo Mountain* and *Crosswind Lake*, and served as a representative of these two targets to spare them from any effects of Supercam LIBS or PIXL activities.)

### 3.4. VISIR Measurements of Grains in the Sampling Area and Comparison With Rock Measurements

Mastcam-Z multispectral imaging of the natural surface of the *Observation Mountain* megaripple (target *Granite Peak*) shows a diversity of coarser clasts armoring the megaripple, which has a finer-grained interior. Enhanced color and decorrelation stretch images show larger (3–5 mm), angular light-toned fragments, angular dark-toned fragments, and smaller (1–2 mm), rounded dark-toned grains (Figure 17). Spectra of the light-toned fragments show steep red edges and absorption bands at 528 and 866 nm, consistent with ferric iron. They are similar to nearby *Knife Creek* outcrop spectra, indicating a possible proximal source (Figure 17). Figure 18 shows that of all targets sampled on the *Observation Mountain* megaripple, these light-toned angular clasts exhibited the strongest 528 nm band depths, and most pronounced 866 nm band depths (shown by the 866/978 nm ratio) and were likely therefore the most oxidized component collected in the regolith sample.



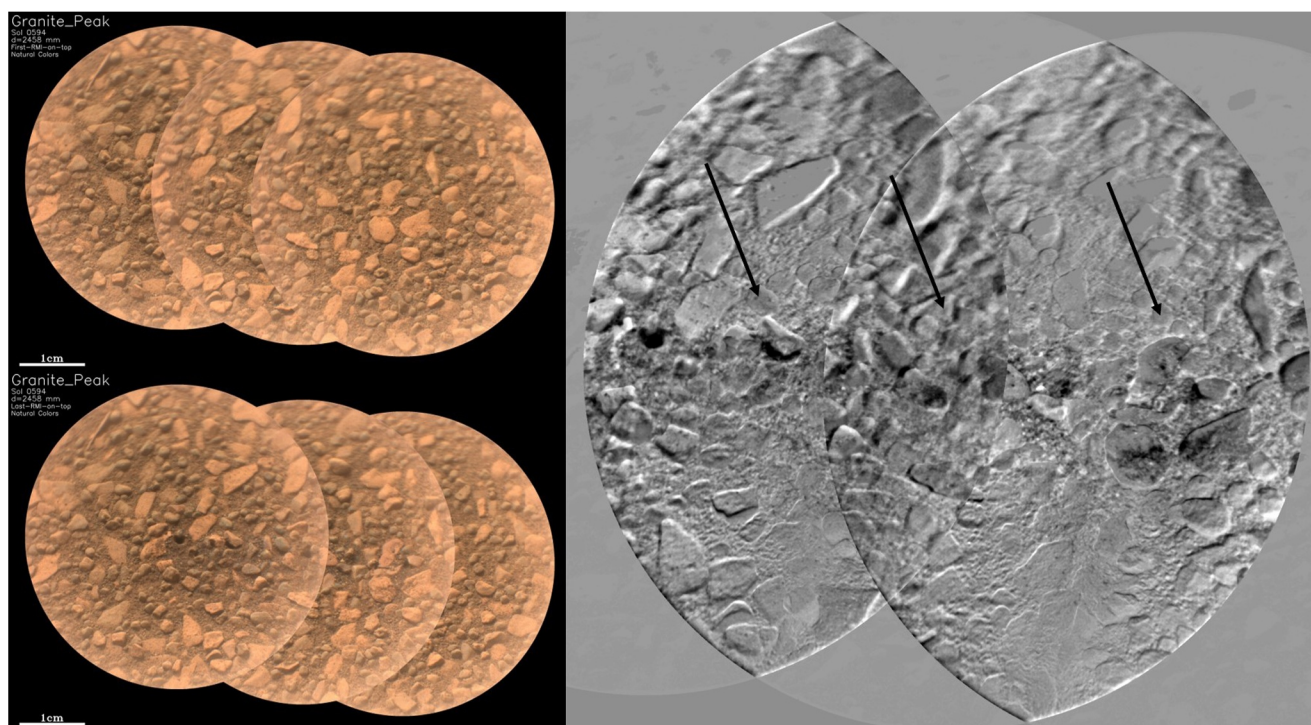


**Figure 16.** Remote Micro-Imager (RMI) mosaics of *Granite Peak* (sol 594; ASCAM\_SOL0594\_scam01594\_MOS\_FR08\_AFT\_RGB\_\_\_\_Granite\_Peak\_\_\_\_\_P01) before the Laser Induced Breakdown Spectroscopy (LIBS) activity (top left), and after the LIBS activity (bottom left). Right pane shows the difference between the two RMI mosaics of *Granite Peak* in the red channel. The dark path across the difference RMI image indicated with arrows is consistent with the removal of airfall dust, which is likely Fe-rich, and therefore well-visualized in the red channel.

Neither population of dark-toned clasts has spectral features indicative of olivine in the Mastcam-Z data, despite the olivine-dominated nature of the nearby Séítah region and the olivine-bearing coarse regolith observed throughout the Jezero Crater Floor Campaign (Vaughan et al., 2023). This could be explained by either (a) no olivine being present in the coarse material armoring the megaripple; or (b) the olivine being sufficiently altered or mixed with other phases to mask its signature (e.g., through stronger absorbers such as ferric iron-bearing phases or orthopyroxene).

Given data collected on the chemistry of these coarse clasts by other instruments presented in this paper, the second option is well supported. SuperCam IRS and PIXL (Section 3.8) measurements indicate the presence of olivine as either a component of a mixture (SuperCam), or as individual altered olivine grains (PIXL).

The fine-grained regolith component exhibited lower albedo than the coarser grains discussed above. Figure 18 shows that all fine-grained regolith targets within the trench and sample tailings exhibited intermediate ferric spectral features compared to the light-toned coarser fragments (more ferric) and the dark-toned coarser clasts (less ferric). As the point colors (shaded by 866/978 nm ratio) in Figure 18 illustrate, there was some variability in the presence of an 866 nm absorption. For example, the natural surface (*Granite Peak*) fine-grained regolith exhibited an 866 nm absorption (possibly attributable to airfall dust), but most disturbed fine-grained regolith targets (e.g., *Fultons Falls*, *Topographers Peak*, and the *Crosswind Lake* sample tailings) exhibited band minima between 900 and 1,000 nm, more consistent with a low-calcium pyroxene (Figure 17). *Topographers Peak* and *Fulton Falls* were consistent with the average fine-grained regolith spectrum from the Jezero Crater Floor Campaign (Vaughan et al., 2023), suggesting that this material has a greater areal extent and could represent a regional, or even global, component.

Mastcam-Z and SuperCam combined spectra of the disturbed regolith targets and *Crosswind Lake* tailings show a broad  $\sim 0.8\text{--}1.7\ \mu\text{m}$   $\text{Fe}^{2+}$  absorption band centered near  $0.9\text{--}1\ \mu\text{m}$ , as well as another  $\text{Fe}^{2+}$  broad and shallow  $0.7\text{--}2.4\ \mu\text{m}$  absorption centered near  $2\ \mu\text{m}$  (Figure 19). This is similar to the spectra of fine soils measured along the rover traverse (Hausrath et al., 2023; Mandon et al., 2023; Vaughan et al., 2023) and consistent with the presence

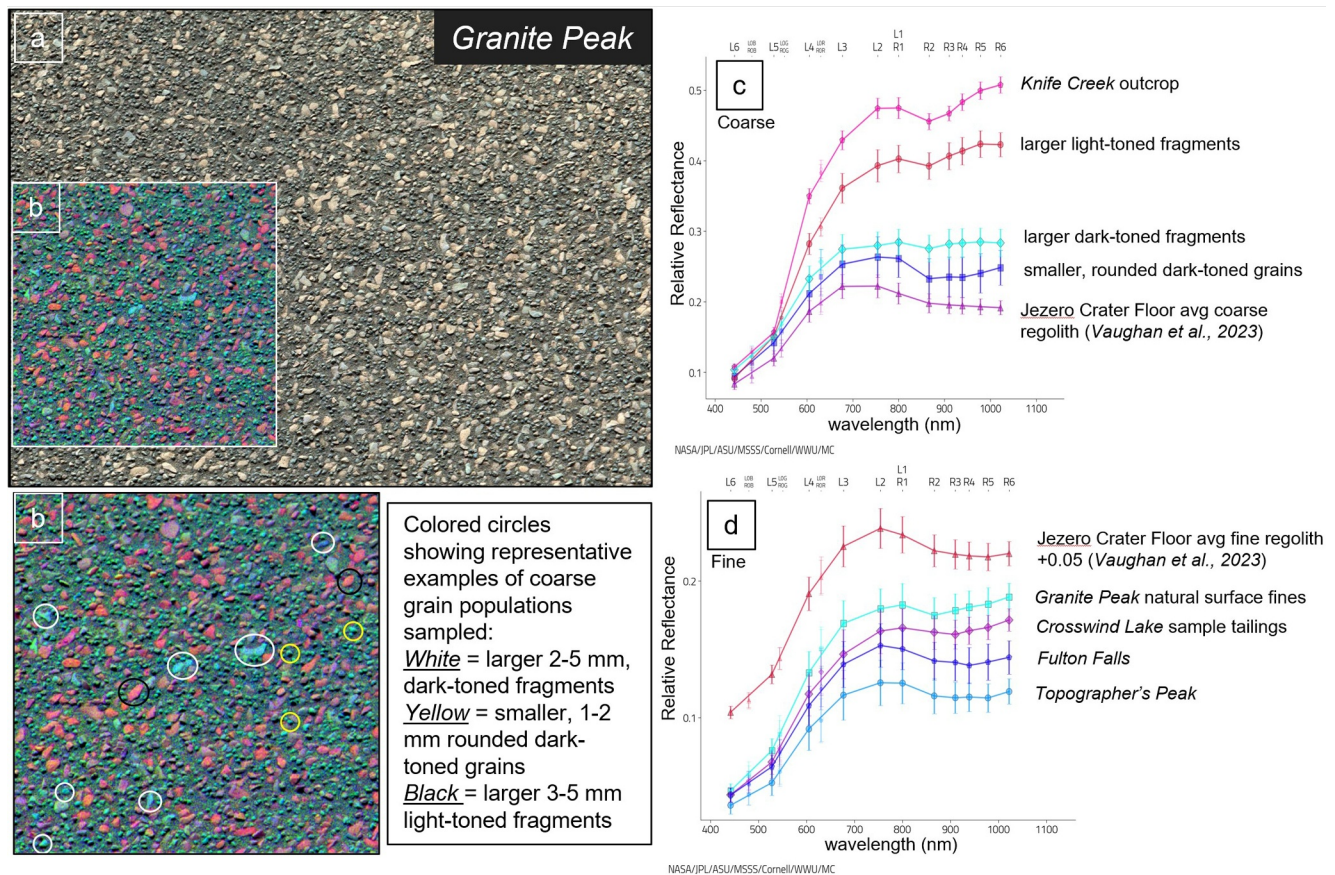


**Figure 17.** Mastcam-Z Multispectral Data. (a) Left-eye Bayer (L0 filter) enhanced color image of the undisturbed surface of the *Observation Mountain* megarripple at target *Granite Peak* taken at 110 mm focal length acquired on Sol 594 (zcam03463). (b) Decorrelation stretch image using wavelengths 754 nm (L2 filter), 528 nm (L5 filter), and 442 nm (L6 filter) to illustrate color diversity of material. (c) Representative spectra of coarse material armoring the megarripple as identified in (b) and compared to nearby outcrop *Knife Creek* and the average coarse regolith from the Jezero Crater Floor Campaign, (d) the fine-grained regolith of both natural and disturbed targets compared to the fine-grained regolith of the Jezero Crater Floor Campaign (offset shown in legend).

of pyroxene. Because the  $\sim 1 \mu\text{m}$  absorption is significantly deeper than the  $\sim 2 \mu\text{m}$ , a mixture with olivine is likely. These regolith targets also exhibit weak absorption features related to hydrated minerals: the  $1.93 \mu\text{m}$  water absorption is observed at 5% max. relative to the continuum (Figures 19 and 20), and the phyllosilicate and carbonate bands in the  $2.3\text{--}2.5 \mu\text{m}$  range are observed near noise levels (Figure 19). This is also in agreement with previous observations of fine soils having very low content of secondary minerals compared to the surrounding rocks (Hausrath et al., 2023; Mandon et al., 2023).

Undisturbed regolith (*Granite Peak* target) shows different spectral features compared to disturbed regolith: a band centered near  $0.86 \mu\text{m}$  (instead of  $>0.9 \mu\text{m}$ ) and indicative of hematite, as well as a stronger  $0.54 \mu\text{m}$  band depth (Figures 19 and 20) indicative of more ferric materials. Additionally, the undisturbed regolith spectra exhibit clear absorptions at  $1.93$ ,  $2.31$ , and  $2.39 \mu\text{m}$  (and perhaps  $2.53 \mu\text{m}$ ; Figure 19), in agreement with the presence of Fe/Mg-phyllosilicates (and possibly weak content of carbonates). These absorption bands, along with the  $0.86 \mu\text{m}$  absorption are deeper in the redder lighter-toned pebbles, and observed in the local bedrock (target *Knife Creek*; Figure 19). This shows that the hematite and phyllosilicates are present in the redder pebbles at the surface (as opposed to the fine fraction of the soils), and that these pebbles could have been sourced locally from the *Devil's Tanyard/Knife Creek* member bedrock.

SuperCam VISIR raster locations sampled light-toned and dark-toned grains on the undisturbed regolith target *Granite Peak* (Figure 21). Figure 20 shows the spectral parameters calculated for *Granite Peak* compared to the disturbed soil targets and the nearby outcrop *Knife Creek*. In Figure 20, *Knife Creek* exhibited the strongest

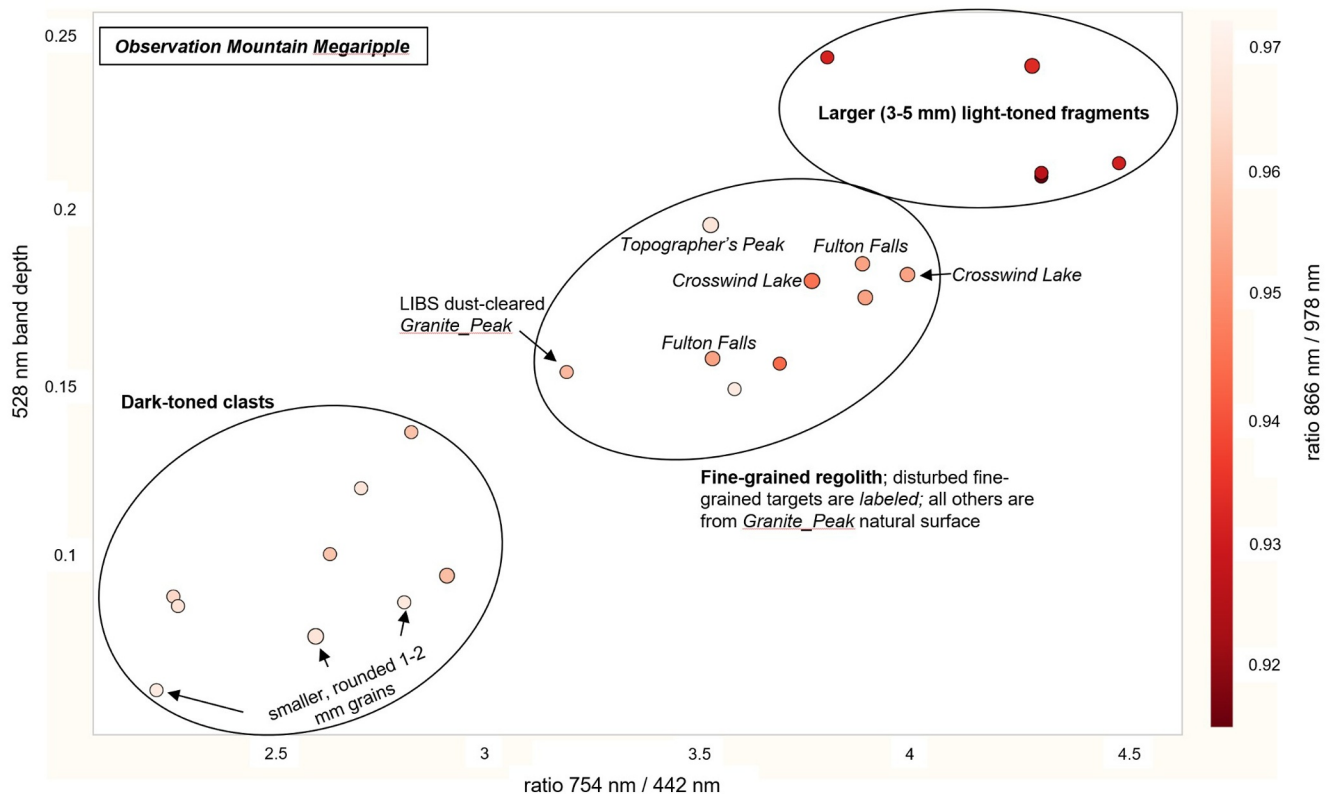


**Figure 18.** Mastcam-Z spectral parameter plot. All circles represent a spectrum from a unique region of interest collected in the *Observation Mountain* workspace. The parameters identified on each axis are representative of ferric iron spectral features such that the most ferric material is located in the upper right portion of the plot and redder circles.

545 nm band depths, indicative of ferric-bearing materials. On *Granite Peak*, light-toned grains sampled at locations 2, 4, and 6 exhibited high 670/440 nm ratios and strong 545 nm band depths that trended toward *Knife Creek's* values. Darker-toned grains sampled at locations 7 and 8 exhibited the weakest 545 nm band depths and highest 600/700 nm ratios, indicative of less ferric materials. Locations 3 and 9 exhibited the most elevated 1,930 nm hydration bands among the soil targets, but slightly different 1,350–1,800 nm slopes. This could be attributable to minor variations in alteration among the ferrous components in darker-toned grains and/or fine-grained regolith. Disturbed soil spectral parameters tended to cluster with similar values, although the *Atmo Mountain* and *Crosswind Lake* sample tailings and *Funnel Creek* rover track exhibited the weakest 670/440 nm and strongest 750/840 nm values, indicative of less ferric (or less dusty) materials.

Spectral modeling of the SuperCam IRS data was performed using non-linear unmixing (see Poulet et al. (2009) for the methodology). Application of this spectral modeling shows that spectra of the fine-grained regolith are best fit by a mixture of pyroxenes, olivine and plagioclase. A very tiny amount of hydrated minerals (smectites being a potential candidate) is required for some spectra to reproduce the very weak 1.9  $\mu\text{m}$  band. This basaltic composition is consistent with the LIBS observations (See Section 3.5). For the undisturbed regolith, olivine, pyroxene, plagioclase and a more substantial amount of alteration products including serpentine, Fe-smectite, and Mg-carbonate is required to reproduce both the hydration band (1.4 and 1.9  $\mu\text{m}$ ) and the 2.3  $\mu\text{m}$  signatures (Figure 22) well. The alteration phases serpentine, smectite, and carbonate are quite common in the Fan C sediments especially in *Amalik* rocks, which suggests locally derived contributions (Dehouck et al., 2023; Hurowitz et al., 2023; Royer et al., 2023).

### 3.5. Laser Induced Breakdown Spectroscopy (LIBS) Analyses

Previous work has demonstrated that the hydrogen score of the soil surface is generally higher than in the deepest shots, and that this increased near-surface hydrogen signal may be related to the formation of soil crusts (Hausrath et al., 2023). Although the soil crust will not be preserved intact in the sample tube, its components will be present.

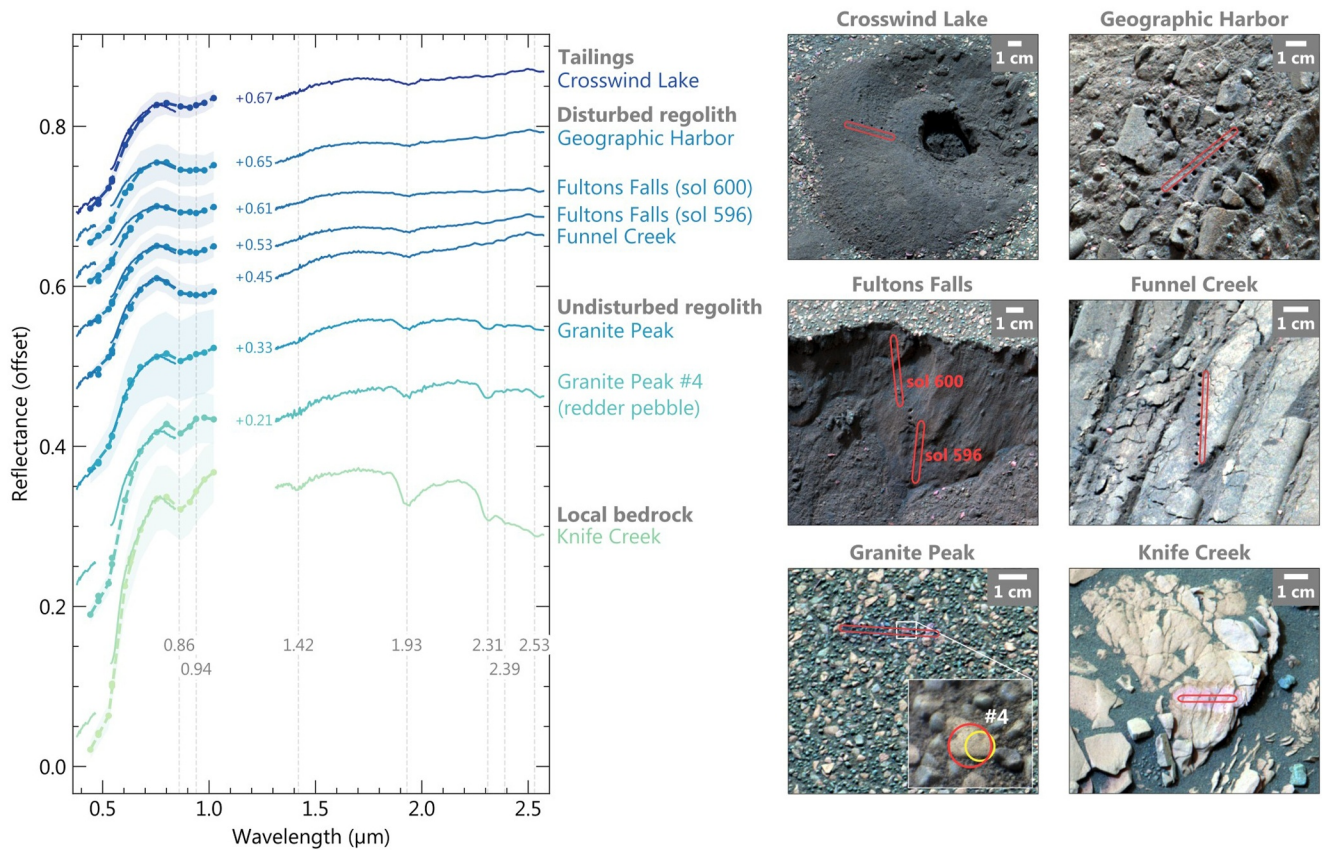


**Figure 19.** Combined Mastcam-Z and SuperCam spectra, along with corresponding areas of spectral measurement over Mastcam-Z enhanced colors images (R: L2 filter (754 nm), G: L5 filter (528 nm), b: L6 filter (442 nm)). SuperCam raster points averaged and Mastcam-Z regions of interest used to produce the spectra are shown in red. *Granite Peak* inset is a SuperCam Remote Micro-Imager image, with the yellow and red circles indicating the locations of the field of view accounting for 68% of signal measured by the UV + VIS and IRS SuperCam spectrometers, respectively.

Therefore, in order to examine the soil crust present on *Observation Mountain* (Figure 10) that will be in the material returned to Earth, we similarly compared the top 6 to 10 shots (similar to previous work, the top 5 shots were removed to avoid the effects of loose dust) with the deepest 10 shots. The change in H scores from shots 6–10 to the bottom 10 shots shows that most fine points (39 out of 55) show a statistically significant difference, which may indicate that the LIBS beam is penetrating through a hydrated crust that is thinner due to the decreased time it has had to form since disturbance (Figure 23).

PCA of the shot-to-shot data from the fine-grained materials of *Observation Mountain* shows a correlation between S, H, Cl, and K<sub>2</sub>O (Figure 24). This is similar to what has previously been observed for fine-grained material along the crater floor (Hausrath et al., 2023), suggesting the presence of hydrated salts in these materials.

### 3.6. MEDA

Of particular relevance for the regolith samples were MEDA's measurements of ground temperature and relative humidity described in Section 2.4.4. Figure 25 (top) shows the field of view of MEDA's ground temperature sensor (green shaded area) and the location of the regolith samples (white arrows). While the sampling locations were not within MEDA's field of view, measurements of ground temperature (Figure 25, bottom) should be representative of both samples given the similarity of the terrain. The ground temperature was ~255 K when sampling-related activities started (~15:53 LMST), which lasted for about 43 min on both Sols.

Figure 26 shows measurements of ground temperature (T<sub>g</sub>) as a function of RH with respect to ice at the ground (RH<sub>g</sub>) and LMST (color bar) for the Sol 593–641 period, when the rover was parked. We estimated RH<sub>g</sub> by assuming that the water vapor content is constant in the first 1.4 m above the ground using Equation 1. Therefore,

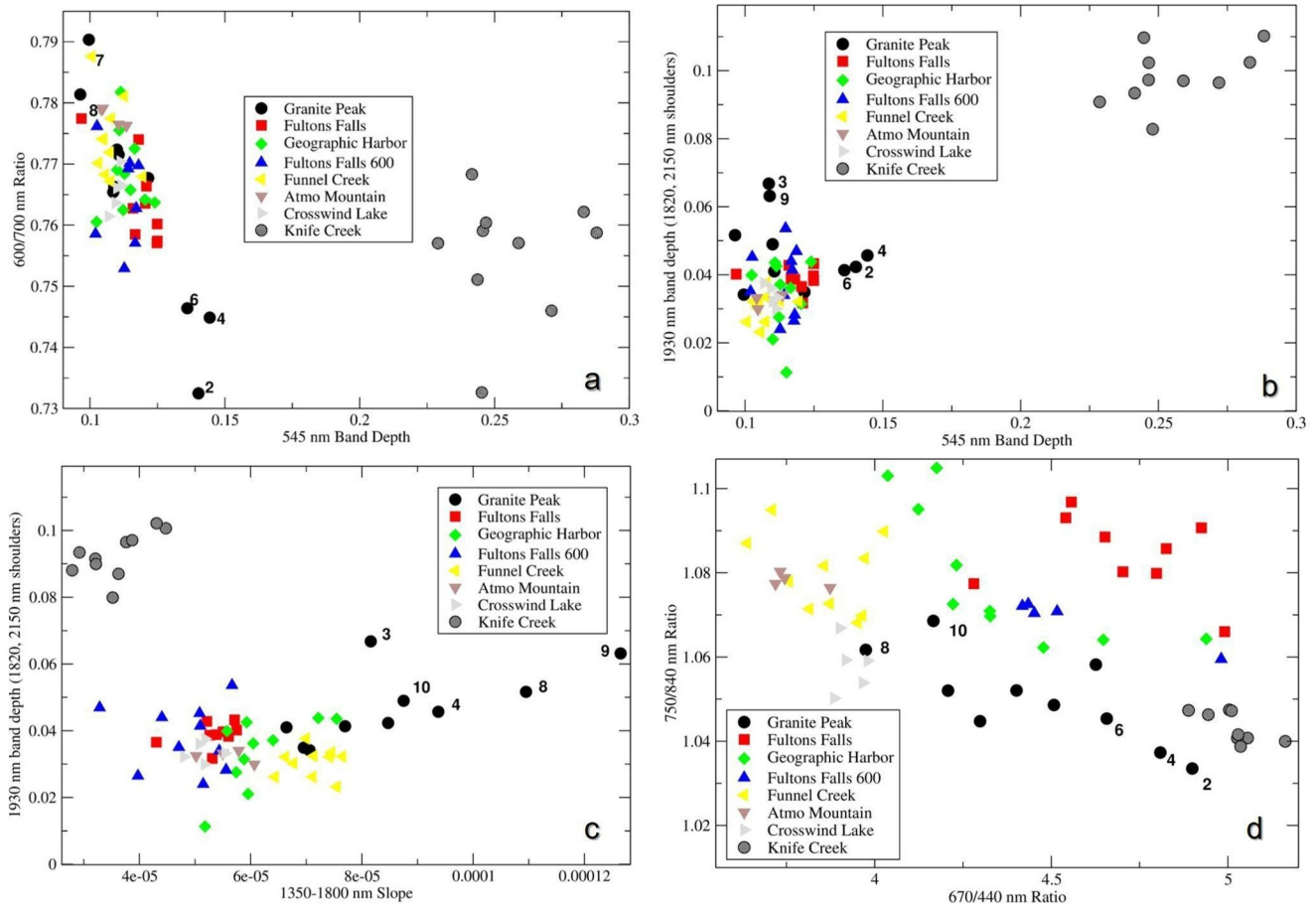


**Figure 20.** SuperCam VISIR spectral parameters for *Observation Mountain* soil targets and nearby *Knife Creek* outcrop. Numbered labels correspond to specific raster locations on undisturbed regolith target *Granite Peak*.

$$RHg \approx e/es(Tg), \quad (1)$$

where  $e = RH \times es$  (TRH) is the water vapor pressure derived from measurements of relative humidity with respect to ice (RH) and temperature (TRH) at 1.4 m made by MEDA's humidity sensor, and  $es$  is the saturation vapor pressure over ice (Polkko et al., 2023). Values of  $Tg$  and  $RHg$  suggest that changes in the hydration state of the  $MgSO_4 \cdot nH_2O$  and  $CaSO_4 \cdot nH_2O$  systems could occur during diurnal cycles. The correlation between K, S, Cl, and H in the SuperCam data (Figure 24) suggest the potential presence of K-containing hydrated salts such as sulfates. We are unaware of comparable Relative Humidity and Temperature data for K-bearing sulfates such as  $KAl(SO_4)_2 \cdot 12H_2O$  or  $K_2Fe_5^{II}Fe_4^{III}(SO_4)_{12} \cdot 18H_2O$ , but the possibility exists that hydration and dehydration of additional salts other than those included on this figure may be impacting the soil surface. In any case, though, it is uncertain whether kinetics of hydration would allow for such changes (Rivera-Valentín et al., 2021). Values of  $Tg$  and  $RHg$  in Figure 26 also suggest that frost ( $RHg > 100\%$ ) may form during early a.m. hours. However, estimated values of  $RHg$  represent an upper limit because water vapor adsorption on the ground likely occurs at night, which would reduce the water content at the ground compared to the water content at 1.4 m, and therefore the actual  $RHg$  values. It is therefore uncertain whether frost formed on the regolith sample overnight.

Following the method shown in Martínez et al. (2023), we used MEDA measurements to calculate the TI and broadband albedo of the terrain shown in Figure 25 (top). We obtained values of  $220 \pm 20$  SI units for the TI, and of  $0.20 \pm 0.01$  for the broadband albedo. The TI of dunes can be related to an effective particle size in the thermal penetration depth of surface materials (the upper few to 100 s of millimeters) using Equation 2,

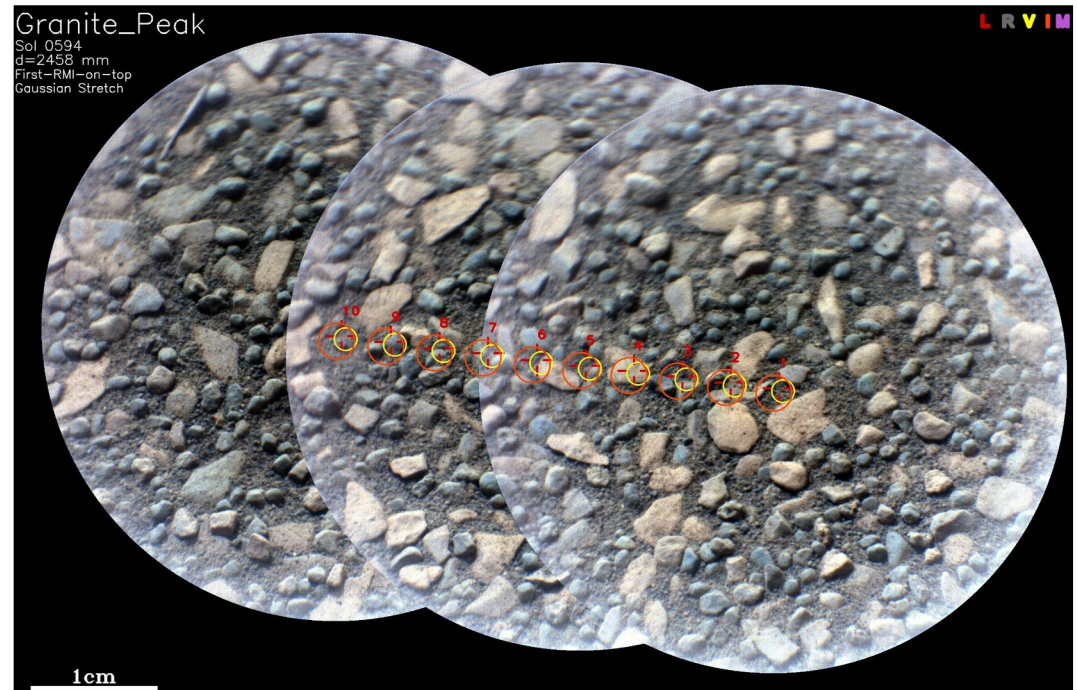


**Figure 21.** Remote Micro-Imager enhanced color mosaic of *Granite Peak* undisturbed soil target (images acquired prior to Laser Induced Breakdown Spectroscopy (LIBS) laser disturbances) from Sol 594 (scam01594), showing number locations of raster points. Red (yellow) circles correspond to approximate near-infrared (visible) fields of view of SuperCam relative reflectance spectra; red crosses correspond to LIBS target locations.

$$TI = (k\rho c)^{1/2}, \quad (2)$$

where  $k$  is the thermal conductivity,  $\rho$  is the material's bulk density, and  $c$  is the specific heat. Under Martian conditions, the thermal conductivity  $k$  of regolith has been shown empirically to depend on pressure and grain size. This relationship has been shown to be such that, at a pressure of 613 Pa,  $k = 0.00375 d^{0.467}$  when  $d$  is the grain size diameter given in mm (Presley & Christensen, 1997). Based on Edgett and Christensen (1994), sand dunes have been previously estimated to contain a bulk density  $\rho$  of approximately 1.680 g/cm<sup>3</sup>. We use 1.630 g/cm<sup>3</sup> which is also equivalent to the bulk density of a material with a porosity of 43% and solid density of 2,850 kg/m<sup>3</sup> (consistent with basalt) (Mellon et al., 2022). We assume a specific heat of  $c = 850$  J/kg/K for basaltic rocks. MEDA-TIRS has provided estimates of the TI values of aeolian ripples at Jezero, calculating TI 220 SI units (relative error 10%).

Using this information, we can infer that the bulk particle size within the *Observation Mountain* megaripple (i.e., not the size of the surficial armoring grains) is of the order of  $\sim 150$   $\mu\text{m}$ . Estimations of TI and grain size from MEDA measurements are based on methods developed in Martinez et al. (2023). This particle size is compatible with the creep, reptation, and saltation processes that create dunes and ripples on Mars. Previous studies have shown that the thermal conductivity of mixtures of grains tend to reflect the properties of the coarse grains (Presley & Christensen, 1997), but atmospheric dust (of the order of 1- to 4  $\mu\text{m}$  size) is likely also part of the bulk of the ripple and its surface based on MEDA Thermal Infra-Red Sensor (TIRS) TI measurements.

From the MEDA RDS measurements of incoming solar radiation (Apéstitigue et al., 2022; Rodriguez-Manfredi et al., 2021), it is possible to quantify the effect of dust accumulation on the windows of the photodiodes facing the zenith. This analysis shows net dust accumulation between the beginning of the dusty perihelion season and the collection of the samples (Sols 361–639): at the time of sample collection, dust accumulated on the RDS photodiode windows caused a decrease in transmitted light of approximately 20% compared to that at the beginning of the perihelion season, with most of the accumulation occurring prior to Sol 595 (Vicente-Retortillo et al., 2024).

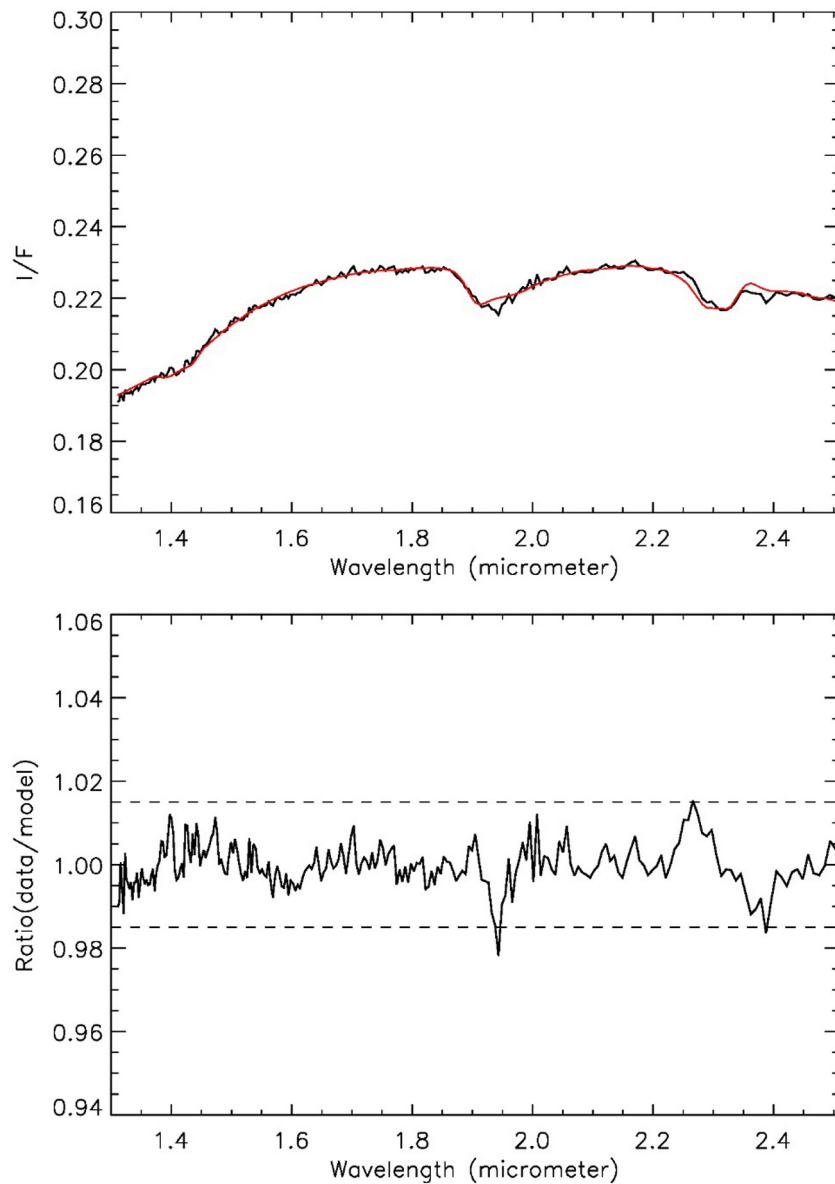


**Figure 22.** (Top panel). Comparison of the IRS data (black line) acquired on sol 594 from the *Granite Peak* target and the modeled composition (red line). (Bottom panel) Data/model ratio. The residual at 2.38  $\mu\text{m}$  can be attributed to phyllosilicates. The residual near 2  $\mu\text{m}$  may be due to the atmospheric correction.

Surfaces may have been affected by convective vortices and wind gusts that could have led to dust removal (Newman et al., 2022; Vicente-Retortillo et al., 2018); however, an analysis of albedo changes at Jezero crater induced by aeolian processes indicates that only a small fraction of dust is being removed from natural surfaces (Vicente-Retortillo et al., 2023), which is consistent with studies showing that large amounts of dust remain within coarse sand particles after dust lifting events (Greeley et al., 2005; Reiss et al., 2010). These findings (permanence of dust within coarser particles and, more importantly, the significant net dust accumulation during the perihelion season) suggest that the collected samples include recent airfall dust.

### 3.7. SHERLOC

The SHERLOC Raman spectra obtained from *Topographers Peak* (sol 598) and *Marmot Bay* (sol 600) are similar although a weaker signal was obtained at *Marmot Bay*, likely due to the greater topography in *Marmot Bay* (Figure 27). In both scans, a clear peak at  $\sim 803\text{ cm}^{-1}$  can be observed, which is similar to the background signal

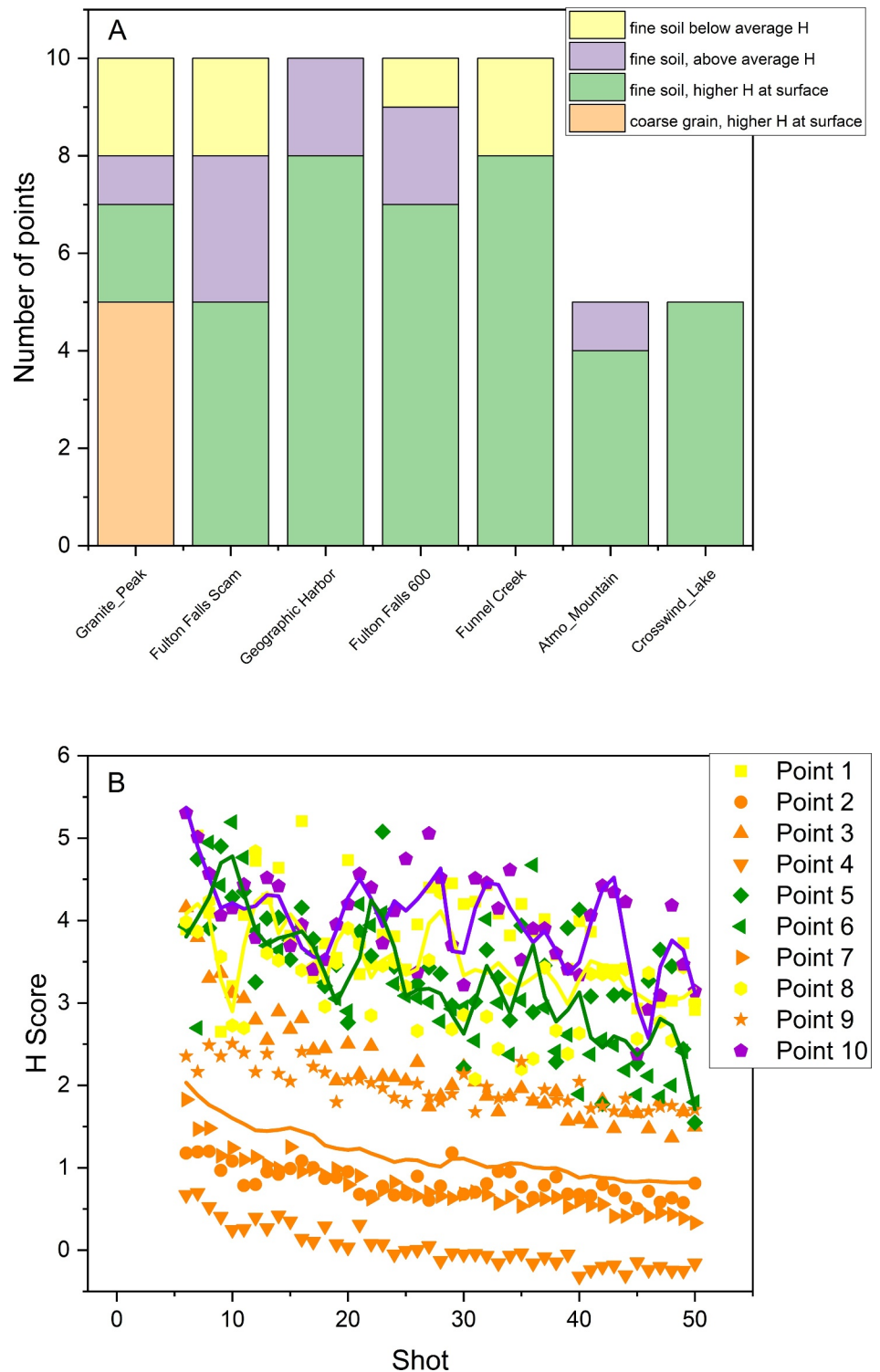


**Figure 23.** (a) An examination of the change in H scores from shots 6–10 to the bottom 10 shots shows that most fine points (39 out of 55) show a statistically significant difference. This may indicate that the Laser Induced Breakdown Spectroscopy beam is penetrating through a hydrated crust that is thinner due to the decreased time it has had to form since disturbance. (b) An example of the H profiles for the types of points shown in (a). The SuperCam Major-element Oxide Compositions (MOC), total emissivity, and all raw data and processed calibrated data files are present in the Planetary Data System (Wiens, Maurice, Deen, et al., 2021). The SuperCam H scores were generated after Forni et al. (2013). The retrieved H component used to generate the H scores (after Forni et al., 2013) can be found in Hausrath et al. (2023).



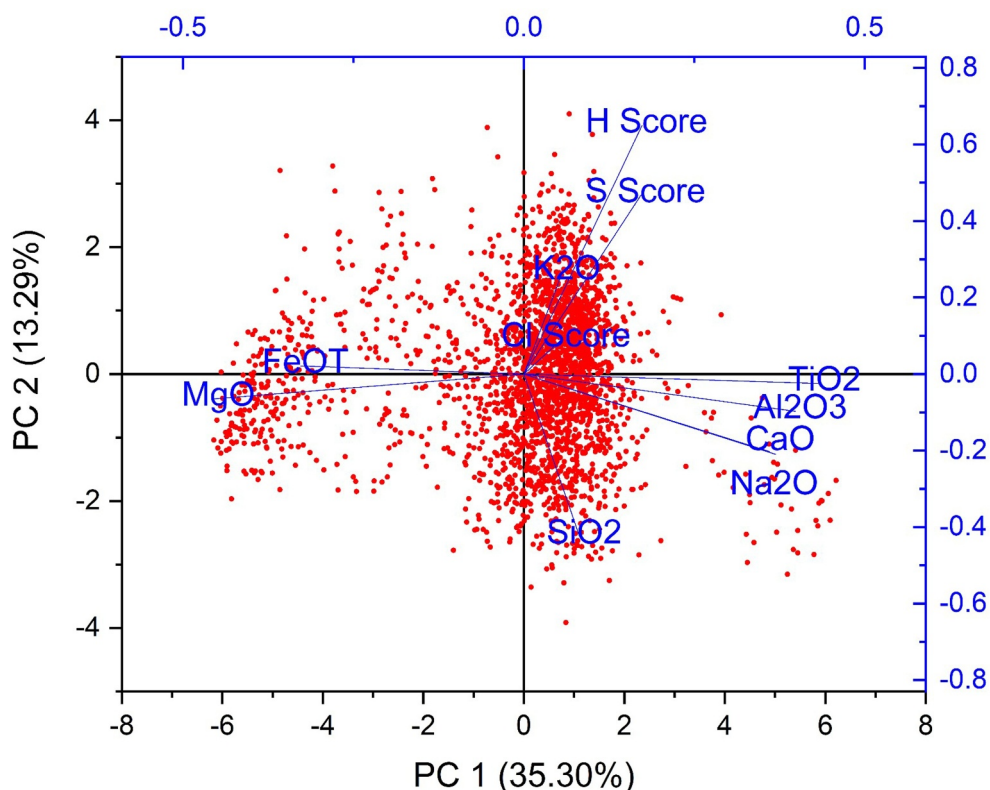


**Figure 24.** Principal Component Analysis of the fine-grained materials from *Observation Mountain* measured by SuperCam shows a correlation between S, H, Cl, and  $K_2O$ . This is similar to what has previously been observed for fine-grained material along the crater floor (Hausrath et al., 2023), and suggests the presence of hydrated salts in these materials. The SuperCam Major-element Oxide Compositions (MOC), total emissivity, and all raw data and processed calibrated data files are present in the Planetary Data System (Wiens, Maurice, Deen, et al., 2021). The SuperCam H scores were generated after Forni et al. (2013). The retrieved H component used to generate the H scores (after Forni et al., 2013) can be found in Hausrath et al. (2023). The Cl scores are generated after Cousin et al. (2025), and the S scores after Meslin et al. (2022), and documented in those publications. The shot-to-shot MOC data are in Supporting Information Table S13.

from the instrument optics (Copolongo et al., 2023). In addition, less clear peaks can be observed at  $\sim 1,077\text{ cm}^{-1}$  which are consistent with a silicate such as feldspar (Copolongo et al., 2023). Weak signals from a mix of sulfate, carbonate, and other silicate minerals present in the matrix may also contribute. No peaks indicating hydration ( $3,000\text{--}4,000\text{ cm}^{-1}$ ) were detected in either spectrum. Overall, the Raman spectra were fairly noisy, which is expected given the presence of dust and topography.

The fluorescence spectra of *Topographers Peak* show fluorescence features at 274, 285, and 285/325 nm while the spectra of *Marmot Bay* show fluorescence features at 285 and 340 nm. These fluorescence signals are consistent with inorganic sources such as  $Ce^{3+}$  in phosphate and mineral defects in silicates, and show variability in the strength of the signal across grains (Gaft et al., 2015; Scheller et al., 2022, 2023; Sharma et al., 2023; Shkolyar et al., 2021). While the signals also could arise from single and double aromatic organic molecules (Razzell Hollis et al., 2023), no definitive Raman peaks that could confirm such a detection were present. Polycyclic aromatic hydrocarbons have to date been found in Martian meteorites (Schmitt-Kopplin et al., 2023) and can potentially be formed by abiotic in situ reactions on Mars (Zolotov & Shock, 1999). However, macromolecular carbon is the more commonly found form of organic carbon in meteorites (Steele et al., 2018) and likely elsewhere on Mars (Eigenbrode et al., 2018).

### 3.8. PIXL

PIXL scans were performed on the disturbed surface of *Topographers Peak* and the undisturbed surface of *Marmot Bay*. Further details on analyses and results are provided in Shumway et al. (2024). Results of the scans

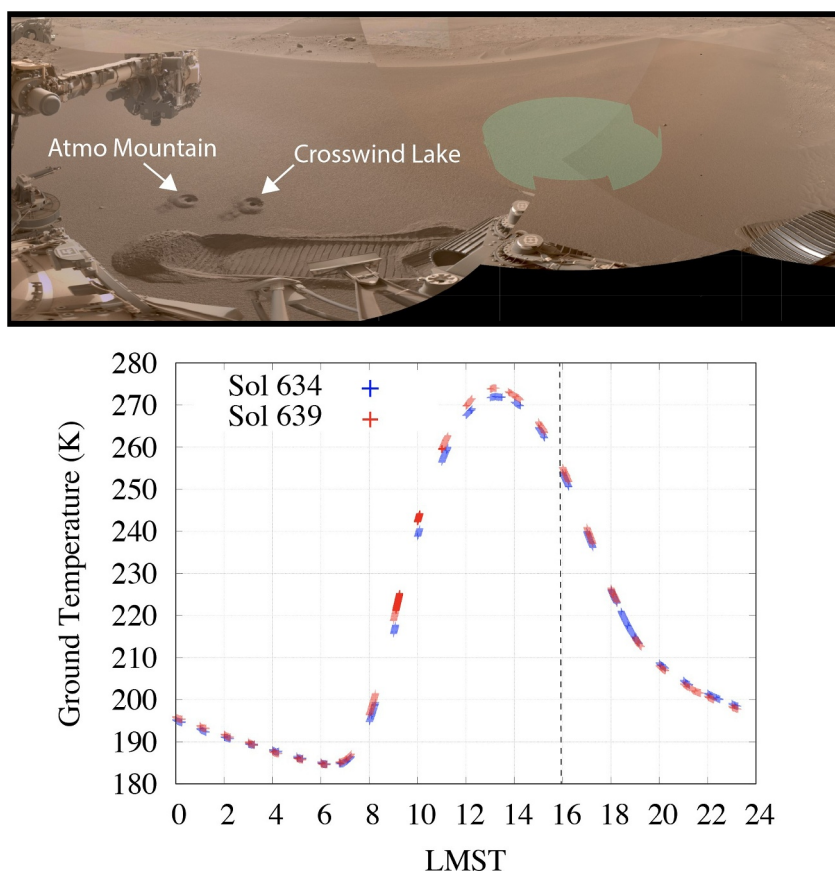


**Figure 25.** (top) Navcam mosaic from Sol 639 (ncam00709) showing the MEDA ground temperature field of view shaded in green, which covers an area of  $\sim 3\text{--}4\text{ m}^2$ , with a center  $\sim 3.75\text{ m}$  from the rover's Radioisotope Thermoelectric Generator to avoid thermal contamination. The white arrows point to both regolith sampling locations, which are separated by  $\sim 50\text{ cm}$ . (bottom) Ground temperature measurements by MEDA on Sols 634 and 639 (the sampling Sols). The starting time of sampling on both Sols is indicated by the dashed vertical line ( $\sim 15:53$  local mean solar time), with a ground temperature value of  $\sim 255\text{ K}$ .

indicate different chemical compositions of two of the populations of grains identified by WATSON and by VISIR captured in the PIXL scan area: the smaller, more rounded, darker grains, and the larger, lighter-toned, more angular grains (Figure 28, Table S5 in Supporting Information S1). PIXL also measured the composition of finer-grained material (grain size less than  $\sim 1\text{ mm}$ ) between larger grains. Analyses of diffraction anomalies in the X-ray spectra indicate that diffraction is present in the smaller, darker grains, which suggests a crystalline primary mineral phase, whereas the larger, lighter grains do not have a coherent pattern of diffraction, which is consistent with poorly ordered secondary phases that have been altered.

#### 4. Discussion

The collected samples will allow the analysis of a potential widespread or global soil component; airfall dust, which can help understand the global component of Martian soil, the past climate of Mars, surface-atmosphere interactions, and atmospheric circulation; and the soil crust, which likely results from ongoing interactions with volatiles including liquid water. In addition, the collection of altered large lithic fragments likely including mudstone allows the analysis of ancient aqueously altered, potentially habitable, and possibly biosignature-containing environments (Bosak et al., 2024). Data acquired during the sample collection process indicate that the collected regolith has the potential to address these questions once the samples are returned to Earth by MSR.

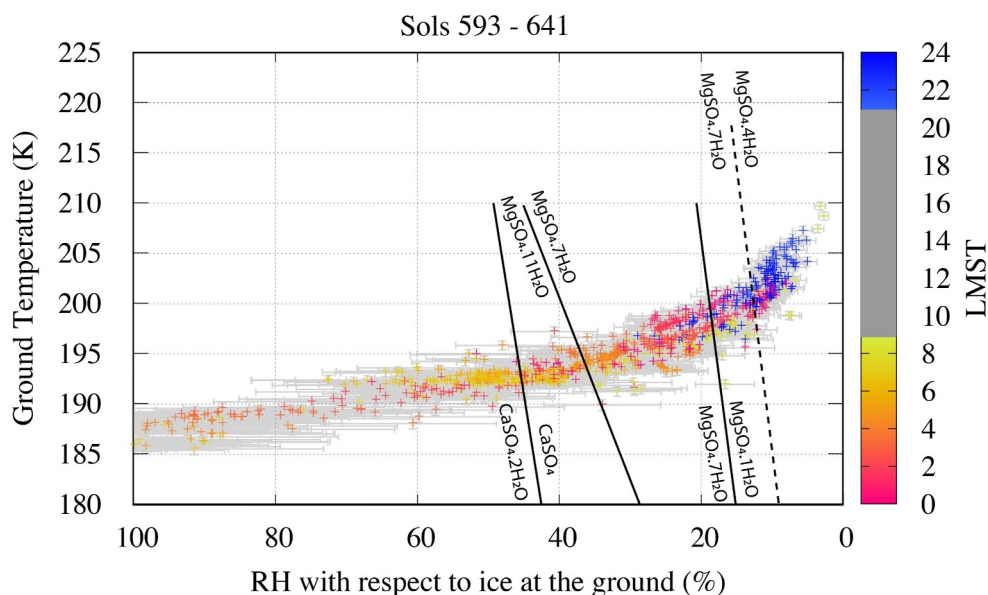


**Figure 26.** Measured ground temperature as a function of estimated relative humidity at the ground and the local mean solar time (LMST) (color bar) for the Sols from formation of the scuff to the Sol the rover drove away from *Observation Mountain*. Error bars are shown in gray, while the superimposed lines represent stable (solid lines) and metastable (dashed lines) boundaries for the  $\text{MgSO}_4 \cdot n\text{H}_2\text{O}$  and  $\text{CaSO}_4 \cdot n\text{H}_2\text{O}$  systems. Only shown are values between 21:00 and 09:00 LMST, when RH was above the detecting threshold (2%). If kinetics permit, salts present in the Martian regolith sample might experience changes in their hydration state under conditions present during sampling. Saturation states of 100% also suggest that frost may possibly form.

#### 4.1. Comparison of the Fine-Grained Material to Proposed Global Martian Soil Components

Previous analyses of soils on Mars indicate both that there is an apparent global component (e.g., Clark et al., 1982; S. R. Taylor & McLennan, 2009; Yen et al., 2005) and that various soil-forming processes result in widely variable soil components, particularly volatiles (e.g., Figure 2). Fine-grained material measured by SuperCam at *Observation Mountain* and by PIXL at the undisturbed surface at *Marmot Bay*, and the disturbed surface of *Topographers Peak* indicates that the fine grained material measured at Jezero is very similar, but not identical to previous measurements of soil on Mars (e.g., O’Connell-Cooper et al. (2017)) (Figure 29), as well as to fine-grained material measured throughout *Perseverance*’s traverse in Jezero crater (Cousin et al., 2025).

This comparison shows that both PIXL and SuperCam results indicate that, due to this similarity, the fine-grained material measured here will likely help understand soil-forming processes on Mars. The differences between SuperCam averages and PIXL averages are likely due to the different locations in which they were measured, as well as the different measurement size (PIXL spot size  $\sim 120 \mu\text{m}$  (Allwood et al., 2020) versus SuperCam spot size  $\sim 350 \mu\text{m}$ ). Laboratory experiments have also indicated that where grains  $< 500 \mu\text{m}$  in size contain a coating, the LIBS measurements only measure the coating rather than the underlying grain (David et al., 2021). Analysis of the returned grains will help identify any such coatings.

Grain size analyses further support the likely collection of a widespread, possibly global soil component in this collected regolith sample. Analysis of images of the disturbed regolith surface at *Topographers Peak* indicate a mean grain size of  $\sim 125 \mu\text{m}$  (Figure 15), comparable with MEDA grain size measurements of  $\sim 150 \mu\text{m}$ . This grain size range is also likely to persist for long periods of time on Mars, and be widely mobile (Figures 3 and 4), contributing to the conclusion that the collected regolith sample likely contains a sample of a widespread and possibly globally distributed soil.

However, despite the similarity of the collected sample to previous measurements and a proposed global soil component (e.g., Figure 29), the extent and causes of variability in the soil are also important to understanding surface processes. LIBS measurements of the fine-grained material at *Observation Mountain* trend between the

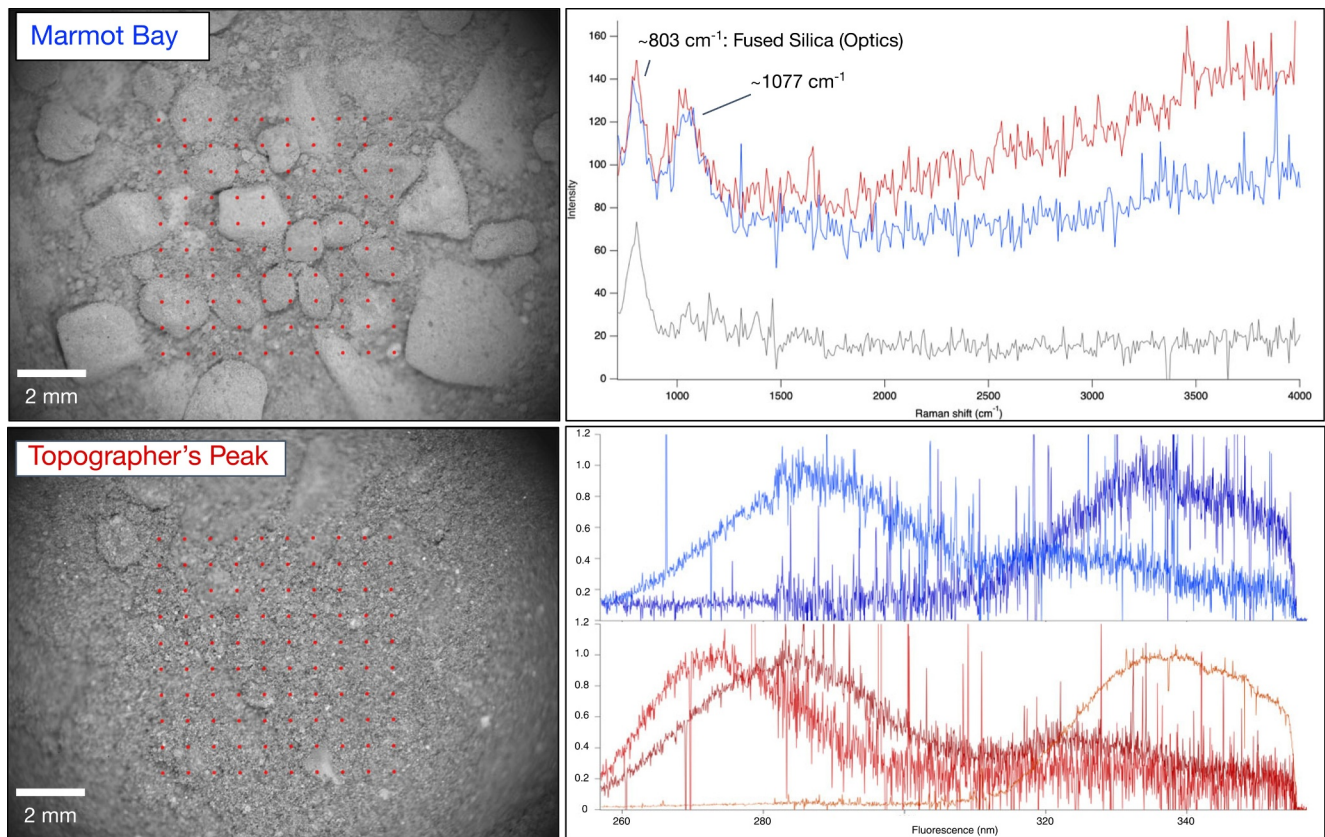


**Figure 27.** SHERLOC  $10 \times 10$  point scans of *Marmot Bay* and *Topographer's Peak*. Left top and bottom panels show Autofocus Context Imager images ( $\sim 4.8$  cm standoff) of each target with SHERLOC analysis points in red. In the right top panel trimmed mean Raman spectra from *Marmot Bay* (blue) and *Topographer's Peak* (red) are shown in comparison to the instrument background (gray). The  $1,077 \text{ cm}^{-1}$  peak is broad, and could be due to a mix of mineral  $\nu_1$  modes including feldspar (Corpolongo et al., 2023). In the right bottom panel mean fluorescence spectra from *Marmot Bay* (blue) and *Topographer's Peak* (red) are shown; y-axis shows intensity normalized to 1 and offset for clarity. Mean normalized spectra are presented. *Topographer's Peak* has three distinct fluorescence patterns: lambda max at 338, 274, and 285/325 nm. *Marmot Bay* has two distinct fluorescence patterns: lambda max at 337 and 285/325 nm. The SHERLOC and WATSON data are available in the Planetary Data System (Beegle et al., 2021). Spectroscopy files are available for sol 598 (Topographer's Peak) and sol 600 (Marmot Bay) in the data\_raw\_spectroscopy folder in csv format, with the character groups "ERA" (active spectra) and "ERB" (dark spectra) in the file names. The spectral data shown above is active-dark spectra. Image files are available for each sol in the data\_aci\_imgops and data\_watson\_imgops folders, in "edr" subfolders, in .IMG format with the character groups "ECM", "ECZ", and "EZS" in the file names.

augite-like composition of the fine-grained regolith analyzed up to Sol 602 that likely represents a relatively uniform mixture of mafic and felsic minerals, and an olivine endmember (Figure 30b). Few analyses show a largely felsic composition. This predominance of mafic minerals in the *Observation Mountain* megaregion is also shown in an A-CN-K-FM plot (Figure 30a), where most analyses are situated toward the mafic corner of the ternary plot. SuperCam LIBS data largely plot below the mafic-felsic mixing line indicative of minimal open-system chemical weathering as Al is not enriched relative to other elements for most LIBS points. Some targets such as the *Fultons Falls* (Sol 600) SuperCam target have points that are situated above the mafic-felsic line potentially indicative of open-system alteration, chemical weathering, and the potential presence of carbonate (see also Figure S5 in Supporting Information S1 of carbonate levels measured by SuperCam LIBS on the *Granite Peak* target (Sol 594)). For *Fultons Falls*, these are points #3 and #5. Point #3 is situated on a large, angular grain which also has a more felsic chemistry (Figure 30b), while point #5 is situated in the fine-grained material suggesting that altered materials are distributed between both fine and coarse grain sizes (Figure 30). Olivine can become enriched as a result of physical grain segregation during aeolian transport or through the reworking of local olivine-rich bedrock, as has been hypothesized for the lithified aeolian deposits in Gale crater (Bedford et al., 2020, 2022). Given the abundance of olivine-rich bedrock within Jezero crater, such as that within the

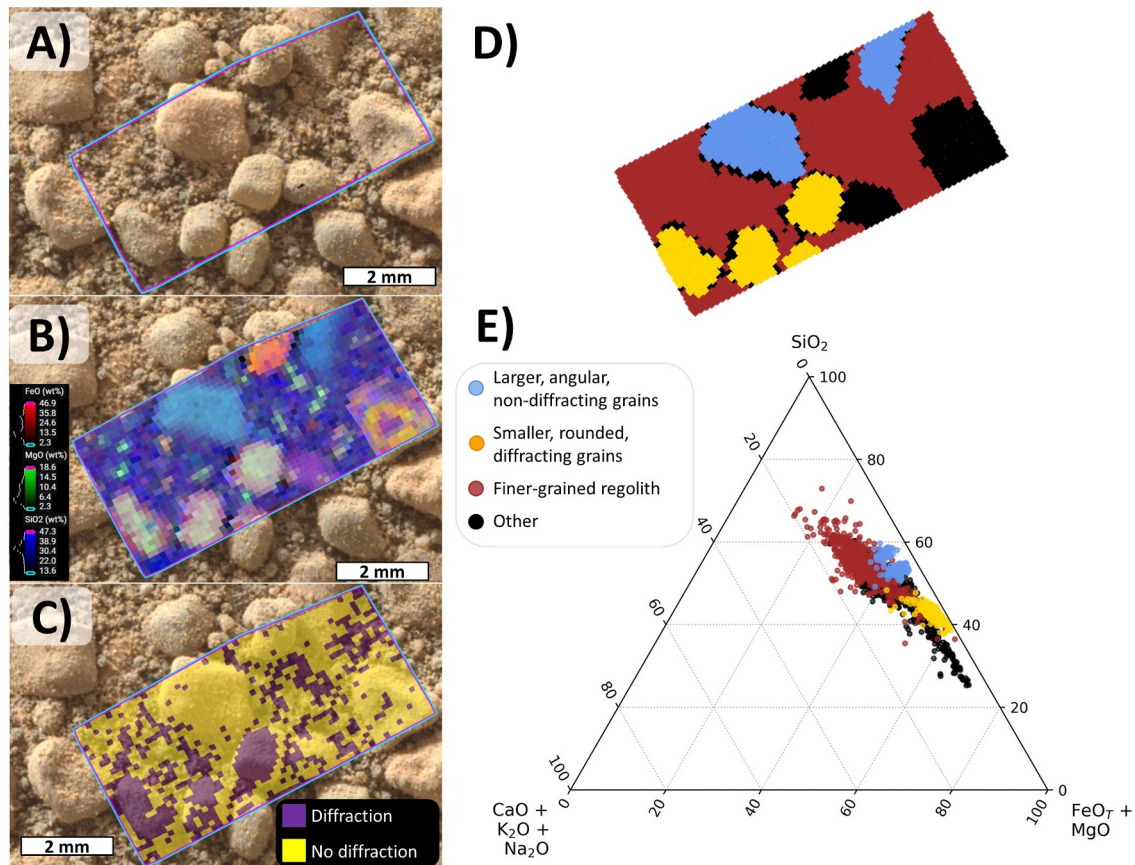


**Figure 28.** (a) The approximate location of PIXL's scan on the *Marmot Bay* target on sol 601, on a WATSON image. (b) Color mapping showing the chemical composition of the larger, lighter, more angular grains (pale blue), and the smaller, darker, more rounded grains (gray) (see also Table S5 in Supporting Information S1 and Shumway et al., 2024). (c) Color mapping showing the areas where PIXL detected diffraction anomalies. Purple areas show points where PIXL detected diffraction peaks in the X-ray spectra, which indicate crystalline regions (Tice et al., 2022); yellow areas show points where no diffraction was detected, which may indicate amorphous or microcrystalline (<40–50  $\mu\text{m}$ ) regions (Tice et al., 2022). A lack of diffraction in the larger, more angular, lighter-toned grains may be evidence of alteration of primary minerals (for further discussion, see also Shumway et al., 2024). (d) A color-coded map showing which grains and regions are plotted on the subsequent ternary plot. (e) A ternary plot showing the compositions of the different populations of grains captured in the scan area. Further interpretation of PIXL's findings, including the regions labeled "other," can be found in Shumway et al., 2024.

Séítah formation, a local contribution for the olivine is likely for coarser grains of the Observation Mountain megareggle. This is also consistent with studies of coarse regolith of the crater floor by Vaughan et al. (2023). The higher degree of scatter of SuperCam data toward the olivine endmember compared to other fine-grained regolith targets in Jezero crater suggest that there may also be some olivine enrichment during aeolian transportation in this aeolian deposit in comparison to previously analyzed regolith targets. Overall, SuperCam LIBS data support that the sample collected from this megareggle will likely contain a mixture of olivine-rich local Séítah-like material and material transported from a longer distance with some grains that have experienced alteration.

Due to both the observed similarity to previous, potentially global soils (Figure 29) and variability between the grains within the sample (Figure 30), this regolith sample will be very valuable for serving as a ground truth for in situ measurements from Gale crater, the MER landing locations, and the Viking locations. In addition, this sample of a global soil will be of immense value to future human exploration (Grady et al., 2022) to understand potential previously unconsidered threats. For example, the lunar regolith was found to be very abrasive and damaging to the astronauts' space suits. Understanding the characteristics of the fine-grained soil contained in this sample will be a very valuable contribution to understanding surface processes on Mars.

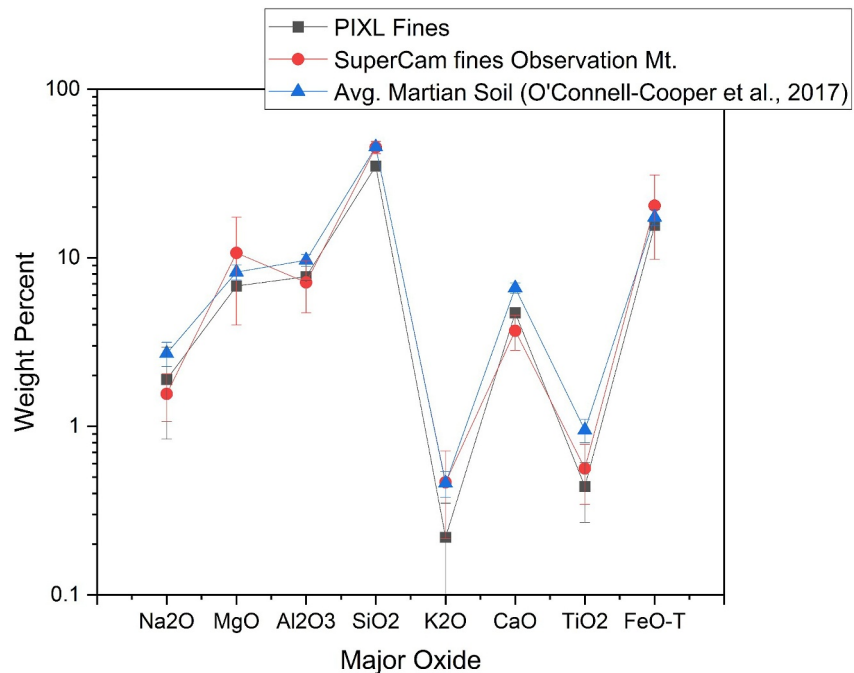


**Figure 29.** Major oxide concentrations compared for PIXL measurements of the fine grains from *Marmot Bay* and *Topographers Peak*, SuperCam fine grains from *Observation Mountain*, and previously published values for an average basaltic Martian soil (O'Connell-Cooper et al., 2017)—for further comparisons between PIXL measurements of soil and previous measurements of soil on Mars see Shumway et al. (2024).

#### 4.2. Probable Airfall Dust Component in the Collected Sample

A sample of airfall dust may help understand the modern and recent past climate of Mars, in which the dust cycle (and especially dust storms) provides the largest source of Sol-to-Sol and year-to-year variability (Forget & Montabone, 2017; Martinez et al., 2017; Read et al., 2015). The large impact of dust on climate is primarily via the major radiative (and thus heating and cooling) effects of lofted dust particles in the thin Martian atmosphere, with those effects depending on their size, shape, and composition, all of which have to date been inferred from remote sensing only (Wolff et al., 2017). Storm-related and seasonal dust increases have also been shown to greatly increase atmospheric water escape rates (Haberle et al., 2003). Further, dust-driven variations in visibility, temperature, atmospheric density, and wind are highly relevant to Mars mission planning, in terms of arriving on or leaving the surface and surface operations. Although the size distribution of the dust within the megaripple may be different from airfall dust, the ability to measure the shape, size distribution, and composition of a Martian dust sample provides a valuable data point to constrain dust models.

Studies of airfall dust will also contribute to a better understanding of the health and mechanical hazards of dust for future human exploration of Mars (Grady et al., 2022), and multiple lines of evidence suggest the presence of dust in the regolith sample. These include evidence of dust clearing by LIBS in RMI images indicated by changes in the red channel in before and after images which are consistent with the removal of ferric dust (Figure 16); bright grains in ACI images (Figure 5); and TI measurements by MEDA TIRS. Furthermore, the relative immobility of the megaripple indicates that there was time for ancient dust to have accumulated.

The first shots during LIBS analyses are considered to be measurements of airfall dust (Lasue et al., 2018, 2023; Meslin et al., 2013). Following the method of Lasue et al. (2023), the composition of dust in the regolith sample is likely to be similar for SiO<sub>2</sub>, Al<sub>2</sub>O<sub>3</sub>, and K<sub>2</sub>O to previous measurements of dust from Gale crater, but differs outside uncertainty for Na<sub>2</sub>O, MgO, CaO, TiO<sub>2</sub>, and FeO<sub>T</sub> (Figure 31).

#### 4.3. Probable Soil Crust Components in the Collected Sample

In addition to atmospheric dust, the regolith sample also sampled the soil crust present at *Observation Mountain* (Figure 10), which is ubiquitous at Jezero crater (Hausrath et al., 2023), and across Mars (e.g., Arvidson,

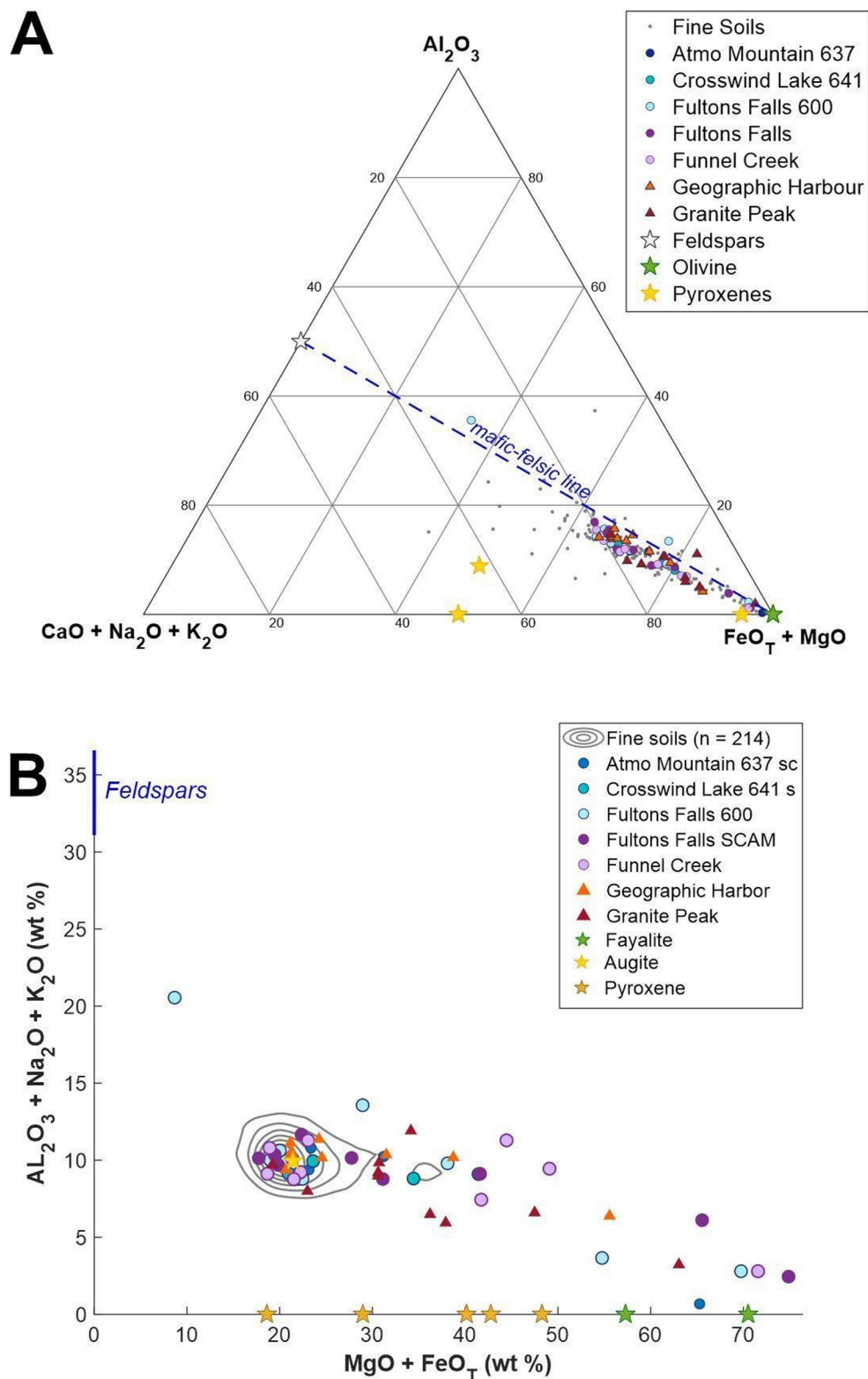


Figure 30.

Anderson, Bartlett, Bell, Blaney, et al., 2004; Arvidson, Anderson, Bartlett, Bell, Christensen, et al., 2004; Arvidson, Poulet, et al., 2006; Arvidson et al., 2009; Clark et al., 1982; Moore et al., 1987; Sullivan et al., 2011; Weitz et al., 2020). Although the soil crust will not be preserved intact in the sample tube, the components will remain in the tube. An analysis of the shot-to-shot SuperCam LIBS measurements that sample the top 1–2 mm (Meslin et al., 2013) of the soil from *Observation Mountain* using PCA shows a tight correlation of S, H, Cl, and K<sub>2</sub>O (Figure 24), and decreasing H scores with depth (Figure 23). This result suggests that a hydrated sulfate component, potentially containing potassium, could be present in the top 1–2 mm (Meslin et al., 2013) of the Martian soil, helping to cement the soil and generate the soil crust. The MEDA measurements record the presence of relative humidity and temperature values that indicate that sulfate salts, if present, could potentially hydrate and dehydrate, contributing to the formation of the observed soil crust (Figure 10). In addition, saturations that reach 100% indicate that frost could potentially be present (Figure 26).

During storage of the sample tubes on the surface of Mars and in the *Perseverance* rover, as well as during transport back to Earth, hydrated salts and frost are likely to undergo changes. For example, the sample tubes are estimated to reach temperatures as high as 28°C (Farley et al., 2020) and the temperature cycling may lead to changes of humidity in the tube, and therefore changes of the hydration states of salts, affecting the gas content of the tube. It is reasonable that at high temperatures water may be released from the hydrates, and accumulate in the headspace gas (increasing the water partial pressure  $e$ ), whereas at low temperatures water will be captured again (decreasing the water partial pressure  $e$ ). In equilibrium, at a water partial pressure  $e$ , the Relative Humidity, RH ( $T$ ) =  $e_{s,w}(T)/100$  with  $e_{s,w}$  the saturation vapor pressure over liquid water  $e_{s,w} = 611.2 * \exp(17.62(T - 273.14159)/(243.12 + (T - 273.14159)))$  or the saturation vapor pressure over ice  $e_{s,i}(T) = 611.2 * \exp(22.46 * (T - 273.14159)/(272.62 + (T - 273.14159)))$ . Since the temperatures of the tubes may change rapidly during a given day by about 100°C (between day and night) reaching temperatures of up to 28°C, this closed system may be out of equilibrium and it is difficult to calculate how the water vapor pressure  $e$  will change within the tube with the desorbed and absorbed water. This type of change in salts should be investigated using analog samples in tubes prior to return of the samples, to best interpret analyses upon their return.

#### 4.4. Altered Grains in the Collected Sample and Their Potential Source Regions

In addition to more recent arid processes on Mars, the material contained within the collected samples can help interpret ancient Martian processes which involved liquid water. Multiple lines of evidence indicate that the coarse grains measured at *Observation Mountain* contain altered material. SuperCam VISIR analyses show higher hydration within the larger, lighter, less spherical grains, indicating the likely presence of water within the samples that can be analyzed upon return to Earth. Hydrated minerals such as sulfates and phyllosilicates have been extensively detected elsewhere in the Fan Front (Dehouck et al., 2023; Farley & Stack, 2023b; Phua et al., 2023), and SHERLOC measurements show the presence of aqueously generated phases such as sulfates and carbonates in the Fan Front (Phua et al., 2023; Roppel et al., 2023; Siljeström et al., 2024). Furthermore, PIXL's lack of detection of diffraction suggests a loss of crystallinity likely due to aqueous alteration (Figure 28).

Future measurements of these aqueously altered grains from *Observation Mountain* can be placed into context by an assessment of the source of the grains using in situ data. Similarities in SuperCam VISIR measurements indicate that the smaller, darker, more spherical grains are likely from the Séítah region, and the larger, lighter, more angular grains are potentially from *Knife Creek* and *Devil's Tanyard*. PIXL chemical results, SuperCam

**Figure 30.** (a) An Al<sub>2</sub>O<sub>3</sub>-CaO + Na<sub>2</sub>O + K<sub>2</sub>O-MgO + FeO<sub>T</sub> ternary diagram showing the SuperCam Laser Induced Breakdown Spectroscopy (LIBS) targets on the *Observation Mountain* megaripple in comparison to the fine soils (gray points) and primary igneous minerals that include pyroxenes (augite, hedenbergite, and diopside), olivine, and plagioclase feldspars (anorthite to albite). Also plotted is the mafic-felsic trendline (dashed blue line). Data that plot above the mafic-felsic trendline may be indicative of alteration as Al<sub>2</sub>O<sub>3</sub>, an element oxide that is considered largely immobile in circum-neutral chemical weathering environments, is enriched relative to the elements within mafic and felsic minerals (Babechuk et al., 2014); data below the mafic-felsic trendline are less likely to be substantially altered by open system processes that enrich aluminum. Points above the mafic-felsic line (*Fultons Falls* (Sol 600)) SuperCam target points #3 and #5 and *Granite Peak* (Sol 594) SuperCam target point #9 may also contain carbonate (see also Figure S5 in Supporting Information S1 of carbonate levels measured by SuperCam LIBS on the *Granite Peak* target (Sol 594)), and (b) a biplot of Al<sub>2</sub>O<sub>3</sub> + Na<sub>2</sub>O + K<sub>2</sub>O (elements found in feldspar minerals) against MgO + FeO<sub>T</sub> (elements found in mafic minerals such as olivine and pyroxene) showing the SuperCam analyses from *Observation Mountain* compared to SuperCam analyses of fine grains along the rover traverse up to Sol 602 represented as gray density contours. Also plotted as stars are primary igneous minerals including olivine (green), pyroxene (yellow), and a blue line representative of the range in feldspar compositions. This plot has been useful in understanding the extent of grain segregation during aeolian transport in Gale crater (Bedford et al., 2020). It shows that the fine grains along the rover traverse are a uniform mixture of felsic and mafic minerals, but the fine grains at *Observation Mountain* have a higher number of mafic grains that trend toward an olivine composition and one point that is more felsic.



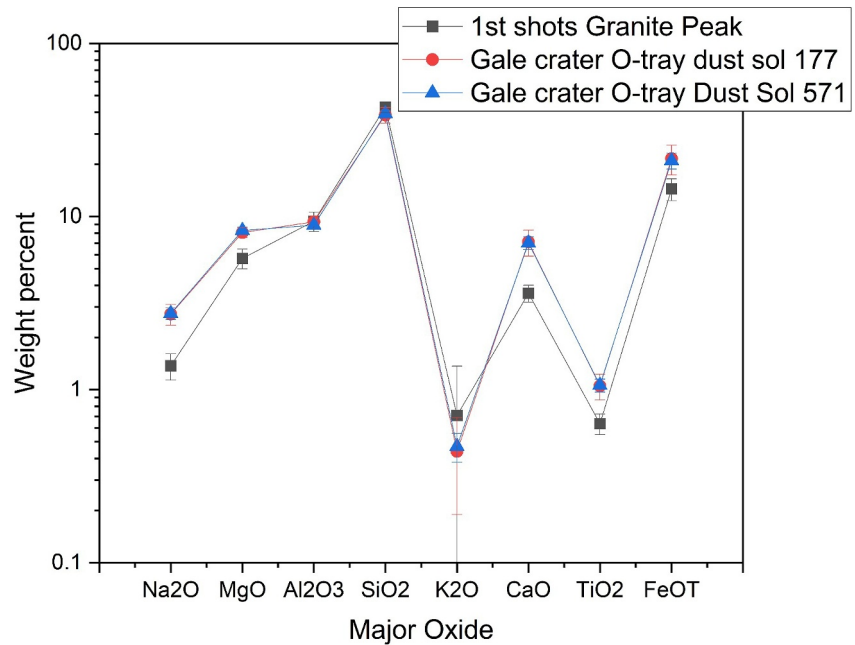


**Figure 31.** A plot of the first shots from *Granite Peak*, considered to be dust (Lasue et al., 2023) compared to previous dust measurements from Gale crater (Berger et al., 2016), indicating that the composition of the dust at *Observation Mountain* is similar for  $\text{SiO}_2$ ,  $\text{Al}_2\text{O}_3$ , and  $\text{K}_2\text{O}$  but differs outside uncertainty for  $\text{Na}_2\text{O}$ ,  $\text{MgO}$ ,  $\text{CaO}$ ,  $\text{TiO}_2$ , and  $\text{FeO}_T$ , from the composition of previously measured samples of airfall dust.

LIBS results (Figure 32 and Figure S4 in Supporting Information S1) and Mastcam-Z measurements are consistent with these results. In particular, the color and shape of the larger, lighter, more angular grains appear consistent with derivation from a distinct, continuous pinkish horizon outcropping at the top of *Knife Creek*

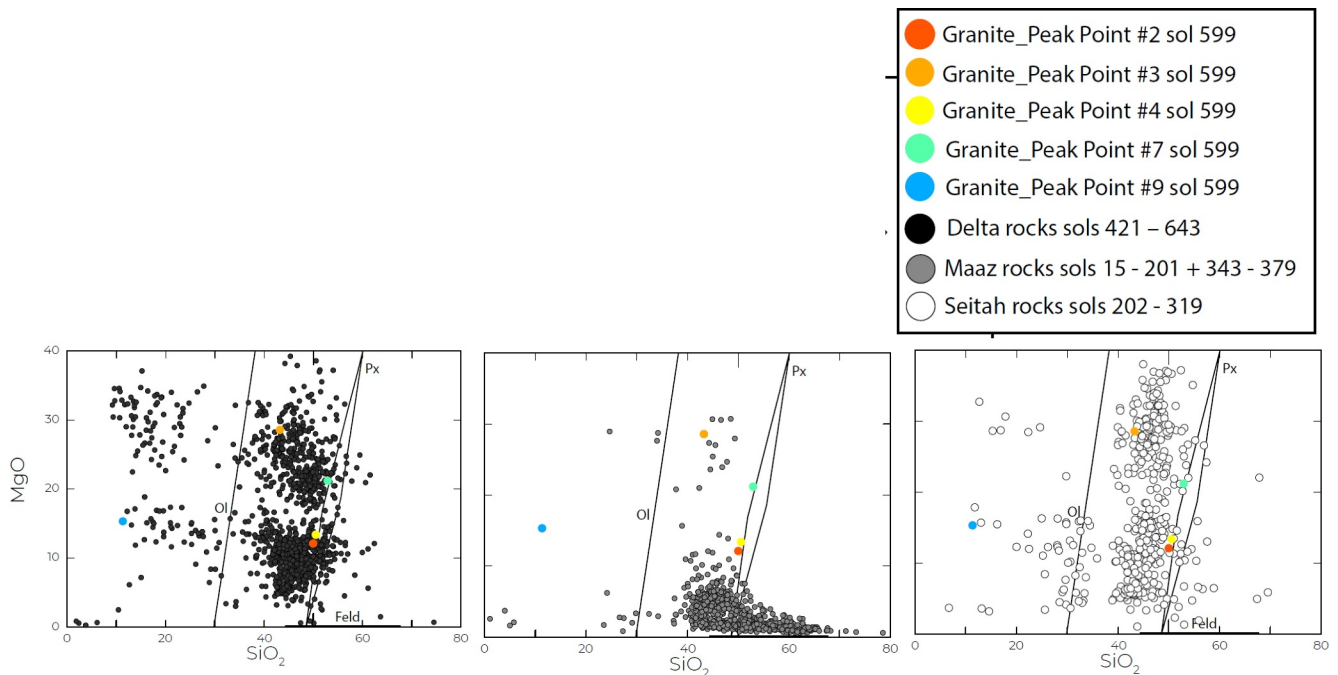


**Figure 32.** Laser Induced Breakdown Spectroscopy of the coarse grains are consistent with potential origin of the grains from the Fan (the light-toned pebbles), and Seitah (the darker-toned grains).



**Figure 33.** Rock outcroppings of upper Cape Nukshak, just above (northeast of) the sampled megaripple *Observation Mountain*. For scale, the block below the word Alagnak is about 1 m across. Of particular note is a distinct un-named horizon (grouped with the *Knife Creek* Member in the stratigraphy of Stack et al. (2024)) that runs continuously along upper Cape Nukshak, just above the line of megaripples that includes *Observation Mountain*. This horizon is “pink” in this particular contrast stretch, platier, and often more resistant than the main *Knife Creek* material, and erodes into the typically chippy fragments shown, making it a candidate source for the pink fragments observed at the *Observation Mountain* regolith sampling site (Portion of Mastcam-Z mosaic from Sol 424 (zcam08447)).

(passing within meters of *Observation Mountain*), which erodes into similar tabular, platy fragments littering the slope immediately below (Figure 33).

#### 4.5. Quantifying Potential Alteration of the Coarse Grains Using $\tau$

In order to examine the extent of alteration of grains on *Observation Mountain*, the chemistry of the coarse grains in the regolith sampling location measured by PIXL can be compared with potential parent material also measured by PIXL. The calculation of  $\tau$  (Anderson et al., 2002; Brimhall & Dietrich, 1987) was used, which compares the chemistry of weathered and parent material, using an assumed immobile element (Equation 3),

$$\tau_{i,j} = \frac{C_{j,w}}{C_{j,p}} \frac{C_{i,p}}{C_{i,w}} - 1. \quad (3)$$

Here  $\tau_{i,j}$  is the fraction of mobile element or mineral  $j$  lost or gained making the assumption that element or mineral  $i$  is immobile, where  $C$  indicates concentration,  $w$  indicates weathered material, and  $p$  indicates parent material. Where  $\tau > 0$ , the element is enriched relative to parent material, where  $\tau < 0$ , the element is depleted relative to parent material ( $\tau = -1$  is completely depleted relative to parent material), and where  $\tau = 0$ , the element is immobile.

Titanium, which is commonly used as a presumed immobile element (e.g., Hausrath et al., 2008, 2018; Sak et al., 2004, 2010; Yesavage et al., 2015), was used in these calculations. PIXL measurements of the *Quartier* abrasion patch were used as a potential *Séítah* parent material for the smaller, darker, more rounded grains, and PIXL measurements of the *Buzzard Rock* sample were used as a potential parent material for the larger, lighter, more angular material (see Table S6 in Supporting Information S1 for values used in the calculations).

Results of the  $\tau$  calculations indicate that for the smaller, darker grains, Na, Mg, Si, Cl, Ca, Mn, and Fe were depleted, and Al, P, S, and Ni were enriched. For the larger, lighter, more angular grains, Na, S, Ca, K, Mn, and Cr were depleted, and Mg, Al, Si, P, Cl, Fe, Ni, Zn, and Br were enriched. The grains and *Buzzard Rock* are natural surface targets, and thus introduce the factor of dust into these calculations (likely particularly important for Al). As such, final analysis will only be able to be performed upon return to Earth. Regardless, these results shed light on potential types of aqueous alteration. For example, the enrichments in P observed in both types of grains may result from similar processes as enrichments that have been documented in similar calculations at Gale crater (Hausrath et al., 2018; Yen et al., 2017) attributed to potential phosphate sorption and formation of Fe-phosphates, respectively. In addition, enrichments in Zn in the larger, lighter grains may indicate hydrothermal alteration (Berger et al., 2017). Aqueous alteration indicated by these  $\tau$  calculations (Figure 34) is consistent with the non-

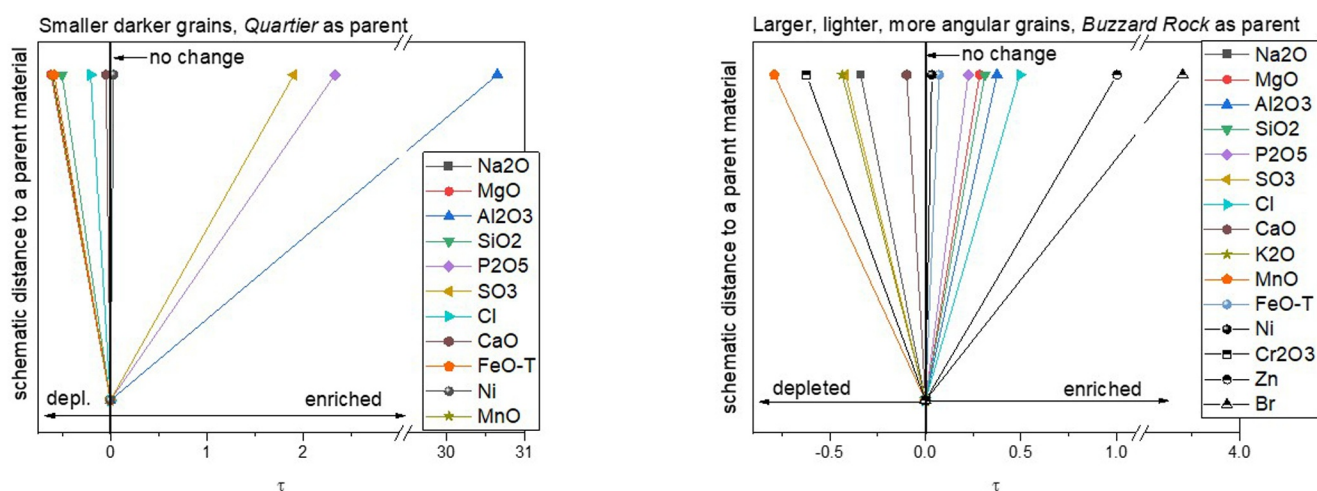


**Figure 34.** Calculation of  $\tau$  for the smaller, darker grains (left), and larger, lighter, more angular grains (right) using the Séítah sample *Quartier* and *Buzzard Rock* as parent material respectively, and Ti as the presumed immobile element for both. Results of the  $\tau$  calculations for the smaller, darker grains indicate that S, Al, P, and Ni are enriched relative to *Quartier*, and Na, Mg, silica, Cl, Ca, Mn, and Fe are depleted. For the larger, lighter, more angular grains, Al, P, Mg, Si, Cl, Fe, Ni, Zn, and Br are enriched, and Na, S, Ca, K, Cr, and Mn are depleted relative to *Buzzard Rock*. Although more definitive analysis is only possible upon return of the samples to Earth, these analyses indicate the types of constraints that these samples will likely be able to place upon past alteration on Mars upon their return to Earth by Mars Sample Return.

detection of diffraction within some of the grains measured by PIXL (Figure 28). These results therefore indicate that the grains collected in the regolith sample will provide additional insight into alteration of the Séítah region, as well as alteration on Mars more broadly.

#### 4.6. Returned Sample Considerations

The regolith sample was selected to best meet the goals of the MSR campaign (e.g., Table S7 in Supporting Information S1). Assessment of the sample indicates that airfall dust (Section 4.2), fine-grained material (Section 4.1), evidence of interactions with the atmosphere including a soil crust (Section 4.3), and aqueously altered materials that may represent past habitable, and inhabited, environments (Sections 4.4 and 4.5) are all present in the sample. With no sample of dust alone, some of the goals of the return of a regolith sample cannot be completed, and a bit tip depth of 6.5 cm limits the ability to examine deep regolith, a desired goal of MSR. However, overall, the returned sample will address most goals of the return of a regolith sample.

This interpretation is corroborated by the assessment of the scientific value of the regolith sample at the Science Community Workshop on the proposed First Sample Depot. It was concluded that the regolith sample will facilitate partially or fully, almost all of the iMOST scientific objectives that are applicable to Jezero Crater, see the SAMPLE SCIENCE TRACEABILITY MATRIX in Czaja et al., 2023. The goal where the regolith sample falls short is in Planetary Scale Geology, for which more distant samples should be available and compared (Czaja et al., 2023).

### 5. Conclusions

In situ analyses of Martian regolith at the *Observation Mountain* target revealed the presence of coarse-grained material that is likely both locally derived and transported from an intermediate distance, as well as fine-grained material of a potentially global origin. Airfall dust was collected which, along with the collected soil crust components, should provide important information on surface-atmosphere interactions and climate processes. The coarse grains are aqueously altered, which provides an opportunity to examine samples from past water-containing environments that may have been habitable, and could therefore contain evidence of ancient Martian life. The analysis of these samples also provides a critical step toward human exploration, allowing an analysis of the potential resources as well as potential threats that may exist for human exploration of Mars (Beatty et al., 2019). Upon eventual return to Earth, these samples will be analyzed by a wide variety of techniques which will provide unprecedented new information about Mars.

## Appendix A

List of Members of the Regolith Working Group

Name	Affiliation
Candice C. Bedford	Purdue University
Jim Bell	Arizona State University
Kathleen C. Benison	West Virginia University
Eve L. Berger	NASA Johnson Space Center
Michael S. Bramble	NASA Jet Propulsion Laboratory
Adrian J. Brown	Plancius Research
John R. Brucato	INAF-Astrophysical Observatory of Arcetri
Fred J. Calef III	NASA Jet Propulsion Laboratory
Emily Cardarelli	University of California, Los Angeles
Nancy A. Carman	University of Nevada, Las Vegas
Titus M. Casademont	University of Oslo
David Catling	University of Washington
Benton C. Clark	Space Science Institute
Edward Cloutis	University of Winnipeg
Agnes Cousin	Institut de Recherche en Astrophysique et Planétologie
Bethany L. Ehlmann	California Institute of Technology
Kenneth A. Farley	California Institute of Technology
David T. Flannery	Queensland University of Technology
Teresa Fornaro	Italian National Institute for Astrophysics
Matthew P. Golombek	NASA Jet Propulsion Laboratory
Felipe Gomez	Centro de Astrobiología (CAB), CSIC-INTA,
Yulia Goreva	NASA Jet Propulsion Laboratory
Samantha J. Gwizd	NASA Jet Propulsion Laboratory
Svein-Erik Hamran	University of Oslo
Elisabeth M. Hausrath	University of Nevada, Las Vegas
Michael H. Hecht	Massachusetts Institute of Technology
Briony H. Horgan	Purdue University
Joel Hurowitz	Stony Brook University
Elsa H. Jensen	Malin Space Science Systems
Jeff Johnson	Johns Hopkins University Applied Physics Laboratory
Rachel E. Kronyak	NASA Jet Propulsion Laboratory
Jeremie A. Lasue	Institut de Recherche en Astrophysique et Planétologie
Juan Manuel Madariaga	Department of Analytical Chemistry, University of the Basque Country UPV/EHU
Jesus Martinez Frias	Institute of Geosciences, IGEO (CSIC-UCM)
German Martinez	Lunar and Planetary Institute
Tim McConnochie	Space Science Institute
Michael T. Mellon	Cornell University
Pierre-Yves V. Meslin	Institut de Recherche en Astrophysique et Planétologie
Naomi Murdoch	ISAE-SUPAERO
Claire E. Newman	Aeolis Research
Daniel C. Nunes	NASA Jet Propulsion Laboratory
David A. Paige	University of California, Los Angeles

**Appendix A**  
*Continued*

Name	Affiliation
Iratxe Población	Department of Analytical Chemistry, University of the Basque Country UPV/EHU
Giovanni Poggiali	INAF—Astrophysical Observatory of Arcetri
Nicolas Randazzo	Department of Earth and Atmospheric Sciences, University of Alberta
Eleni M. Ravanis	University of Hawaii
Melissa Rice	Western Washington University
Mitch Schulte	NASA
Mark A. Sephton	Department of Earth Science & Engineering, Imperial College
Andrew Shumway	University of Washington
David L. Shuster	University of California, Berkeley
Sandra M. Siljestroem	RISE Research Institutes of Sweden
Robert J. Sullivan	Cornell University
Nicholas J. Tosca	Cambridge University
Scott J. VanBommel	Washington University in St. Louis
Paulo Vasconcelos	University of Queensland
Alicia Vaughan	Apogee Engineering
Roger Wiens	Purdue University
Nathan R. Williams	NASA Jet Propulsion Laboratory
Maria Paz Zorzano Mier	Centro de Astrobiología (CAB), CSIC-INTA

### Data Availability Statement

The data in this paper are from the Mars2020 instruments SuperCam, PIXL, SHERLOC, WATSON, Mastcam-Z, and MEDA. The SuperCam data include the Laser Induced Breakdown Spectroscopy (LIBS), Visible/near infrared (VISIR) Spectroscopy, and images from the Remote Microimager. The PIXL data include images, PIXL spectra and diffraction data, and oxide concentrations. The Mastcam-Z data include multispectral data, stereo images, and results of the 3-D processing documented in Paar et al. (2023). The MEDA data include images, ground temperature, and relative humidity. The SHERLOC data include spectra and ACI images, and the WATSON data includes images. The SuperCam Major-element Oxide Compositions (MOC), total emissivity, and all raw data and processed calibrated data files are present in the Planetary Data System (Wiens, Maurice, Deen, et al., 2021) (PDS). The SuperCam H scores are generated after Forni et al. (2013), and the retrieved H component used to generate the H scores after Forni et al. (2013) is included in Hausrath et al. (2023). The Cl scores are generated after Cousin et al. (2025), and the S scores after Meslin et al. (2022), and documented in those publications. The PIXL images, spectra, and oxides are documented in the PDS (Allwood & Hurowitz, 2021). The Mastcam-Z image and spectra data are available in the PDS (Bell et al., 2021). The MEDA data utilized in the manuscript are available in the PDS (Rodriguez-Manfredi and de la Torre Juarez, 2021). The SHERLOC and WATSON data are available in the PDS (Beegle et al., 2021). The Navcam images are available on the PDS (Maki, Deen, et al., 2020). The data from previous missions presented in Figure 2 are summarized in papers as described (Gellert, 2019) and the PDS for the Mars Exploration Rovers at the PDS Geosciences Node site: <https://>

pds-geosciences.wustl.edu/missions/mer/mer\_apxs\_oxide.htm. The SI for this document is available at E. M. Hausrath et al. (2024).

**Acknowledgments**

E. M. Hausrath, C. T. Adcock, and N. A. Carman acknowledge funding from NASA RSS PS Grant 80NSSC20K0239, R. Sullivan from Mars 2020 Phase E funding for Mastcam-Z and MEDA, M.-P. Zorzano was supported by Grant PID2022-1401800B-C21 funded by MCIN/AEI/10.13039/501100011033, S. Siljeström was supported by the Swedish National Space Agency (contracts 2021-00092 and 137/19), S. Sharma was supported by M2020 Phase E funding for SHERLOC and her research was carried out at the Jet Propulsion Laboratory, California Institute of Technology, under a contract with NASA (80NM0018D0004). S. J. VanBommel and A. Knight acknowledge funding from M2020 Participating Scientist Grant 80NSSC21K0328, G. Martinez acknowledges JPL funding from USRA Contract Number 1638782, A. Vicente-Retortillo is funded by MCIN/AEI/10.13039/501100011033/FEDER, UE. L. Mandon is funded by the Texaco Postdoctoral fellowship awarded by the division of Geological and Planetary Sciences of Caltech, J. M. Madariaga and I. Poblacion acknowledge funding from the Spanish Agency for Research, Contract PID2022-1427500B-I00, funded by MCIN/AEI/10.13039/501100011033, J. R. Johnson acknowledges funding from JPL subcontract 1532432, ASU subcontract 15-707 (1511125), J. Lasue acknowledges CNES funding (French Space Agency), E. Cardarelli acknowledges funding from M2020 Phase E funding for SHERLOC, A. Udry acknowledges funding from NASA Mars 2020 Participating Scientist program 80NSSC21K0330, R. Wiens, and C.C. Bedford acknowledge funding from NASA Mars 2020 SuperCam contract NNH13ZDA0180, K. Benison acknowledges funding from NASA M2020 Returned Sample Scientist Participating Scientist Grant 80NSSC20K0235, T. Bosak acknowledges funding from M2020 Returned Sample Scientist Participating Scientist Grant 80NSSC20K0234, A. Czaja was supported by the Mars 2020 Returned Sample Science Participating Scientist Program (NASA award number 80NSSC20K0237), B. Weiss thanks the Mars 2020 Participating Scientist program (Grant 80NSSC20K0238) for funding, B. C. Clark and A. O. Shumway acknowledge funding from M2020 Phase E funding for PIXL, C. D. K. Herd acknowledges funding from M2020 Returned Sample Scientist Participating Scientist Grant CSA20EXPMARS, K.E. Herkenhoff acknowledges funding from M2020 Phase E funding for Mastcam-Z, R. S. Jakubek acknowledges funding from Advanced Curation, NASA Astromaterials Acquisition and Curation Office, Johnson Space Center, L. Jandura acknowledges

**References**

Allwood, A. C., & Hurowitz, J. A. (2021). Mars 2020 perseverance rover PIXL raw and derived data products. <https://doi.org/10.17189/1522645>

Allwood, A. C., Wade, L. A., Foote, M. C., Elam, W. T., Hurowitz, J. A., Battel, S., et al. (2020). PIXL: Planetary instrument for X-ray litho-chemistry. *Space Science Reviews*, 216(8), 134. <https://doi.org/10.1007/s11214-020-00767-7>

Anderson, S. P., Dietrich, W. E., & Brimhall, G. H. (2002). Weathering profiles, mass balance analysis, and rates of solute loss: Linkages between weathering and erosion in a small, steep catchment. *Geological Society of America Bulletin*, 114(9), 1143–1158. [https://doi.org/10.1130/0016-7606\(2002\)114<1143:wpmbaa>2.0.co;2](https://doi.org/10.1130/0016-7606(2002)114<1143:wpmbaa>2.0.co;2)

Apestigue, V., Alejandro Gonzalo, J. J., Boland, J., Lemmon, M., de Mingo, J. R., Garcia-Menendez, E., et al. (2022). Radiation and dust sensor for Mars environmental dynamic analyzer onboard M2020 rover. *Sensors*, 22(8), 2907. <https://doi.org/10.3390/s22082907>

Arvidson, R. E., Anderson, R. C., Bartlett, P., Bell, J. F., III, Blaney, D., Christensen, P. R., et al. (2004). Localization and physical properties experiments conducted by Spirit at Gusev crater. *Science*, 305(5685), 821–824. <https://doi.org/10.1126/science.1099922>

Arvidson, R. E., Anderson, R. C., Bartlett, P., Bell, J. F., III, Christensen, P. R., Chu, P., et al. (2004). Localization and physical properties experiments conducted by opportunity at Meridiani Planum. *Science*, 306(5702), 1730–1733. <https://doi.org/10.1126/science.1104211>

Arvidson, R. E., Bell, J. F., III, Belluta, P., Cabrol, N. A., Catalano, J. G., Cohen, J., et al. (2010). Spirit Mars rover mission: Overview and selected results from the northern home plate Winter haven to the side of Scamander crater. *Journal of Geophysical Research*, 115(E7), E00F03. <https://doi.org/10.1029/2010JE003633>

Arvidson, R. E., Bonitz, R. G., Robinson, M. L., Carsten, J. L., Volpe, R. A., Trebi-Ollennu, A., et al. (2009). Results from the Mars Phoenix lander robotic arm experiment. *Journal of Geophysical Research*, 114(E1), E00E02. <https://doi.org/10.1029/2009JE003408>

Arvidson, R. E., Poulet, F., Morris, R. V., Bibring, J.-P., Bell, J. F., III, Squyres, S. W., et al. (2006). Nature and origin of the hematite-bearing plains of Terra Meridiani based on analyses of orbital and Mars Exploration rover data sets. *Journal of Geophysical Research*, 111(E12), E12S08. <https://doi.org/10.1029/2006JE002728>

Arvidson, R. E., Squyres, S. W., Anderson, R. C., Bell, J. F., III, Blaney, D., Brückner, J., et al. (2006). Overview of the Spirit Mars exploration rover mission to Gusev crater: Landing site to Backstay rock in the Columbia Hills. *Journal of Geophysical Research*, 111(E2), E02S0. <https://doi.org/10.1029/2005JE002499>

Babechuk, M. G., Widdowson, M., & Kamber, B. S. (2014). Quantifying chemical weathering intensity and trace element release from two contrasting basalt profiles, Deccan Traps, India. *Chemical Geology*, 363, 56–75. <https://doi.org/10.1016/j.chemgeo.2013.10.027>

Bagnold, R. (1941). *The Physics of Blown Sand and Desert Dunes*. Methuen. subsequently reprinted by others (e.g., 1973 by Chapman & Hall, 2005 by Dover) (p. 265).

Beatty, D. W., Grady, M. M., McSween, H. Y., Sefton-Nash, E., Carrier, B. L., Altieri, F., et al. (2019). The potential science and engineering value of samples delivered to Earth by Mars sample return. *Meteoritics & Planetary Science*, 54(S1), S3–S152. <https://doi.org/10.1111/maps.13242>

Bedford, C. C., Banham, S. G., Bridges, J. G., Forni, O., Cousin, A., Bowden, D., et al. (2022). An insight into ancient aeolian processes and post-Noachian aqueous alteration in Gale crater, Mars, using ChemCam geochemical data from the Greenhough Capping Unit. *Journal of Geophysical Research: Planets*, 127(9), e2021E007100. <https://doi.org/10.1029/2021JE007100>

Bedford, C. C., Schwenzer, S. P., Bridges, J. C., Banham, S., Wiens, R. C., Gasnault, O., et al. (2020). Geochemical variation in the Stimson formation of Gale crater: Provenance, mineral sorting, and a comparison with modern Martian dunes. *Icarus*, 341, 113622. <https://doi.org/10.1016/j.icarus.2020.113622>

Beegle, L. W., Bhartia, R., Deen, R. G., Padgett, D., Algermissen, S., Dunn, A. E., et al. (2021). Mars 202 Perseverance rover SHERLOC raw, partially processed and derived data products. <https://doi.org/10.17189/1522643>

Bell, J. F., Maki, J. N., Mehall, G. L., Ravine, M. A., Caplinger, M. A., Bailey, Z. J., et al. (2021). The Mars 2020 Perseverance rover mast camera Zoom (Mastcam-Z) multispectral, stereoscopic imaging investigation. *Space Science Reviews*, 217(24), 24. <https://doi.org/10.1007/s11214-020-00755-x>

Berger, J. A., Schmidt, M. E., Gellert, R., Boyd, N. I., Desouza, E. D., Flemming, R. L., et al. (2017). Zinc and germanium in the sedimentary rocks of Gale crater on Mars indicate hydrothermal enrichment followed by diagenetic fractionation. *Journal of Geophysical Research: Planets*, 122(8), 1747–1772. <https://doi.org/10.1002/2017JE005290>

Berger, J. A., Schmidt, M. E., Gellert, R., Campbell, J. L., King, P. L., Flemming, R. L., et al. (2016). A global Mars dust composition refined by the Alpha-Particle X-ray Spectrometer in Gale Crater. *Geophysical Research Letters*, 43(1), 67–75. <https://doi.org/10.1002/2015GL066675>

Bhartia, R., Beegle, L. W., DeFlores, L., Abbey, W., Razzell Horris, J., Uckert, K., et al. (2021). Perseverance’s Scanning habitable environments with Raman and Luminescence for organics and chemicals (SHERLOC) investigation. *Space Science Reviews*, 217(58), 58. <https://doi.org/10.1007/s11214-021-00812-z>

Blair, T. C., & McPherson, J. G. (1994). Alluvial fans and their natural distinction from rivers based on morphology, hydraulic processes, sedimentary processes, and facies assemblages. *Journal of Sedimentary Research*, 64(3a), 450–489.

Blake, D. F., Morris, R. V., Kocurek, G., Morrison, S. M., Downs, R. T., Bish, D., et al. (2013). Curiosity at Gale crater, Mars: Characterization and analysis of the Rocknest sand shadow. *Science*, 341(6153), 1239505. <https://doi.org/10.1126/science.1239505>

Bosak, T., Shuster, D. L., Scheller, E. L., Siljeström, S., Zawaski, M. J., Mandon, L., et al. (2024). Astrobiological potential of rocks acquired by the Perseverance rover at a sedimentary fan front in Jezero crater, Mars. *AGU Advances*, 5(4), e2024AV001241. <https://doi.org/10.1029/2024AV001241>

Brimhall, G., & Dietrich, W. E. (1987). Constitutive mass balance relations between chemical composition, volume, density, porosity, and strain in metasomatic hydrochemical systems: Results on weathering and pedogenesis. *Geochimica et Cosmochimica Acta*, 51(3), 567–587. [https://doi.org/10.1016/0016-7037\(87\)90070-6](https://doi.org/10.1016/0016-7037(87)90070-6)

Bristow, C. S., & Moller, T. H. (2018). Dust production by abrasion of eolian basalt sands: Analogue for Martian dust. *Journal of Geophysical Research: Planets*, 123(10), 2713–2731. <https://doi.org/10.1029/2018JE005682>

Cabrol, N. A., Herkenhoff, K., Knoll, A. H., Farmer, J., Arvidson, R., Grin, E., et al. (2014). Sands at Gusev crater, Mars. *Journal of Geophysical Research: Planets*, 119(5), 941–967. <https://doi.org/10.1002/2013JE004535>

Cantor, B. A. (2007). MOC observations of the 2001 Mars planet-encircling dust storm. *Icarus*, 186(1), 60–96. <https://doi.org/10.1016/j.icarus.2006.08.019>

Carr, M. H., & Head, J. W. (2010). Geologic history of Mars. *Earth and Planetary Science Letters*, 294(3–4), 185–203. <https://doi.org/10.1016/j.epsl.2009.06.042>

funding from M2020 Phase E funding for Strategic Sampling. J. Martínez-Frias acknowledges funding from the Spanish Agency for Research, Contract PID2022-1427500B-I00, L. E. Mayhew acknowledges funding from the M2020 Return Sample Science Participating Scientist Grant 80NSSC20K0240, S. K. Sharma is supported by a subcontract from JPL to participate as a co-PI of the SuperCam Instrument, J. Simon acknowledges funding from M2020 Return Sample Science Participating Scientist supported by NASA Mars Exploration Program, I. Tirona acknowledges funding from M2020 Phase E funding for Robotic Operations—Tactical Sampling, A. Williams acknowledges funding from NASA M2020 Participating Scientist Program, Grant 80NSSC21K0332, F. Gómez acknowledges funding from INTA internal project DAXE (S.IGS22001), M. A. Sephton was supported by UK Space Agency Grant V006134/1, Alicia Vaughan acknowledges funding through NASA Agreement 80HQTR20T0096, T. Fornaro acknowledges funding from ASI/INAF agreement no. 2023-3-HH, Mini Grant Ricerca Fondamentale INAF 2022, E. Cloutis acknowledges funding from NSERC (RGPIN-2023-04582) and the Canadian Space Agency (22EXPCO14), WATSON and ACI images are acquired and focus merges processed by Malin Space Science Systems. We would like to thank the Mars2020 Science and Engineering teams for their work supporting the mission that has enabled the scientific research presented in this manuscript, and thank reviewer Michael Thorpe, R. Aileen Yingst, Editor Deanne Rogers, and one anonymous reviewer whose careful and insightful reviews greatly improved this work.

- Christensen, P. R., & Moore, H. J. (1992). The Martian surface layer. In H. H. Kieffer (Ed.), *University of Arizona press, space science Series. Mars* (pp. 686–727).
- Clark, B. C., Baird, A. K., Weldon, R. J., Tsusaki, D. M., Schnabel, L., & Candelariam, P. (1982). Chemical composition of Martian fines. *Journal of Geophysical Research*, 87(B12), 10059–10067. <https://doi.org/10.1029/JB087B12p10059>
- Corpolongo, A., Jakubek, R. S., Burton, A. S., Brown, A. J., Yanchilina, A., Czaja, A. D., et al. (2023). SHERLOC Raman mineral class detections of the Mars 2020 Crater Floor Campaign. *Journal of Geophysical Research: Planets*, 128(3), e2022JE007455. <https://doi.org/10.1029/2022JE007455>
- Cousin, A., Meslin, P. Y., Forni, O., Beyssac, O., Clavé, E., Hausrath, E., et al. (2025). Soil diversity at Jezero crater and comparison to Gale crater, Mars. *Icarus*, 425, 116299. <https://doi.org/10.1016/j.icarus.2024.116299>
- Czaja, A. D., Zorzano, M.-P., Kminek, G., Meyer, M. A., Beaty, D. W., Sefton-Nash, E., et al. (2023). Report of the science Community Workshop on the proposed first sample depot for the Mars sample return campaign. *Meteoritics & Planetary Science*, 58(6), 885–896. <https://doi.org/10.1111/maps.13981>
- David, G., Meslin, P.-Y., Dehouck, E., Gasnault, O., Cousin, A., Forni, O., et al. (2021). Laser-induced Breakdown spectroscopy (LIBS) characterization of granular soils: Implications for ChemCam analyses at Gale crater, Mars. *Icarus*, 365, 114481. <https://doi.org/10.1016/j.icarus.2021.114481>
- Dehouck, E., Forni, O., Quantin-Nataf, C., Beck, P., Mangold, N., Royer, C., et al. (2023). Overview of the bedrock geochemistry and mineralogy observed by SuperCam during Perseverance's Delta front campaign. In *54th lunar and planetary conference, abstract #2862*.
- Edgett, K. S., & Christensen, P. R. (1994). Mars aeolian sand: Regional variations among dark-hued crater floor features. *Journal of Geophysical Research*, 99(E1), 1997–2018. <https://doi.org/10.1029/93JE03094>
- Eigenbrode, J. L., Summons, R. E., Steele, A., Freissinet, C., Millan, M., Navarro-Gonzalez, R., et al. (2018). Organic matter preserved in 3-billion-year-old mudstones at Gale crater, Mars. *Science*, 360(6393), 1096–1101. <https://doi.org/10.1126/science.aas9185>
- Farley, K. A., & Stack, K. M. (2023a). Mars 2020 initial reports—Volume 1 crater floor campaign. <https://doi.org/10.17189/68tf-re13>
- Farley, K. A., & Stack, K. M. (2023b). Mars 2020 initial reports—Volume 2 delta front campaign. <https://doi.org/10.17189/49zd-2k55>
- Farley, K. A., & Stack, K. M. (2023c). *Mars 2020 sample Dossier Bundle*. NASA Planetary Data System. <https://doi.org/10.17189/1E55-M884>
- Farley, K. A., Williford, K. H., Stack, K. M., Bhartiya, R., Chen, A., de la Torre, M., et al. (2020). Mars 2020 mission overview. *Space Science Reviews*, 216(142), 142. <https://doi.org/10.1007/s11214-020-00762-y>
- Folk, R. L., & Ward, W. C. (1957). Brazos River bar: A study in the significance of grain size parameters. *Journal of Sedimentary Research*, 27(1), 3–26. <https://doi.org/10.1306/74D70646-2B21-11D7-8648000102C1865D>
- Forget, F., & Montabone, L. (2017). Atmospheric dust on Mars: A review. In *47th international conference environmental systems, 2017-07-16*. Retrieved from [https://tlu-ir.tdl.org/bitstream/handle/2346/72982/ICES\\_2017\\_175.pdf](https://tlu-ir.tdl.org/bitstream/handle/2346/72982/ICES_2017_175.pdf)
- Forni, O., Maurice, S., Gasnault, O., Wiens, R. C., Cousin, A., Clegg, S. M., et al. (2013). Independent component analysis classification of Laser-Induced Breakdown Spectroscopy spectra. *Spectrochimica Acta B: Atomic Spectroscopy*, 86, 31–41. <https://doi.org/10.1016/j.sab.2013.05.003>
- Fryberger, S. G., Hesp, P., & Hastings, K. (1992). Aeolian granule ripple deposits, Namibia. *Sedimentology*, 39(2), 319–331. <https://doi.org/10.1111/j.1365-3091.1992.tb01041.x>
- Gaft, M., Reisfeld, R., & Panczer, G. (2015). *Modern Luminescence of minerals and materials*. Springer Mineralogy. <https://doi.org/10.1007/978-3-319-24765-6>
- Gary, M., McAfee, R., & Wolf, C. L. (Eds.) (1972). *Glossary of geology* (pp. 293–294). American Geological Institute.
- Gellert, R. (2019). *MER APXS derived oxide data Bundle*. NASA Planetary System. <https://doi.org/10.17189/1518973>
- Gellert, R., Campbell, J. L., King, P. L., Leshin, L. A., Lugmair, G. W., Spray, J. G., et al. (2009). The Alpha-Particle-X-ray-Spectrometer (APXS) for the Mars Science Laboratory (MSL) rover mission. In *40th lunar and planetary science conference, abstract #2364*. Retrieved from <https://www.lpi.usra.edu/meetings/lpsc2009/pdf/2364.pdf>
- Gellert, R., Rieder, R., Brückner, J., Clark, B. C., Dreibus, G., Klingelhöfer, G., et al. (2006). Alpha particle X-ray spectrometer (APXS): Results from Gusev crater and calibration report. *Journal of Geophysical Research*, 111(E2), E02S05. <https://doi.org/10.1029/2005JE002555>
- Golombek, M. P., Haldemann, A. F. C., Simpson, R. A., Ferguson, R. L., Putzig, N. E., Arvidson, R. E., et al. (2008). Martian surface properties from joint analysis of orbital, Earth-based, and surface observations. In J. Bell (Ed.), *The Martian surface: Composition, mineralogy and physical properties, Cambridge planetary science* (pp. 468–498). Cambridge University Press.
- Grady, M. M., Summons, R. E., Swindle, T. D., Westall, F., Kminek, G., Meyer, M. A., et al. (2022). The scientific importance of returning airfall dust as part of Mars sample return (MSR). *Astrobiology*, S176–S185. <https://doi.org/10.1089/ast.2021.0111>
- Greeley, R., Arvidson, R., Bell, J. F., III, Christensen, P., Foley, D., Haldemann, A., et al. (2005). Martian variable features: New insight from the Mars express orbiter and the Mars exploration rover Spirit. *Journal of Geophysical Research*, 110(E6), E06002. <https://doi.org/10.1029/2005je002403>
- Greeley, R., Leach, R., White, B., Iversen, J., & Pollack, J. (1980). Threshold windspeeds for sand on Mars: Wind tunnel simulations. *Geophysical Research Letters*, 7(2), 121–124. <https://doi.org/10.1029/GL007i002p00121>
- Guzewich, S. D., Lemmon, M., Smith, C. L., Martínez, G., de Vicente-Retortillo, Á., Newman, C. E., et al. (2019). Mars Science Laboratory observations of the 2018/Mars year 34 global dust storm. *Geophysical Research Letters*, 46(1), 71–79. <https://doi.org/10.1029/2018GL080839>
- Haberle, R. M., Murphy, J. R., & Schaeffer, J. (2003). Orbital change experiments with a Mars general circulation model. *Icarus*, 161(1), 66–89. [https://doi.org/10.1016/S0019-1035\(02\)00017-9](https://doi.org/10.1016/S0019-1035(02)00017-9)
- Hausrath, E. M., Adcock, C. T., Bechtold, A., Beck, P., Benison, K., Brown, A., et al. (2023). An examination of soil crusts on the floor of Jezero Crater, Mars. *Journal of Geophysical Research: Planets*, 128(10), e2022JE007433. <https://doi.org/10.1029/2022JE007433>
- Hausrath, E. M., Sullivan, R., Goreva, Y., Zorzano, M. P., Vaughan, A., Cousin, A., et al. (2024). Collection and in situ analyses of regolith samples by the Mars 2020 rover: Implications for their formation and alteration history Supplementary Online Material [Dataset]. *Journal of Geophysical Research*. <https://doi.org/10.6084/m9.figshare.25302640>
- Hausrath, E. M., Ming, D. W., Peretyazhko, T. S., & Rampe, E. B. (2018). Reactive transport and mass balance modeling of the Stimson sedimentary formation and altered fractures zones constrain diagenetic conditions at Gale crater, Mars. *Earth and Planetary Science Letters*, 491, 1–10. <https://doi.org/10.1016/j.epsl.2018.02.037>
- Hausrath, E. M., Treiman, A. H., Vicenzi, E., Bish, D. L., Blake, D., Sarrazin, P., et al. (2008). Short- and long-term olivine weathering in Svalbard: Implications for Mars. *Astrobiology*, 8(6), 1079–1092. <https://doi.org/10.1089/ast.2007.0195>
- Hayes, A. G., Corlies, P., Tate, C., Barrington, M., Bell, J. F., Maki, J. N., et al. (2021). Pre-flight calibration of the Mars 2020 rover Mastcam Zoom (Mastcam-Z) multispectral, stereoscopic imager. *Space Science Reviews*, 217(2), 29. <https://doi.org/10.1007/s11214-021-00795-x>
- Herkenhoff, K. E., Golombek, M. P., Guinness, E. A., Johnson, J. B., Kusak, A., Richter, L., et al. (2008). In situ observations of the physical properties of the Martian surface. In J. Bell (Ed.), *The Martian surface, composition, Mineralogy and physical properties* (pp. 451–467). Cambridge University Press. <https://doi.org/10.1017/CBO9780511536076.021>

- Hurowitz, J. A., Tice, M. M., Allwood, A. C., Cable, M. L., Bosak, T., Broz, A., et al. (2023). The Petrogenetic history of the Jezero Crater Delta front from Microscale observations by the Mars 2020 PIXL instrument. In *Paper presented at the 54th lunar and planetary science conference, Houston*. Retrieved from <https://www.hou.usra.edu/meetings/lpsc2023/pdf/2301.pdf>
- Iversen, J. D., & White, B. R. (1982). Saltation threshold on Earth, Mars and Venus. *Sedimentology*, 29(1), 111–119. <https://doi.org/10.1111/j.1365-3091.1982.tb01713.x>
- Jerolmack, D. J., Mohrig, D., Grotzinger, J. P., Fike, D. A., & Watters, W. A. (2006). Spatial grain size sorting in eolian ripples and estimation of wind conditions on planetary surfaces: Application to Meridiani Planum, Mars. *Journal of Geophysical Research*, 111(E12), E12S02. <https://doi.org/10.1029/2005JE002544>
- Johnson, J. R., Bell, J. F., III, Cloutis, E., Staid, M., Farrand, W. H., McCoy, T., et al. (2007). Mineralogic constraints on sulfur-rich soils from Pancam spectra at Gusev crater, Mars. *Geophysical Research Letters*, 34(13), L13202. <https://doi.org/10.1029/2007GL029894>
- Kinch, K. M., Madsen, M. B., Bell, J. F., Maki, J. N., Bailey, Z. J., Hayes, A. G., et al. (2020). Radiometric calibration targets for the Mastcam-Z camera on the Mars 2020 rover mission. *Space Science Reviews*, 216(8), 141. <https://doi.org/10.1007/s11214-020-00774-8>
- Kuenen, P. H. (1960). Experimental abrasion 4: Eolian action. *The Journal of Geology*, 68(4), 427–449. <https://doi.org/10.1086/626675>
- Lämmel, M., Meiwald, A., Yizhaq, H., Tsoar, H., Katra, I., & Kroy, K. (2018). Aeolian sand sorting and megaripple formation. *Nature Physics*, 14(7), 759–765. <https://doi.org/10.1038/s41567-018-0106-z>
- Lasue, J., Cousin, A., Meslin, P.-Y., Mangold, N., Wiens, R. C., Berger, G., et al. (2018). Martian eolian dust probed by ChemCam. *Geophysical Research Letters*, 45(20), 10968–10977. <https://doi.org/10.1029/2018GL079210>
- Lasue, J., Meslin, P.-Y., Cousin, A., Forni, O., Anderson, R., Beyssac, O., et al. (2023). SuperCam first shots: Dust composition and variability. In *54th lunar and planetary science conference, abstract #2806*.
- Lemmon, M. T., Smith, M. D., Viudez-Moreiras, D., de la Torre-Jurez, M., Vicente-Retortillo, A., Munguira, A., et al. (2022). Dust, sand, and winds within an active Martian storm in Jezero crater. *Geophysical Research Letters*, 49(17), e2022GL100126. <https://doi.org/10.1029/2022GL100126>
- Maki, J. N., Deen, R. G., Algermissen, S., Dunn, A. E., Toole, N. T., Crombie, M. K., et al. (2020). Calibrated data products for the Mars 2020 perseverance rover cache camera. <https://doi.org/10.17189/47kr-ta40>
- Maki, J. N., Gruel, D., McKinney, C., Ravine, M. A., Morales, M., Lee, D., et al. (2020). The Mars 2020 engineering cameras and microphone on the perseverance rover: A next-generation imaging system for Mars exploration. *Space Science Reviews*, 216(8), 137. <https://doi.org/10.1007/s11214-020-00765-9>
- Mandon, L., Ehlmann, B. L., Wiens, R. C., Garczynski, B. J., Horgan, B. H. N., Fouchet, T., et al. (2024). Variable iron mineralogy and redox conditions recorded in ancient rocks measured by in situ visible/near-infrared spectroscopy at Jezero crater, Mars. *Journal of Geophysical Research: Planets*, 129(7), e2023JE008254. <https://doi.org/10.1029/2023JE008254>
- Mandon, L., Quantin-Nataf, C., Royer, C., Beck, P., Fouchet, T., Johnson, J. R., et al. (2023). Reflectance of Jezero crater floor: 2. Mineralogical interpretation. *Journal of Geophysical Research: Planets*, 128(7), e2022JE007450. <https://doi.org/10.1029/2022JE007450>
- Martin, N. D., Chide, B., Sheridan, A., Cousin, A., Hausrath, E., Beyssac, O., et al. (2023). Acoustics and LIBS profiling of soils at Jezero Crater, Mars. In *Paper presented at the 54th lunar and planetary science conference, Houston*. Retrieved from <https://www.hou.usra.edu/meetings/lpsc2023/pdf/1521.pdf>
- Martínez, G. M., Newman, C. N., De Vicente-Retortillo, A., Fischer, E., Renno, N. O., Richardson, M. I., et al. (2017). The modern near-surface Martian climate: A review of in-situ meteorological data from Viking to Curiosity. *Space Science Reviews*, 212(1–2), 295–338. <https://doi.org/10.1007/s11214-017-0360-x>
- Martínez, G. M., Sebastian, E., Vicente-Retortillo, A., Smith, M. D., Johnson, J. R., Fischer, E., et al. (2023). Surface energy budget, albedo and thermal inertia at Jezero Crater, Mars, as observed from the Mars 2020 MEDA instrument. *Journal of Geophysical Research: Planets*, 128(2), e2022JE007537. <https://doi.org/10.1029/2022JE007537>
- Maurice, S., Wiens, R., Bernardi, P., Cais, P., Robinson, S., Nelson, T., et al. (2021). The SuperCam instrument suite on the Mars 2020 rover: Science objectives and mast-unit description. *Space Science Reviews*, 217, 1–108. <https://doi.org/10.1007/s11214-021-00807>
- McLennan, S. M., Sephton, M. A., Beaty, D., Hecht, M., Pepin, B., Leya, I., et al. (2012). Planning for Mars returned sample science: Final report of the MSR end-to-end international science analysis group (E2E-ISAG): A report requested by the Mars exploration program analysis group (MEPAG). *Astrobiology*, 12, 175–230. <https://doi.org/10.1089/ast.2011.0805>
- Mellon, M. T., Ferguson, R. L., & Pubzig, N. E. (2008). The thermal inertia of the surface of Mars. In J. F. Bell (Ed.), *The thermal inertia of the surface of Mars, in the Martian surface: Composition, mineralogy, and physical properties*. Cambridge University Press. Retrieved from <https://www.cambridge.org/core/books/martian-surface/thermal-inertia-of-the-surface-of-mars/683F86021F4BB3790DD78C4C2513DF45>
- Mellon, M. T., McKay, C. P., & Grant, J. A. (2022). Thermal conductivity of planetary regoliths: The effects of grain-size distribution. *Icarus*, 387, 115211. <https://doi.org/10.1016/j.icarus.2022.115211>
- Merusi, M., Kinch, K. B., Madsen, M. B., Bell, J. F., Maki, J. N., Hayes, A. G., et al. (2022). The Mastcam-Z radiometric calibration targets on NASA's Perseverance rover: Derived irradiance time-series, dust deposition, and performance over the first 350 sols on Mars. *Earth and Space Science*, 9(12), e2022EA002552. <https://doi.org/10.1029/2022EA002552>
- Meslin, P.-Y., Forni, O., Beck, P., Cousin, A., Beyssac, O., Lopez-Reyes, G., et al. (2022). Evidence for perchlorate and sulfate salts in Jezero Crater, Mars, from Supercam observations. In *Paper presented at the 53rd lunar and planetary science conference, Houston*. Retrieved from <https://www.hou.usra.edu/meetings/lpsc2022/pdf/2694.pdf>
- Meslin, P.-Y., Gasnault, O., Forni, O., Schroder, S., Cousin, A., Berger, G., et al. (2013). Soil diversity and hydration as observed by ChemCam at Gale crater, Mars. *Science*, 341(6153), 1238670. <https://doi.org/10.1126/science.1238670>
- Ming, D. W., Mittlefehldt, D. W., Morris, R. V., Golden, D. C., Gellert, R., Yen, A., et al. (2006). Geochemical and mineralogical indicators for aqueous processes in the Columbia Hills of Gusev crater, Mars. *Journal of Geophysical Research*, 111(E2), E02S12. <https://doi.org/10.1029/2005JE002560>
- Minitti, M. E., Kah, L. C., Yingst, R. A., Edgett, K. S., Anderson, R. C., Beegle, L. W., et al. (2013). MAHLI at the Rocknest sand shadow: Science and science-enabling activities. *Journal of Geophysical Research: Planets*, 118(11), 2338–2360. <https://doi.org/10.1002/2013je004426>
- Moeller, R. C., Jandura, L., Rosette, K., Robinson, M., Samuels, J., Silverman, M., et al. (2021). The sampling and caching subsystem (SCS) for the scientific exploration of Jezero Crater by the Mars 2020 Perseverance rover. *Space Science Reviews*, 217(1), 5. <https://doi.org/10.1007/s11214-020-00783-7>
- Moore, H. J., Hutton, R. E., Clow, G. D., & Spitzer, C. R. (1987). Physical properties of the surface materials at the Viking landing sites on Mars. In *U. S. Geological Survey Professional paper 1389* (p. 222). U. S. Government Printing Office. <https://doi.org/10.3133/pp1389>
- Mustard, J. F., Adler, M., Allwood, A., Bass, D., Beaty, D., Bell, J. F., et al. (2013). Report of the Mars 2020 science definition team. Retrieved from [https://mepag.jpl.nasa.gov/reports/MEP/Mars\\_2020\\_SDT\\_Report\\_Final.pdf](https://mepag.jpl.nasa.gov/reports/MEP/Mars_2020_SDT_Report_Final.pdf)



- Neakrase, L. D. V., Balme, M. R., Esposito, F., Keling, T., Klose, M., Kok, J. F., et al. (2016). Particle lifting processes in dust devils. *Space Science Reviews*, 203(1–4), 347–376. <https://doi.org/10.1007/s11214-016-0296-6>
- Newman, C. E., Hueso, R., Lemmon, M. T., Munguira, A., Vicente-Retortillo, A., Apestigue, V., et al. (2022). The dynamic atmospheric and aeolian environment of Jezero crater, Mars. *Science Advances*, 8(21), eabn3783. <https://doi.org/10.1126/sciadv.abn3783>
- NRC (National Research Council). (2011). *Visions & Voyages for planetary science in the decade 2013–2022*. National Academies Press. <https://doi.org/10.17226/13117>
- O'Connell-Cooper, C. D., Spray, J. G., Thompson, L. M., Gellert, R., Berger, J. A., Boyd, N. I., et al. (2017). APXS-derived chemistry of the Bagnold dune sands: Comparisons with Gale Crater soils and the global Martian average. *Journal of Geophysical Research: Planets*, 122(12), 2623–2643. <https://doi.org/10.1002/2017JE005268>
- Paar, G., Ortner, T., Tate, C., Deen, R. G., Abercrombie, P., Vona, M., et al. (2023). Three-dimensional data preparation and immersive mission-spanning visualization and analysis of Mars 2020 Mastcam-Z stereo image sequences. *Earth and Space Science*, 10(3), e2022EA002532. <https://doi.org/10.1029/2022EA002532>
- Peters, G. H., Abbey, W., Bearman, G. H., Mungas, G. S., Smith, J. A., Anderson, R. C., et al. (2008). Mojave Mars simulant—Characterization of a new geologic Mars analog. *Icarus*, 197(2), 470–479. <https://doi.org/10.1016/j.icarus.2008.05.004>
- Phua, Y. Y., Ehlmann, B. L., Siljeström, S., Czaja, A. D., Bhartia, R., Minitti, M. E., et al. (2023). Sulfates as hydration carrier phases in altered rocks of Jezero crater fan and floor geologic units from SHERLOC on Mars 2020. AGU23.
- Polkko, J., Hieta, A.-M., Tamppari, L., Martinez, G., Viudez-Moreiras, D., Savijarvi, H., et al. (2023). Initial results of the relative humidity observations by MEDA instrument onboard the Mars 2020 Perseverance Rover. *Journal of Geophysical Research: Planets*, 128(2), e2022JE007447. <https://doi.org/10.1029/2022JE007447>
- Poulet, F., Mangold, N., Platevoet, B., Bardintzeff, J.-M., Sautter, V., Mustard, J. F., et al. (2009). Quantitative compositional analysis of Martian mafic regions using the MEX/OMEGA reflectance data: 2. Petrological implications. *Icarus*, 201(1), 84–101. <https://doi.org/10.1016/j.icarus.2008.12.042>
- Powers, M. C. (1953). A new roundness scale for sedimentary particles. *Journal of Sedimentary Petrology*, 23, 117–119.
- Presley, M. A., & Christensen, P. R. (1997). Thermal conductivity measurements of particulate materials 1. A review. *Journal of Geophysical Research*, 102(E3), 6535–6549. <https://doi.org/10.1029/96JE03302>
- Razzell Hollis, J., Sharma, S., Abbey, W., Bhartia, R., Beegle, L. W., Fries, M., et al. (2023). A deep-ultraviolet Raman and fluorescence spectral library of 51 organic compounds for the SHERLOC instrument onboard Mars 2020. *Astrobiology*, 23, 1–23. <https://doi.org/10.1089/ast.2022.0023>
- Read, P. L., Lewis, S. R., & Mulholland, D. P. (2015). The Physics of Martian weather and climate: A review. *Reports on Progress in Physics*, 78(12), 125901. <https://doi.org/10.1088/0034-4885/78/12/125901>
- Reiss, D., Raack, J., Rossi, A. P., Di Achille, G., & Hiesinger, H. (2010). First in-situ analysis of dust devil tracks on Earth and their comparison with tracks on Mars. *Geophysical Research Letters*, 37(14). <https://doi.org/10.1029/2010gl044016>
- Rivera-Valentín, E. G., Martinez, G., Filiberto, J., Lynch, K., Chevrier, V. F., Gough, R. V., et al. (2021). Resolving the water cycle on a salty Mars: Planetary science and astrobiology exploration strategies for the next decade. In *Planetary Science and Astrobiology Decadal Survey 2023-2032* (Vol. 53, p. 4). <https://doi.org/10.3847/25c2cfcb.b0e3963b>
- Rodríguez-Manfredi, J. A., & de la Torre Juárez, M. (2021). Mars 2020 Perseverance rover Mars environmental dynamics analyzer (MEDA) experiment data record (EDR) and reduced data record (RDR) data products Archive Bundle. PDS Atmospheres Node. <https://doi.org/10.17189/1522849>
- Rodríguez-Manfredi, J. A., de la Torre Juárez, M., Alonso, A., Apestegue, V., Arruogo, I., Atienza, T., et al. (2021). The Mars environmental dynamics analyzer, MEDA. A suite of environmental sensors for the Mars 2020 mission. *Space Science Reviews*, 217(3), 48. <https://doi.org/10.1007/s11214-021-00816-9>
- Roppel, R. D., Abbey, W. J., Asher, S. A., Bhartia, R., Bykov, S. V., Conrad, P., et al. (2023). Investigation of mineralogies during the delta front campaign by SHERLOC. In *54th lunar and planetary science conference, abstract #2761*. Lunar and Planetary Institute.
- Royer, C., Fouchet, T., Mandon, L., Montmessin, F., Poulet, F., Forni, O., et al. (2023). Reflectance of Jezero crater floor: 1. Data processing and calibration of the infrared spectrometer (IRS) on SuperCam. *Journal of Geophysical Research: Planets*, 128, e2022JE007481. <https://doi.org/10.1029/2022JE007481>
- Sak, P. B., Fisher, D. M., Gardner, T. W., Murphy, K., & Brantley, S. L. (2004). Rates of weathering rind formation on Costa Rican basalt. *Geochimica et Cosmochimica Acta*, 68(7), 1453–1472. <https://doi.org/10.1016/j.gca.2003.09.007>
- Sak, P. B., Navarre-Sitchler, A. K., Miller, C. E., Daniel, C. C., Gaillardet, J., Buss, H. L., et al. (2010). Controls on rind thickness on basaltic andesite clasts weathering in Guadeloupe. *Chemical Geology*, 276(3–4), 129–143. <https://doi.org/10.1016/j.chemgeo.2010.05.002>
- Scheller, E. L., Bosak, T., Weiss, B. P., McCubbin, F., Jakubek, R. S., Bykov, S., et al. (2023). Investigating the origin of luminescent materials in the crater floor and delta of Jezero crater, Mars. AGU23.
- Scheller, E. L., Razzell Hollis, J., Cardarelli, E. L., Steele, A., Beegle, L. W., Bhartia, R., et al. (2022). Aqueous alteration processes in Jezero crater, Mars—Implications for organic geochemistry. *Science*, 378(6624), 1105–1110. <https://doi.org/10.1126/science.abo5204>
- Schmitt-Kopplin, P., Matzka, M., Ruf, A., Menez, B., Chennaoui Aoudjehane, H., Harir, M., et al. (2023). Complex carbonaceous matter in Tissint Martian meteorites give insights into the diversity of organic geochemistry on Mars. *Science Advances*, 9(2), eadd6439. <https://doi.org/10.1126/sciadv.add6439>
- Sharma, S., Roppel, R. D., Murphy, A. E., Beegle, L. W., Bhartia, R., Steele, A., et al. (2023). Diverse organic-mineral associations in Jezero crater, Mars. *Nature*, 619(7971), 724–732. <https://doi.org/10.1038/s41586-023-06143-z>
- Sharp, R. P. (1963). Wind ripples. *The Journal of Geology*, 71(5), 617–636. <https://doi.org/10.1086/626936>
- Shkolyar, S., Lalla, E., Konstantindis, M., Cote, K., Daly, M. G., Steele, A., et al. (2021). Detecting Ce3+ as a biosignature mimicker using UV time-resolved laser-induced fluorescence and Raman spectroscopy: Implications for planetary missions. *Icarus*, 354, 114093. <https://doi.org/10.1016/j.icarus.2020.114093>
- Shumway, A. O., Kizovski, T. V., VanBommel, S. J., Catling, D. C., Tice, M. M., Tosca, N. J., et al. (2024). *Regolith Composition on the Jezero Delta Front Revealed with PIXL: Implications for Brine-Forming Salts*. LPI Contributions, 3007, 3386. <https://ui.adsabs.harvard.edu/abs/2024LPICo3007.3386S>
- Siljeström, S., Czaja, A. D., Corpolongo, A., Berger, E. L., Li, A. Y., Cardarelli, E., et al. (2024). Evidence of sulfate-rich fluid alteration in Jezero Crater Floor, Mars. *Journal of Geophysical Research: Planets*, 129(1), e2023JE007989. <https://doi.org/10.1029/2023JE007989>
- Silvestro, S., Chojnacki, M., Vaz, D. A., Cardinale, M., Yizhaq, H., & Esposito, F. (2020). Megaripple migration on Mars. *Journal of Geophysical Research: Planets*, 125(8), e2020JE006446. <https://doi.org/10.1029/2020JE006446>

- Simon, J. I., Hickman-Lewis, K., Cohen, B. A., Mayhew, L. E., Shuster, D. L., Debaille, V., et al. (2023). Samples collected from the floor of Jezero Crater with the Mars 2020 Perseverance rover. *Journal of Geophysical Research: Planets*, *128*(6), e2022JE007474. <https://doi.org/10.1029/2022JE007474>
- Soderblom, L. A., Anderson, R. C., Arvidson, R. E., Bell, J. F., III, Cabrol, N. A., Calvin, W., et al. (2004). Soils of Eagle crater and Meridiani Planum at the opportunity rover landing site. *Science*, *306*(5702), 1723–1726. <https://doi.org/10.1126/science.1105127>
- Stack, K. M., Ives, L. R. W., Gupta, S., Lamb, M. P., Tebolt, M., Caravaca, G., et al. (2024). Sedimentology and stratigraphy of the Shenandoah formation, Western fan, Jezero Crater, Mars. *Journal of Geophysical Research: Planets*, *129*(2), e2023JE008187. <https://doi.org/10.1029/2023JE008187>
- Steele, A., Benning, L. G., Wirth, R., Siljeström, S., Fries, M. D., Hauri, E., et al. (2018). Organic synthesis on Mars by electrochemical reduction of CO<sub>2</sub>. *Science Advances*, *4*(10), eaat5118. <https://doi.org/10.1126/sciadv.aat5118>
- Stein, N. T., Arvidson, R. E., O'Sullivan, J. A., Catalano, J. G., Guinness, E. A., Politte, D. V., et al. (2018). Retrieval of compositional end-members from Mars Exploration Rover Opportunity observations in a soil-filled fracture in Marathon Valley, Endeavour crater rim. *Journal of Geophysical Research: Planets*, *123*(1), 278–290. <https://doi.org/10.1002/2017JE005339>
- Sullivan, R., Anderson, R., Biesiadecki, J., Bond, T., & Stewart, H. (2011). Cohesions, friction angles, and other physical properties of Martian regolith from Mars Exploration Rover wheel trenches and wheel scuffs. *Journal of Geophysical Research*, *116*(E2), E02006. <https://doi.org/10.1029/2010JE003625>
- Sullivan, R., Arvidson, R., Bell, J. F., III, Gellert, R., Golombek, M., Greeley, R., et al. (2008). Wind-driven particle mobility on Mars: Insights from MER observations at “El Dorado” and surroundings at Gusev crater. *Journal of Geophysical Research*, *113*(E6), E06S07. <https://doi.org/10.1029/2008JE003101>
- Sullivan, R., Baker, M., Newman, C., Turner, M., Schieber, J., Weitz, C., et al. (2022). The aeolian environment of Glen Torridon, Gale crater, Mars. *Journal of Geophysical Research: Planets*, *127*(8), e2021JE007174. <https://doi.org/10.1029/2021JE007174>
- Sullivan, R., Banfield, D., Bell, J. F., III, Calvin, W., Fike, D., Golombek, M., et al. (2005). Aeolian processes at the Mars exploration rover Meridiani Planum landing site. *Nature*, *436*(7047), 58–61. <https://doi.org/10.1038/nature03641>
- Sullivan, R., & Kok, J. (2017). Aeolian saltation on Mars at low wind speeds. *Journal of Geophysical Research: Planets*, *122*(10), 2111–2143. <https://doi.org/10.1002/2017JE005275>
- Sullivan, R., Kok, J. F., Katra, I., & Yizhaq, H. (2020). A broad continuum of aeolian impact ripple morphologies on Mars is enabled by low wind dynamic pressures. *Journal of Geophysical Research: Planets*, *125*(10), e2020JE006485. <https://doi.org/10.1029/2020JE006485>
- Swann, C., Sherman, D. J., & Ewing, R. C. (2020). Experimentally-derived thresholds for windblown sand on Mars. *Geophysical Research Letters*, *47*(3), e2019GL084484. <https://doi.org/10.1029/2019GL084484>
- Taylor, G., & Eggleton, R. A. (2001). *Regolith geology and geomorphology* (p. 375). John Wiley & Sons Ltd.
- Taylor, S. R., & McLennan, S. (2009). *Planetary crusts: Their composition, origin and evolution* (p. 402). Cambridge University Press.
- Tice, M. M., Hurowitz, J. A., Allwood, A. C., Jones, M. W. M., Orenstein, B. J., Davidoff, S., et al. (2022). Alteration history of Seitah formation rocks inferred by PIXL X-ray fluorescence, X-ray diffraction, and multispectral imaging on Mars. *Science Advances*, *8*(47), eabp9084. <https://doi.org/10.1126/sciadv.abp9084>
- Uckert, K. (2022). Loupe. Retrieved from <https://github.com/nasa/Loupe>
- Vaughan, A., Miniti, M. E., Cardarelli, E. L., Johnson, J. R., Kah, L. C., Pilleri, P., et al. (2023). Regolith of the crater floor units, Jezero crater, Mars: Textures, composition, and implications for provenance. *Journal of Geophysical Research: Planets*, *128*(3), e2022JE007437. <https://doi.org/10.1029/2022JE007437>
- Vicente-Retortillo, A., Lemmon, M. T., Martinez, G. M., Toledo, D., Apéstigue, V., Arruego, I., et al. (2024). Dust accumulation and lifting at the landing site of the Mars 2020 mission, Jezero crater, as observed from MEDA. *Geophysical Research Letters*, *51*(11), e2023GL107975. <https://doi.org/10.1029/2023GL107975>
- Vicente-Retortillo, A., Martinez, G. M., Lemmon, M. T., Hueso, R., Johnson, J. R., Sullivan, R., et al. (2023). Dust lifting through surface albedo changes at Jezero Crater, Mars. *Journal of Geophysical Research: Planets*, *128*(4), e2022JE007672. <https://doi.org/10.1029/2022JE007672>
- Vicente-Retortillo, A., Martinez, G. M., Renno, N., Newman, C. E., Ordonez-Etxeberria, I., Lemmon, M. T., et al. (2018). Seasonal deposition and lifting of dust on Mars as observed by the Curiosity rover. *Scientific Reports*, *8*(1), 17576. <https://doi.org/10.1038/s41598-018-35946-8>
- Wang, A., Bell, J. F., III, Li, R., Johnson, J. R., Farrand, W. H., Cloutis, E. A., et al. (2008). Si-Rich species discovered by the Mars exploration rover Spirit in Columbia Hills. *Journal of Geophysical Research*, *113*(E12), E12S40. <https://doi.org/10.1029/2008JE003126>
- Wang, A., Haskin, L. A., Squyres, S. W., Jolliff, B. L., Crumpler, L., Gellert, R., et al. (2006). Sulfate deposition in subsurface regolith in Gusev crater, Mars. *Journal of Geophysical Research*, *111*(E2), E02S17. <https://doi.org/10.1029/2005JE002513>
- Weitz, C. M., Grant, J. A., Golombek, M. P., Warner, N. H., Hauber, E., Ansan, V., et al. (2020). Comparison of InSight Homestead hollow to hollows at the Spirit landing site. *Journal of Geophysical Research: Planets*, *125*(7), e2020JE006435. <https://doi.org/10.1029/2020JE006435>
- Weitz, C. M., O'Connell-Cooper, C., Thompson, L., Sullivan, R. J., Baker, M., & Grant, J. (2022). The physical properties and geochemistry of grains on aeolian bedforms at Gale crater, Mars. *Journal of Geophysical Research: Planets*, *127*(11), e2021JE007061. <https://doi.org/10.1029/2021JE007061>
- Weitz, C. M., Sullivan, R. J., Lapotre, M. G. A., Rowland, S. K., Grant, J. A., Baker, M., & Yingst, R. A. (2018). Sand grain sizes and shapes in Eolian Bedforms at Gale crater, Mars. *Geophysical Research Letters*, *45*(18), 9471–9479. <https://doi.org/10.1029/2018GL078972>
- Wentworth, U. K. (1922). A scale of grade and class terms for clastic sediments. *The Journal of Geology*, *30*(5), 377–392. <https://doi.org/10.1086/622910>
- Wiens, R. C., Maurice, S., Robinson, S. H., Nelson, A. E., Cais, P., Bernardi, P., et al. (2021). The SuperCam instrument suite on the NASA Mars 2020 rover: Body unit and combined system tests. *Space Science Reviews*, *217*(4), 4. <https://doi.org/10.1007/s11214-020-00777-5>
- Wiens, R. C., Maurice, S. A., Deen, R. G., Padgett, D., Algermissen, S., Dunn, A. E., et al. (2021). Mars 2020 perseverance rover SuperCam raw, calibrated, and derived data products. <https://doi.org/10.17189/1522646>
- Wolff, M. J., López-Valverde, M., Madeleine, J.-B., Wilson, R. J., Smith, M. D., Fouchet, T., & Delory, G. T. (2017). Radiative process: Techniques and applications. In R. M. Haberle, R. T. Clancy, F. Forget, M. D. Smith, & R. W. Zurek (Eds.), *The atmosphere and climate of Mars* (pp. 106–171). Cambridge University Press.
- Yen, A. S., Gellert, R., Schröder, C., Morris, R. V., Bell, J. F., III, Knudson, A. T., et al. (2005). An integrated view of the chemistry and mineralogy of Martian soils. *Nature*, *436*(7047), 49–54. <https://doi.org/10.1038/nature03637>
- Yen, A. S., Ming, D. W., Vaniman, D. T., Geller, R., Blake, D. F., Morris, R. V., et al. (2017). Multiple stages of aqueous alteration along fractures in mudstone and sandstone strata in Gale crater, Mars. *Earth and Planetary Science Letters*, *471*, 186–198. <https://doi.org/10.1016/j.epsl.2017.04.033>
- Yen, A. S., Morris, R. V., Clark, B. C., Gellert, R., Knudson, A. T., Squyres, S., et al. (2008). Hydrothermal processes at Gusev crater: An evaluation of Paso Robles class soils. *Journal of Geophysical Research*, *113*(E6), E06S10. <https://doi.org/10.1029/2007JE002978>

- Yesavage, T., Thomspon, A., Hausrath, E. M., & Brantley, S. L. (2015). Basalt weathering in an Arctic Mars-analog site. *Icarus*, *254*, 219–232. <https://doi.org/10.1016/j.icarus.2015.03.011>
- Zolotov, M., & Shock, E. (1999). Abiotic synthesis of polycyclic aromatic hydrocarbons on Mars. *Journal of Geophysical Research*, *104*(E6), 14033–14049. <https://doi.org/10.1029/1998JE000627>

## References From the Supporting Information

- Achilles, C. N., Downs, R. T., Ming, D. W., Rampe, E. B., Morris, R. V., Treiman, A. H., et al. (2017). Mineralogy of an active eolian sediment from the Namib dune, Gale crater, Mars. *Journal of Geophysical Research: Planets*, *122*(11), 2344–2361. <https://doi.org/10.1002/2017JE005262>
- Arvidson, R. E., Ashley, J. W., Bell, J. F., III, Chojnacki, M., Cohen, J., Economou, T. E., et al. (2011). Opportunity Mars rover mission: Overview and selected results from Purgatory ripple to traverses to Endeavour crater. *Journal of Geophysical Research*, *116*, E00F15. <https://doi.org/10.1029/2011JE003746>
- Arvidson, R. E., Morris, R. V., Ming, D. W., Crumpler, L. S., Yen, A. S., Squyres, S. W., et al. (2008). Spirit Mars rover mission to the Columbia Hills, Gusev crater: Mission overview and selected results from the Cumberland ridge to Home plate. *Journal of Geophysical Research*, *113*(E12), E12S33. <https://doi.org/10.1029/2008JE003183>
- Baird, A. K., Toulmin, P., III, Clark, B. C., Rose, H. J., Jr., Keil, K., Christian, R. P., & Gooding, J. L. (1976). Mineralogic and petrologic implications of Viking geochemical results from Mars: Interim results. *Science*, *194*(4271), 1288–1293. <https://doi.org/10.1126/science.194.4271.1288>
- Baumeister, J. L., Hausrath, E. M., Olsen, A., Tschauner, O., Adcock, C. T., & Metcalf, R. V. (2015). Biogeochemical weathering of serpentinites: An examination of incipient dissolution affecting serpentine soil formation. *Applied Geochemistry*, *54*, 74–84. <https://doi.org/10.1016/j.apgeochem.2015.01.002>
- Bish, D. L., Blake, D. F., Vaniman, D. T., Morris, R. V., Treiman, A. H., Sarrazin, P., et al. (2013). X-Ray diffraction results from Mars Science Laboratory: Mineralogy of Rocknest at Gale crater. *Science*, *341*(6153), 1238932. <https://doi.org/10.1126/science.1238932>
- Foley, C. N., Economou, T., & Clayton, R. N. (2003). Final chemical results from the Mars Pathfinder alpha proton X-ray spectrometer. *Journal of Geophysical Research*, *108*, 8096. <https://doi.org/10.1029/2002JE002019>
- Foley, C. N., Economou, T. E., Clayton, R. N., & Dietrich, W. (2003). Calibration of the Mars Pathfinder alpha proton X-ray spectrometer. *Journal of Geophysical Research*, *108*(E12), 8095. <https://doi.org/10.1029/2002JE002018>
- Bedford, C. (2019). *Distinguishing the geochemical effects of sedimentary processes and source region characteristics in Gale crater, Mars*. PhD thesis. The Open University.
- Bedford, C. C., Bridges, J. C., Schwenzer, S. P., Wiens, R. C., Rampe, E. B., Frydenvang, J., & Gasda, P. J. (2019). Alteration trends and geochemical source region characteristics preserved in the fluvio-lacustrine sedimentary record of Gale crater, Mars. *Geochimica et Cosmochimica Acta*, *246*, 234–266. <https://doi.org/10.1016/j.gca.2018.11.031>
- Borg, L., & Drake, M. J. (2005). A review of meteorite evidence for the timing of magmatism and of surface or near-surface liquid water on Mars. *Journal of Geophysical Research*, *110*(E12), E12S03. <https://doi.org/10.1029/2005JE002402>
- Bridges, N. T., & Ehlmann, B. L. (2018). The Mars Science Laboratory (MSL) Bagnold dunes campaign, phase I: Overview and introduction to the special issue. *Journal of Geophysical Research: Planets*, *123*(1), 3–19. <https://doi.org/10.1002/2017JE005401>
- Brückner, J., Dreibus, G., Rieder, R., & Wänke, H. (2003). Refined data of Alpha Proton X-ray Spectrometer analyses of soils and rocks at the Mars Pathfinder site: Implications for surface chemistry. *Journal of Geophysical Research*, *8094*(E12), 8094. <https://doi.org/10.1029/2003JE002060>
- Clark, B. C. (1993). Geochemical components in Martian soil. *Geochimica et Cosmochimica Acta*, *57*(19), 4575–4581. [https://doi.org/10.1016/0016-7037\(93\)90183-W](https://doi.org/10.1016/0016-7037(93)90183-W)
- Clark, B. C., Baird, A. K., Rose, H. J., Jr., Toulmin, P., III, Keil, K., Castro, A. J., et al. (1976). Inorganic analysis of Martian surface samples at the Viking landing sites. *Science*, *194*(4271), 1283–1288. <https://doi.org/10.1126/science.194.4271.1283>
- Cousin, A., Dehouck, E., Meslin, P.-Y., Forni, O., Williams, A. J., Stein, N., et al. (2017). Geochemistry of the Bagnold dune field as observed by ChemCam and comparison with other aeolian deposits at Gale crater. *Journal of Geophysical Research: Planets*, *122*(10), 2144–2162. <https://doi.org/10.1002/2017JE005261>
- Ehlmann, B. L., Edgett, K. S., Sutter, B., Achilles, C. N., Litvak, M. L., Lapotre, M. G. A., et al. (2017). Chemistry, mineralogy, and grain properties at Namib and high dunes, Bagnold dune field, Gale crater, Mars: A synthesis of Curiosity rover observations. *Journal of Geophysical Research: Planets*, *122*(12), 2510–2543. <https://doi.org/10.1002/2017JE005267>
- Franz, H. B., Mahaffy, P. R., Webster, C. R., Flesch, G. J., Raaen, E., Freissinet, C., et al. (2020). Indigenous and exogenous organics and surface-atmosphere cycling inferred from carbon and oxygen isotopes at Gale crater. *Nature Astronomy*, *4*(5), 526–532. <https://doi.org/10.1038/s41550-019-0990-x>
- Gabriel, T. S. J., Hardgrove, C., Czarniecki, S., Rampe, E. B., Rapin, W., Achilles, C. N., et al. (2018). Water abundance of dunes in Gale crater, Mars from active neutron experiments and implications for amorphous phases. *Geophysical Research Letters*, *45*(23), 12766–12775. <https://doi.org/10.1029/2018GL079045>
- Gainey, S. R., Hausrath, E. M., Adcock, C. T., Tschauner, O., Hurowitz, J. A., Ehlmann, B. L., et al. (2017). Clay mineral formation under oxidized conditions and implications for paleoenvironments and organic preservation on Mars. *Nature Communications*, *8*(1), 1230. <https://doi.org/10.1038/s41467-017-01235-7>
- Hecht, M. H., Kounaves, S. P., Quinn, R. C., West, S. J., Young, S. M. M., Ming, D. W., et al. (2009). Detection of perchlorate and the soluble chemistry of Martian soil at the Phoenix lander site. *Science*, *325*(5936), 64–67. <https://doi.org/10.1126/science.1172466>
- Heirwegh, C. M., Elam, W. T., O'Neil, L. P., Sinclair, K. P., & Das, A. (2022). The focused beam X-ray fluorescence elemental quantification software package PIQUANT. *Spectrochimica Acta Part B: Atomic Spectroscopy*, *196*, 106520. <https://doi.org/10.1016/j.sab.2022.106520>
- Kounaves, S. P., Chaniotakis, N. A., Chevrier, V. F., Carrier, B. L., Folds, K. E., Hansen, V. M., et al. (2014). Identification of the perchlorate parent salts at the Phoenix Mars landing site and possible implications. *Icarus*, *232*, 226–231. <https://doi.org/10.1016/j.icarus.2014.01.016>
- Lapotre, M. G. A., & Rampe, E. B. (2018). Curiosity's investigation of the Bagnold Dunes, Gale crater: Overview of the two-phase scientific campaign and introduction to the special collection. *Geophysical Research Letters*, *45*(19), 10200–10210. <https://doi.org/10.1029/2018GL079032>
- Millan, M., Teinturier, S., Malespin, C. A., Bonnet, J. Y., Buch, A., Dworkin, J. P., et al. (2022). Organic molecules revealed in Mars's Bagnold Dunes by Curiosity's derivatization experiment. *Nature Astronomy*, *6*(1), 129–140. <https://doi.org/10.1038/s41550-021-01507-9>

- Ming, D. W., Gellert, R., Morris, R. V., Arvidson, R. E., Brückner, J., Clark, B. C., et al. (2008). Geochemical properties of rocks and soils in Gusev crater, Mars: Results of the alpha particle X-ray spectrometer from Cumberland ridge to Home plate. *Journal of Geophysical Research*, *113*(E12), E12S39. <https://doi.org/10.1029/2008JE003195>
- Ming, D. W., Morris, R. V., Woida, R., Sutter, B., Lauer, H. V., Shinohara, C., et al. (2008). 2007 Mars Phoenix Scout mission organic free blank: Method to distinguish Mars organics from terrestrial organics. *Journal of Geophysical Research*, *113*(E3), E00A21. <https://doi.org/10.1029/2007JE003061>
- Mitrofanov, I. G., Litvak, M. L., Varenikov, A. B., Barmakov, Y. N., Behar, A., Bobrovitsky, Y. I., et al. (2012). Dynamic Albedo of Neutrons (DAN) experiment onboard NASA's Mars Science Laboratory. *Space Science Reviews*, *170*(1–4), 559–582. <https://doi.org/10.1007/s11214-012-9924-y>
- Moore, H. J., & Jarosky, B. M. (1989). Viking landing sites, remote-sensing observations, and physical properties of Martian surface materials. *Icarus*, *81*(1), 164–184. [https://doi.org/10.1016/0019-1035\(89\)90132-2](https://doi.org/10.1016/0019-1035(89)90132-2)
- O'Connell-Cooper, C. D., Thompson, L. M., Spray, J. G., Berger, J. A., VanBommel, S. J., Gellert, R., et al. (2018). Chemical diversity of sands within the linear and barchan dunes of the Bagnold Dunes, Gale Crater, as revealed by APXS onboard Curiosity. *Geophysical Research Letters*, *45*(18), 9460–9470. <https://doi.org/10.1029/2018GL079026>
- Patterson, C. (1956). Age of meteorites and the Earth. *Geochimica et Cosmochimica Acta*, *10*(4), 230–237. [https://doi.org/10.1016/0016-7037\(56\)90036-9](https://doi.org/10.1016/0016-7037(56)90036-9)
- Putzig, N. E., Mellon, M. T., Arvidson, R. E., & Kretke, K. A. (2005). Global thermal inertia and surface properties of Mars from the MGS mapping mission. *Icarus*, *173*(2), 325–341. <https://doi.org/10.1016/j.icarus.2004.08.017>
- Qin, X., Ren, X., Wang, X., Liu, J. J., Zeng, X., Sun, Y., et al. (2023). Modern water at low latitudes on Mars: Potential evidence from dune surfaces. *Science Advances*, *9*(17), eadd8868. <https://doi.org/10.1126/sciadv.add8868>
- Ralston, S. J., Hausrath, E. M., Tschauner, O., Rampe, E. B., Peretyazhko, T. S., Christoffersen, R., et al. (2021). Dissolution rates of Allophane with variable Fe contents: Implications for aqueous alteration and the preservation of X-ray amorphous materials on Mars. *Clays and Clay Minerals*, *69*(2), 263–288. <https://doi.org/10.1007/s42860-021-00124-x>
- Rampe, E. B., Lapotre, M. G. A., Bristow, T. F., Arvidson, R. E., Morris, R. V., Achilles, C. N., et al. (2018). Sand mineralogy within the Bagnold dunes, Gale Crater, as observed in situ and from orbit. *Journal of Geophysical Research: Planets*, *123*(18), 9488–9497. <https://doi.org/10.1029/2018GL079073>
- Rieder, R., Economou, T., Wänke, H., Turkevich, A., Crisp, J., Brückner, J., et al. (1997). The chemical composition of Martian soil and rocks returned by the mobile alpha proton X-ray spectrometer: Preliminary results from the X-ray mode. *Science*, *278*(5344), 1771–1774. <https://doi.org/10.1126/science.278.5344.1771>
- Tu, V. M., Hausrath, E. M., Tschauner, O., Iota, V., & Egeland, G. W. (2014). Dissolution rates of amorphous Al- and Fe-phosphates and their relevance to phosphate mobility on Mars. *American Mineralogist*, *99*(7), 1206–1215. <https://doi.org/10.2138/am.2014.4613>
- Velbel, M. A., & Losiak, A. I. (2010). Denticles on Chain silicate grain surfaces and their utility as indicators of weathering conditions on Earth and Mars. *Journal of Sedimentary Research*, *80*(9), 771–780. <https://doi.org/10.2110/jsr.2010.074>
- Wiens, R. C., Maurice, S., Barraclough, B., Saccocio, M., Barkley, W. C., Bell, J. F., III, et al. (2012). The ChemCam instrument suite on the Mars Science Laboratory (MSL) rover: Body unit and combined system tests. *Space Science Reviews*, *170*(1–4), 167–227. <https://doi.org/10.1007/s11214-012-9902-4>
- Yin, Q.-Z., Herd, C. D. K., Zhou, Q., Li, X.-H., Wu, F.-Y., Li, Q.-L., et al. (2014). Reply to comment on Geochronology of the Martian meteorite Zagami revealed by U-Pb ion probe dating of accessory minerals. *Earth and Planetary Science Letters*, *385*, 218–220. <https://doi.org/10.1016/j.epsl.2013.09.016>